ALMA MATER STUDIORUM · UNIVERSITÀ DI BOLOGNA

Scuola di Scienze

Corso di Laurea Magistrale in Fisica del Sistema Terra

Simulating the seismicity induced by magmatic dikes with application to the 2000 dike propagation event at the Miyakejima volcano, Japan

Relatrice:
Prof.ssa Eleonora Rivalta

Presentata da:
Luca Soravia

SESSIONE IV

ANNO ACCADEMICO 2022/2023

Contents

Abstract (Eng)

Seismicity induced by fluid-filled intrusions, such as volcanic dikes or hydraulic fractures in industrial settings for the exploitation of georesources, can cause substantial damage to human communities and infrastructure. Thus, studying the spatio-temporal evolution of dikes and associated observables, including deformation and seismicity rates, is important not only for academic purposes but also to improve our ability to evaluate hazards. In this thesis, I develop models for two scenarios of dikes propagating in a brittle-elastic medium and producing deformation, stress and seismicity. For my simulations, I take inspiration from the 2000 dike propagation event at Miyakejima volcano in Japan. In the first scenario I consider a dike propagating at a constant velocity, volume and shape. In the second scenario, the dike still has constant volume, but a decreasing topographic loading at the surface modifies its size and velocity. The seismicity is simulated through Coulomb stress and the rate-state modeling. The dike, which is the source of change of the stress field, is modeled using the boundary elements technique. My simulations replicate some features of the seismicity observed during the Miyakejima dike propagation event, including the migration of an isolated cloud of earthquakes and the lateral thinning of the cloud. I conclude my thesis by suggesting future extensions to the models and tests to carry out with data, to improve the models' potential of forecasting earthquake rates during magma intrusions and hydraulic fracturing operations.

Abstract (Ita)

La sismicità indotta da intrusioni di fluidi, come i dicchi vulcanici o le idrofratture che si creano in contesti industriali di sfruttamento delle georisorse, rappresenta una casusa di potenziale danno per gli insediamenti umani e le infrastrutture. Questo fenomeno rende lo studio dell'evoluzione spaziotemporale dei dicchi e della sismicità ad essi associata, di vitale importanza non solo per uno scopo accademico ma anche per il miglioramento dell'hazard sismico e delle misure di prevenzione dal rischio. In questa tesi realizzo due scenari di sismicità generata da un dicco che propaga in un mezzo roccioso elasto-fragile. Per lo sviluppo delle relative simulazioni mi ispiro all'evento di dicco propagante avvenuto presso il vulcano Miyakejima (in Giappone) nel 2000. Nel primo scenario considero un dicco che propaga a velocità costante mantenendo inalterati forma e volume. Nel secondo scenario introduco l'effetto di una topografia declinante alla superficie, la quale va a influenzare la taglia e la velocità del dicco, ancora considerato con volume costante. Per simulare la sismicità utilizzo il modello rate-state, il quale si basa su variazioni indotte dello sforzo di Coulomb. Il dicco, che rappresenta la sorgente delle variazioni del campo di stress, viene modellato per mezzo di metodi ai boundary elements. Le mie simulazioni replicano alcune caratteristiche della sismicità osservata durante l'evento di propagazione del dicco al Miyakejima, tra cui la migrazione di una nuvola isolata di terremoti e il suo assottigliamento laterale. Nel capitolo finale vengo presentate alcune proposte per un futuro ampliamento dei modelli e un loro test con i dati, per migliorarne il potenziale di forecasting dei tassi di sismicità, durante l'avvenimento di intrusioni magmatiche e operazioni di idrofratturazione.

Introduction

When fluids are injected at high pressure in the Earth's crust, they form roughly planar, thin fractures that upon further fluid injection extend at their tip line (see fig. 1). Fluid-filled fractures occur both in nature, for example as magma-filled intrusions, and in industrial settings as a result of injection of fluids in boreholes. As both natural and man-made fluid-filled fractures propagate, they deform and stress the surrounding rocks. The rocks composing the Earth's crust are often damaged; if the stresses induced by the propagating cracks overcome the strength of the fractures surrounding the crack, the fractures fail, which results in seismicity.
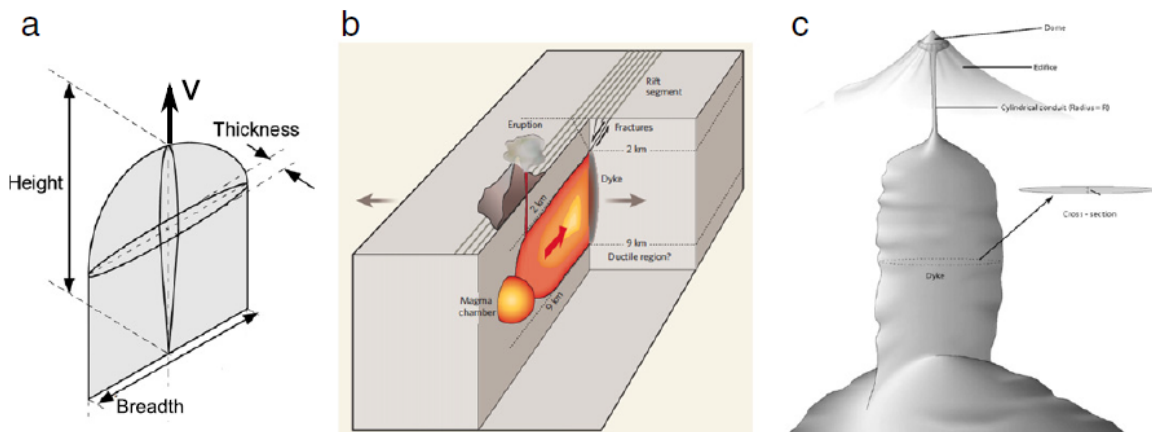
Figure 1: (a) Schematic of a vertically propagating dike. (b) Horizontally propagating dike from a magma chamber. (c) Dike-like root originating from a magma chamber and developing into a cylindrical conduit in the volcanic edifice. Figure 2 from Rivalta et al. (2015), see references therein.

The seismicity induced by propagating fluid-filled cracks is a phenomenon of great interest both in the field of volcanology and in the context of industrial activities. Propagating magmatic dikes transport magma to the Earth's surface to cause eruption, so that a better understanding of the patterns in dike-induced seismicity can help us tracking the magma moving underground and estimating the volume, trajectory and velocity of the dike. As for man-made fluid-filled cracks, controlling the geometry of sub-surface injections is important for a safe

exploitation of geothermal and other forms of energy. Thus, modelling the observables (deformation and seismicity) induced by fluid transport through hydraulic fracturing is one of the best tools for better understanding the mechanisms involved during the fluids' migration and potentially forecasting the earthquakes they induce. It is also of crucial interest in many other societal contexts because of the potential damaging consequences of events of this kind: induced seismicity has caused in the past billions of damage to properties and is a concern for the communities surrounding gas fields (for instance are the Groningen gas field in The Netherlands (Dahm and Hainzl (2022))), waste fluids re-injection sites and locations of interest for new geothermal power plants (for example the enhanced geothermal system below Basel in Switzerland (Deichmann and Giardini (2009))). Developing increasingly reliable forecasting models allows us to reduce uncertainties on seismic hazard and, thus, to better plan risk reduction measures to protect human life and infrastructures.

Earthquakes can be described as events of abrupt energy release in form of elastic seismic waves due to the sudden slip on a newly formed or pre-existing fracture. They occur as a result of elastic deformation and stress accumulating on faults that are located in the brittle elastic lithosphere and are locked by friction. The sources of stress and deformation that lead to critical accumulation can be various: most commonly it is the relative motions of tectonic plates, for example at their boundaries. In general, stresses loading a fault may originate from nearby earthquakes, postseismic relaxation following large mainshocks, slow slip events, gravitational loading at the Earth's surface (such as the filling of a dam lake), thermal effects and also fluid-filled intrusions. In this thesis I will focus on the stresses induced by propagating fluid-filled cracks, specifically the intrusion of sheet-like magma bodies called dikes.

Dikes are formed when magma intrudes brittle elastic rocks. Dikes propagate according to a mechanism called hydraulic fracturing, which, as briefly mentioned above, is a more general process relevant in many different contexts, including industrial activities such as gas extraction/production, oil reservoir formation and geothermal energy generation. All these activities require pumping liquids at high pressure into deep wells in the Earth's crust. The fluids fracture the rock and propagate by moving into the newly formed fracture until pressure is sustained at the inlet. Alternatively, injection may form a fluid pocket achieving self-sustained propagation, as better explained later in this thesis.

In the context of volcanism and eruptions, dikes are the main form of magma transport to the Earth's surface and, simultaneously, dynamic sources of stress changes. Studying their effects on the surroundings in space and time, provide information that can be used to infer from observations their characteristics and behaviour. For instance, from the inversion of deformation and strain rate data at the surface, we can determine the size, location and opening history of the dike. Thus from well-constrained models of the state of the dike it may be possible to forecast their evolution and their effects, such as induced seismicity.

Physics-based seismicity rate models link the stress changes produced by a source of deformation on the potential faults to expected seismicity rates on those faults. Stresses are

especially intense in the proximity of the source, so that elevated seismicity rates are expected there. Thus, by coupling seismicity rate models with calculations of the stress changes generated by a propagating dike it is possible to calculate the expected seismicity rates and how they evolve in space and time. A well-known model for seismicity, that I will use in this thesis, is the rate-state model theorized by J. Dieterich (1994). The rate-state seismicity model converts the Coulomb stress changes (the sum of tangential forces, or shear stresses, and normal stresses times the friction, calculated for an assumed set of receiver faults) generated by a source of stress into expected seismicity rates.

In this thesis I seek to produce simulations of seismic rates for simplified scenarios of dike propagation. I will test the ability of this model to reproduce the main features of the observed spatio-temporal evolution of seismicity near a propagating dike. In particular I will relate the simulations to the 2000 dike propagation event at Miyakejima volcano in Japan. This diking episode generated the most energetic seismic swarm (five M$>$ 6 earthquakes and thousands of M$>$ 3 events) since modern monitoring is in place.

In CHAPTER 1 I present some examples of observations collected during events of dike propagation. In particular I describe patterns of seismicity and deformation, induced by static and propagating dikes. Then I outline the 2000 dike propagation event at the Miyakejima volcano, which is the event of reference for the simulations I have developed in this thesis. After presenting the main observations and results of other studies about the episode, I identify some open questions that this thesis and future works will seek to answer.

In CHAPTER 2, I present diking as the main mechanism of transport of magma through the Earth's crust. Then I describe the theory on which the modelling is grounded. Firstly, I present the model I use to calculate the elastic stresses generated by the dike, consisting of multiple rectangular tensile dislocations combined in a boundary element model. Secondly, I introduce the concepts of Coulomb stress changes and of receiver faults, on which Coulomb stresses are calculated. I explain how positive and negative Coulomb stresses are found to be correlated with increased and decreased seismicity rates, respectively. Lastly, I outline the rate-state model, which belongs to the class of Coulomb stress change seismicity models, and which I will use in the next chapter for the simulations.

In CHAPTER 3, firstly I present simple applications of Coulomb stress change to elementary rectangular dislocations. Then I develop a three-dimensional model of a static dike by using the technique of the boundary elements. Next, I develop two models for two different scenarios of propagation, with some characteristics taken from the 2000 Miyakejima event, and carry out a series of calculations to simulate the spatio-temporal pattern of the expected seismic rates.

In CHAPTER 4 I discuss the results of previous chapters and highlight the potential and limitations of my models, suggesting possible routes for further improvement.

Chapter 1

Observable effects produced by dikes

Magma intrusions produce observable effects including surface displacements and induced earthquakes, as shown in fig. 1.1. These types of data can help constraining models of static or propagating dikes. In the following paragraphs I will present some examples of observations collected during a dike event.

1.1 Deformation induced by a dike

Usually, surface deformation is measured by satellite techniques such as GPS and InSAR, which is based on interferometry. GPS stations' records provide point-wise deformation time series, so that this technique has high temporal resolution but scarce spatial resolution. In contrast, InSAR supplies differential displacement data on extended areas relative to two different times typically separated by a week or more, so that it has high spatial resolution and low temporal resolution. Dike emplacement typically occur on a time scale of hours to a few days, which is shorter than that of InSAR data acquisition. Therefore the latter generally provides information on the cumulative ground deformation of the entire dike event rather than on its detailed dynamics.

As shown in figure 1.1, the 2014 dike at Bardarbunga volcano in Iceland propagated for around two weeks in the NE direction producing, among other effects, a moving cloud of seismicity and evolving deformation. The latter is represented by red and blue vectors of displacement recorded by GPS stations, continuous and campaign, respectively. The displacement field shows the typical features of a tensile dislocation. This dike propagation happened in a segmented way, starting from a first radial segment away from the Bardarbunga caldera and followed by more segments, gradually more sub-perpendicular to the minimum compressive regional stress in the area. Past fissure swarms are indicated in yellow shadows in figure 1.1.
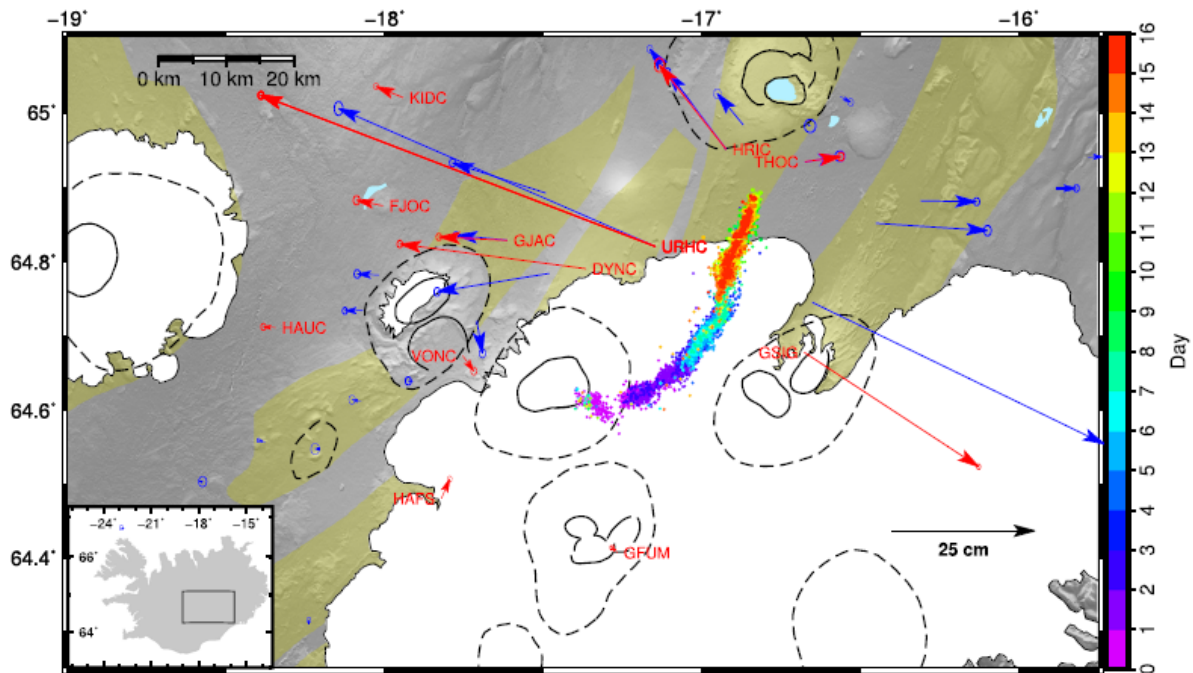
Figure 1.1: Surface cumulative GPS displacements and seismicity induced by the 2014 diking event at the Bardarbunga volcano in Iceland, in the period between the 16th and the 29th of August. Red arrows are continuous GPS stations and blue ones are campaign GPS stations. In color-code is represented the spatio-temporal pattern of induced seismicity (from Ágústsdóttir et al. (2019)). Figure modified from Elıas R Heimisson and Segall (2020).

The opening of the dike and the induced seismicity were more intense in the last segments (corresponding to the green, yellow and red clouds of earthquakes in fig. 1.1). The displacement vectors point outward with respect to the dike, with intensity decreasing moving away from it. Displacements near the central zone of the dike at the end of its propagation are sub-perpendicular to the dike and reach intensity around 1 m. In contrast, near the tips displacement vectors are oblique to the dike and range between some centimeters to some tens of centimeters. This pattern mirrors the expansion of the dike and the compressive and shear strain induced on the surrounding. The few displacement measurements available near the dike tips point towards the dike, mirroring the along-dike shortening induced by the dike dilation.

Another example of deformation induced by a dike intrusion is that of the 2000 Miyakejima volcano event in Japan. The event took place in the Izu archipelago from the end of June to the end of September of 2000. In figure 1.2 (from Cattania et al. (2017)) I show the displacement field generated by the Miyakejima dike as recorded by GPS stations on Kozushima, Shikinejima and Niijima islands, some kilometers far from the intrusion. The data reported in the figure are relative to 1 day of recording within the period of inflation of the dike after its arrest. The observed displacements, indicated as red arrows, show a divergent and perpendicu-
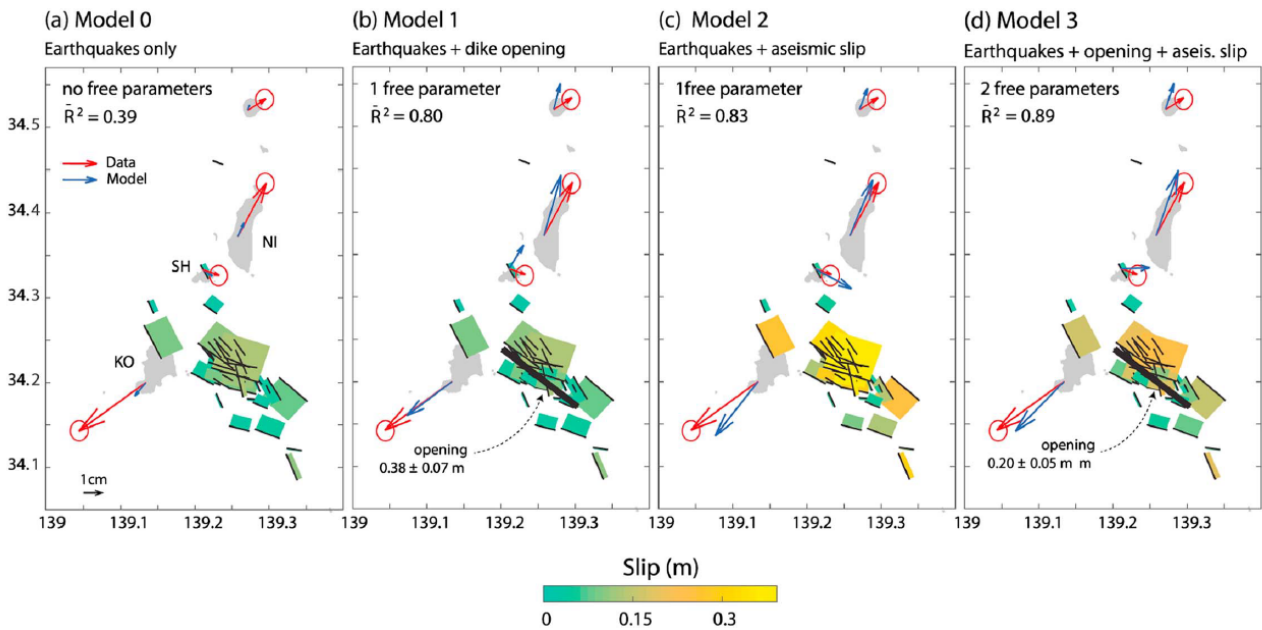
Figure 1.2: Example of various types of modeling of surface deformation (GPS) of the 2000 diking event at the Miyakejima volcano. In red are reported the observe displacements and in blue the modeled ones for different combinations of seismic slip, opening and aseismic slip. The thick solid black line represent the dike. Figure modified from Cattania et al. (2017).

lar movement of a few centimeters, with respect to the opening dike, which is represented as a thick solid segment in black. The displacements are coherent with the pattern of deformation that a tensile dislocation induces in its surrounding. As from the analysis by Cattania et al. (2017), the agreement between observed (red arrows) and modeled (blue arrows) displacements improve if the deformation model includes, beside the dike, seismic and aseismic slips on faults (see figure 1.2, (d)).

The observed crustal deformation relative to the GPS stations of the two major islands (Kozushima and Niijima), for the entire dike event is reported in figure 1.3. This shows how the distance between the islands increased during the progressive propagation and inflation of the dike. The propagation phase lasted 5 days, in which the change in distance is small, of the order of 5 cm. The dike became arrested and an inflation phase started. During this phase, the displacements grew a lot more with a quasi-constant velocity. Simultaneously, abundant induced earthquakes occurred around the dike, generating intense bursts of seismicity, indicated in figure 1.3 by vertical lines. The cumulative distance between the Niijima and Kozushima islands changed during the event reaching in the horizontal and vertical directions respectively around 80 cm and -20 cm. These observations suggest a considerable thickening of the dike during its inflation phase.
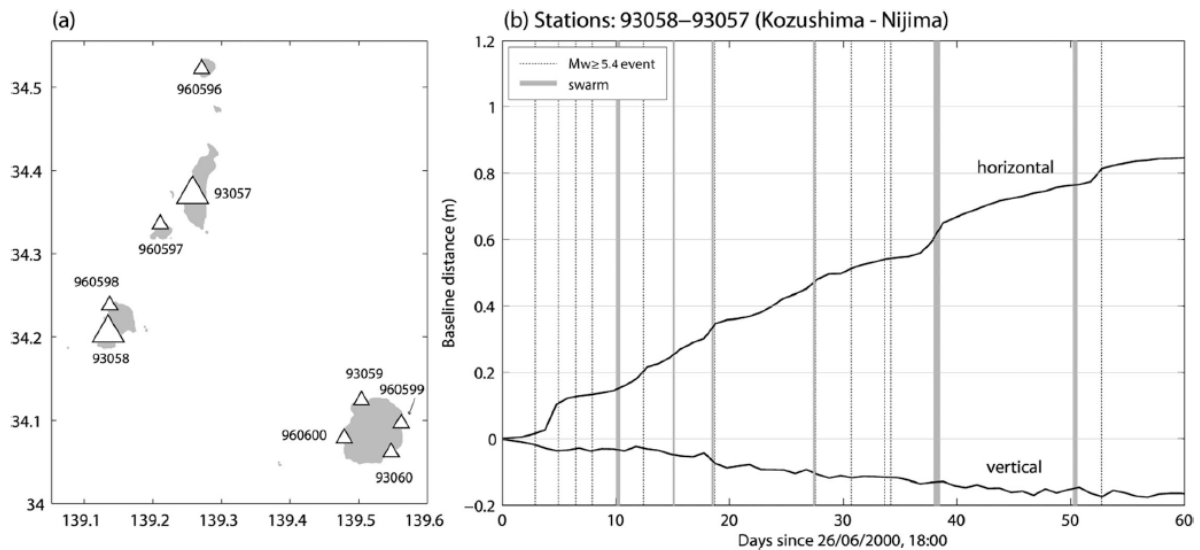
Figure 1.3: (a) Map of the GEONET stations in the northern islands of the Izu archipelago. (b) Baseline distance between the stations (two larger triangles) on the major islands, measured everyday for the first 60 days of the event. Figure modified from Cattania et al. (2017).

Inversions of deformation data

Inversions of ground deformation data can help estimating the shape and volume of magma-filled dikes and the volume change of magma chambers that fed them (Rivalta et al. (2015)). GPS time series potentially allow to constrain the dynamic evolution of the shape of magma-filled dikes but time-dependent inversions have rarely been performed (some examples are Aloisi, Bonaccorso, and Gambino (2006), Montgomery-Brown et al. (2011) and Sigmundsson, Hooper, et al. (2015)). The spatial resolution of GPS data is generally too low to allow determining the fine-scale details of a dike shape, so that in some inversions InSAR and GPS data are jointly inverted.

In general, when inverting surface displacement data, the dike is modeled as one, or a mosaic of, rectangular tensile dislocations (Okada (1985), Okada (1992)). A mosaic of dislocations can represent in a more detailed way the opening distribution on the dike (Sigmundsson, Hooper, et al. (2015)). Further sources of surface deformation are sometimes considered at the same time, to improve the agreement of modeled data with observations or to incorporate some physical constraints: a inflated/deflated magma chamber and graben faults, especially if large earthquakes had accompanied the intrusions (Nobile et al. (2012), Cattania et al. (2017)) (see as reference fig. 1.2).

In order to obtain realistic solutions (although subjectively), regularization/smoothing (Nobile et al. (2012)) or physical constraints (Sigmundsson, Hreinsdóttir, et al. (2010)) are applied on the solutions. Physical constraints can also be applied, such as a constant pressure drop or

a linear pressure gradient on the plane of the dike.This reduces the number of model parameters and produces smoothly varying dike opening with more realistic stress and strain fields in their surrounding (Elıas R Heimisson and Segall (2020)). Moreover, since dikes are filled with fluid material, it makes physical sense to impose conditions of uniform pressure in the horizontal direction or of linearly varying pressure in the vertical direction, on their plane, as I will explain in detail later. In this thesis I assume a linear pressure gradient on the dike plane to constrain my physical models.

1.2   Seismicity induced by a propagating dike

Beside ground deformation, dikes generally induce abundant seismicity. Evidence exists that the swarm seismicity marks the propagating edge of a moving dike. In particular, for laterally propagating dikes an advancing front of earthquake epicenters is often recorded. A typical pattern shows a convex-upward trend, followed by a retreating front (Rivalta et al. (2015)). Between these two limits lies the seismically active area in a spatio-temporal plot of the epicenters, as shown in figure 1.5, where the trends of the fronts are respectively indicated by a blue and a green lines.

This pattern can be well recognised in the epicentral plots of the seismicity induced by the October 2008 dike propagation during the 2005-2010 rifting episode at the Manda-Harraro rift segment in Afar (Ethiopia) (see figures 1.4 and 1.5). As shown in those figures, the migrating seismicity involves a migrating cloud of earthquakes of magnitudes between 2 and 4. With some delay, larger earthquakes appear, with a maximum magnitude of 4.6, on the back of the dike. In the initial propagation phase the dike starts with a velocity of 0.65 ms^{-1} for the first 6 km and then decelerates until it stops after another 7 km. This phase is highlighted by the blue line in fig. 1.5 and has a duration of about 8 hours. As the dike stops, seismicity diminishes its rates and starts to spread backwards with respect to the direction of propagation of the dike. An intense seismic activity continues for more than four days after the intrusion ceases to advance. The number of earthquakes recorded is about 600, of which 100 are of magnitude M$\geqslant$ 3 (Belachew et al. (2011)).
The seismicity after the dike event may be linked to a delay in the seismic response of some of the partially pre-loaded faults to the change in stress induced by the dike or to the interaction of the potential faults with previous induced earthquakes.

A second example of seismicity generated by a propagating dike is that of the 2014 rifting event at Bardarbunga volcano in Iceland. In figure 1.7 (a) I show the evolution of the dike and its induced seismicity, divided into five segments with different orientations, as mentioned above. Those segments formed as discrete trajectory offsets during propagation. The seismicity marks the advancing of the dike, with the hypocenters concentrated near the lower edge of the dike and in particular in segments 3 and 5. Indeed, as shown in figure 1.6 the largest openings of the dike happened in the distal part of these segments. Spaans and Hooper (2018)
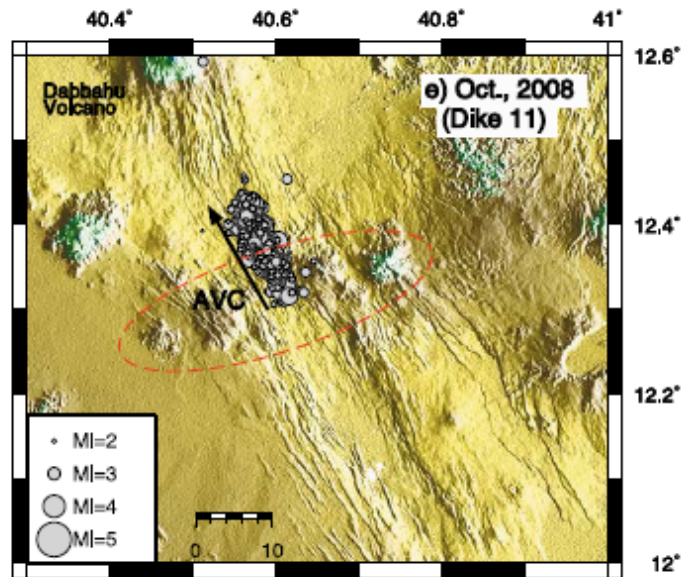
Figure 1.4: Map view of the distribution of the epicenters of the earthquakes induced by the October 2008 propagating dike N. 11 of the 2005–2010 rifting episode at the Manda-Harraro rift segment in Afar, Ethiopia. The black arrow indicates the direction of propagation of seismicity and of the magma intrusion. Earthquakes are scale by magnitude. Figure modified from fig. 3 of Belachew et al. (2011).
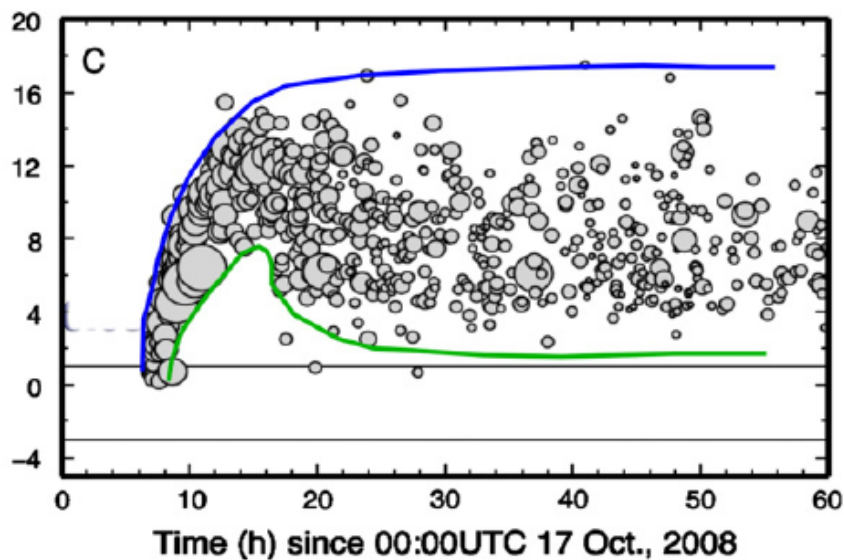
Figure 1.5: Spatio-temporal distribution of the earthquake epicenters, scaled by magnitude, induced by the dike N. 11 of the rifting episode of October 2008 at the Manda-Harraro rift segment in Afar, Ethiopia. The distribution of epicenters is projected along the dike axis direction and show a seismic active zone contained between an advancing front (green) and a retreating one (blue). Figure modified from fig.3 of Belachew et al. (2011).
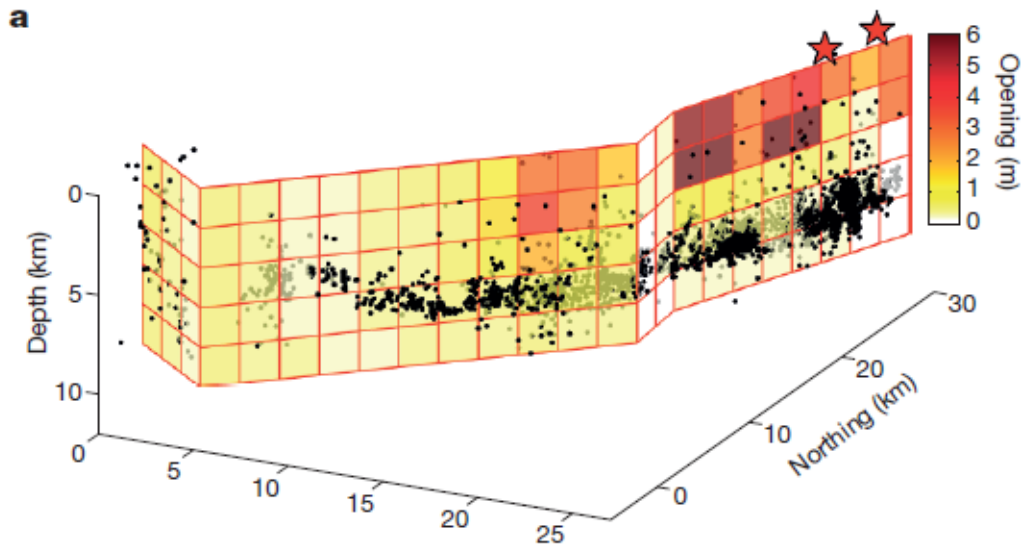
Figure 1.6: Modelled distribution of the cumulative opening of the dike at the end of its propagation, in the rifting episode at the Bardarbunga volcano of 2014. Figure modified from Sigmundsson, Hooper, et al. (2015).

suggested that in the region under the glacier, which intersects segments from 1 to 4 and part of the 5th, earlier intrusions may have accommodated part of the regional extension accumulated over the last 200 years. Differently the region of segment 5 has not experienced recorded rifting episode in the same period: this may explain the larger opening of the dike and clustering of the earthquakes in the last segment. The dike propagation phase lasted 14 days, starting from 16 August 2014, and ended with an eruption at Holuhraun, near the end of segment 5. Moreover, seismic and eruptive activities continued for six months after, with some seismic activity also linked to caldera collapse under the Bardarbunga volcano.

The seismicity, which comprises around $33,000$ events, is concentrated at depths between 5 and 8 km, although the dike expanded also to shallower depths, as demonstrated by small fissure eruptions below the ice sheet and at the main eruption site. The dike must have, thus,largely widened aseismically. Accordingly to Woods et al. (2019), this probably happened because the combined stresses from the dike opening and the ambient regional extension have to be sufficiently large to trigger failure on pre-existing faults. Near the brittle-ductile boundary, which is at those depths, the differential stresses for plate spreading are larger than at shallower locations; moreover near the surface the rock is probably more weak and fracture allowing a largely aseismic opening of the dike. The focal mechanisms of the earthquakes are exclusively strike-slip, aligned with the rift fabric. The main verse of slip changed abruptly from right-lateral to left-lateral in the passage from segment 3 and segment 4 because of the change of the relative orientation of the dike with respect to the rift fabric, as it can be seen in fig. 1.7 (Ágústsdóttir et al. (2019)).
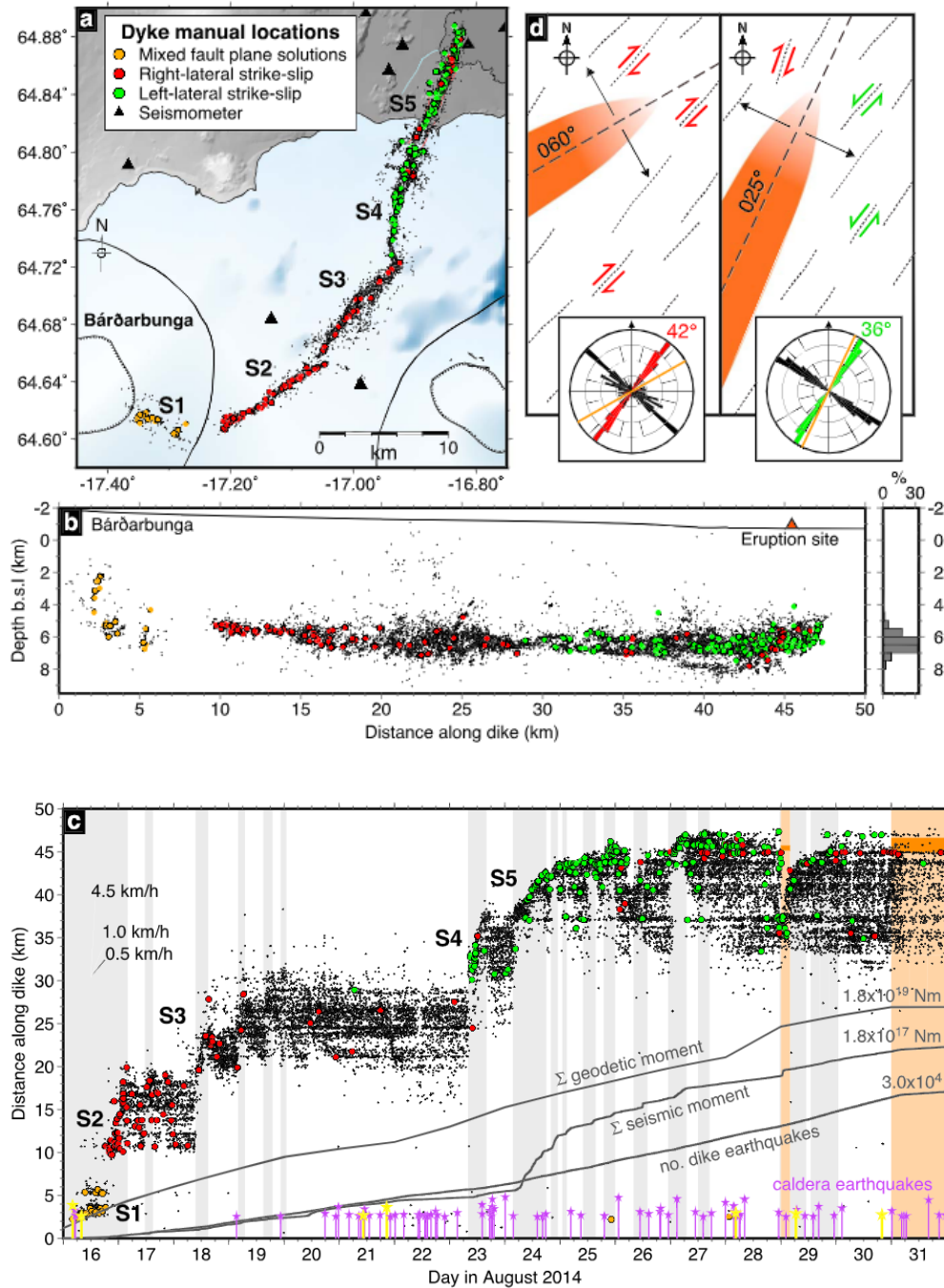
Figure 1.7: Distribution of dike earthquakes locations in map view (a) and lateral section view (b), for the propagation phase of the dike in the rifting episode at the Bardarbunga volcano (Iceland) of August 2014. (c) Spatio-temporal distribution of the dike induced earthquakes during the dike propagation phase. The epicenters of the earthquakes are projected along the dike. In the figure are indicated the various segments into which the dike is divided. In panel (d) are represented in color-code the main mechanisms of the induced earthquakes recorded. The color-coded earthquakes, scaled by magnitude, are those manually analysed by Ágústsdóttir et al. (2019). Figure modified from Ágústsdóttir et al. (2019).

Figure 1.7 (c) shows the distribution, along the dike, of the epicenters of the induced earth-quakes, versus time, for the 14-15 days of propagation of the intrusion of magma. The distribution of earthquakes has a step-wise trend: the seismic activity of a large dike segment drops before the dike proceeds with the successive segment of the intrusion. For each segment the trend of the seismicity is similar to that of others dikes, including the 2008 dike event in Afar (fig. 1.5). The formation of a new segment follows a period of build-up of pressure in the dike, until the dike segment is large enough to fracture the rock at its tip. As propagation resumes, the front of the dike migrates with decreasing velocity, until a new stop occurs after some kilometers. As the dike advances, a compact cloud of epicenters moves forward with it. After the dike stops, the seismic activity spreads all over the newly form segment of the dike. Within each large segment it is possible to recognise smaller segments with similar trends, and other phenomena such as patterns similar to the Miyakejima dike (as shown above and later below) which were identified as slow slip events. These patterns are limited to the region of the current dike segment, so that when a new segment is formed, they disappear.

## 1.3   The 2000 dike event at Miyakejima: an overview

The 2000 dike propagation event at Miyakejima is the natural event from which I take inspiration for my simulations (chapter 3). For this reason, in this section I describe in more detail the event and some of the results of previous studies regarding the induced seismicity observed.

Dike evolution

The 2000 dike propagation event that originated from beneath Miyakejima volcano occurred in the tectonic setting of the Izu archipelago in Japan. The islands are located in the northern part of the Philippine Sea plate (PS plate) where the crust is subjected to northeast-southwest extension and northwest-southeast compression. This is the result of the collision of the PS plate towards the Honshu mainland, to the north, and the subduction of the plate from the Suruga and Sagami troughs. Moreover The Pacific plate subducts under the PS plate (see fig. 1.8 as reference).

Miyakejima is a ten-thousand year old stratovolcano, with a basal diameter of about 25 km and a height of 1200 m above the sea floor, of which 800 m above the sea surface. During the last 5 centuries it has experienced 14 fissure eruptions on its flanks due to basaltic dike formations and their propagation (Maccaferri, Eleonora Rivalta, Passarelli, and Aoki (2016)).

The 2000 magma intrusion started on 26 June 2000 at 6:30 pm of the Japan Standard Time, below the western coast of the volcano, causing thousands of earthquakes of low magnitudes. The first 12 hours were characterize by a complex propagation but after that the propagation regularized changing the direction from EW to SE-NW (towards Kozushima island). This second phase was accompanied by a seismic cloud migrating at a nearly constant velocity of
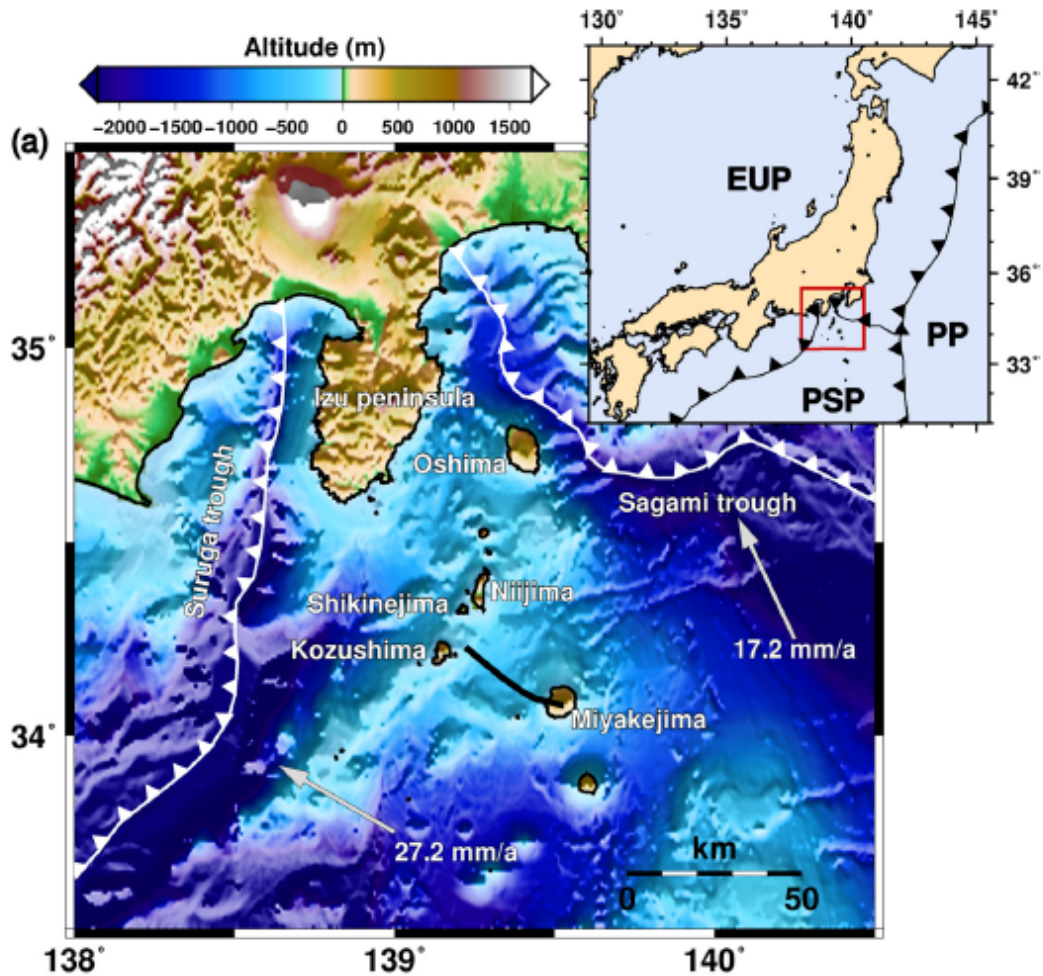
Figure 1.8: (a) Map of the islands of the Izu archipelago in Japan and of the tectonic setting of the region. The topography is color-coded and from ETOPO1 by Amante and Eakins (2009) and the solid blak line represents the projection of the centroid of the daily cloud of seismicity of the first five days of the dike propagation. Figure modified from Maccaferri, Eleonora Rivalta, Passarelli, and Aoki (2016).

about 0.050 ms^{-1} (Ozawa et al. (2004)) (see fig. 1.8, (a) and (b)). The propagation phase ended suddenly on 1 July, near Kozushima, simultaneous with an earthquake of magnitude $M_l = 6.5$ and a displacement between Kozushima and Niijima of 5 cm, indicating an initially narrow dike (Ozawa et al. (2004), Hughes (2010)). The intense seismic activity lasted another two months after the arrest of the dike. The majority of the hypocenters distributed between 10 km NW of Miyakejima volcano and SE of the Kozushima island, in a subvertical plane (Ozawa et al. (2004), Hughes (2010)). In this period ground deformation continued to increase (fig. 1.3) and four earthquakes of $M_l > 6$ occurred, indicating that the dike continued to inflate. Moreover the seismicity branched off the central zone of the dike intrusion, towards north of Kozushima and south of Miyakejima (see fig. 1.9). Furthermore, modeling of the deformation

data on Miyakejima suggest a deflation of a magma chamber at a 4-6 km of depth (Ueda et al. (2005)), and the formation of a a caldera 450 m deep and about 1.6 km wide (Fujita et al. (2002)) in conjunction with only 0.02 km^3 of erupted basaltic products (Saito et al. (2005)), suggest that most of the magma from the deflated chamber went into the dike intrusion (Maccaferri, Eleonora Rivalta, Passarelli, and Aoki (2016)).
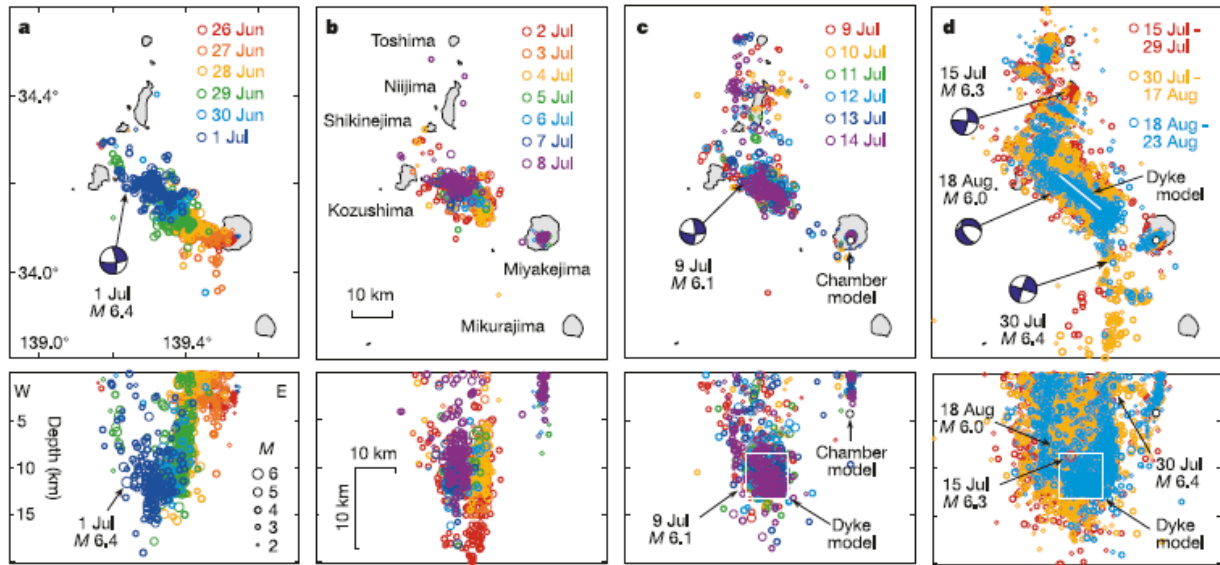

Figure 1.9: Map view (top panels) and cross-section view (bottom panels) of the seismic swarms induce by the dike event of 2000 at the Miyakejima volcano. In figures (a), (b), (c) and (d) are plotted the epicenters and hypocenters, scaled by magnitude, in color-code accordingly to the day/period of occurrence and for different phases of the intrusion event. Figure modified from Toda, Stein, and Sagiya (2002).

Observed pattern of seismicity

As shown in fig. 1.9 (a) and fig. 1.10, the first five days of dike propagation are character-ized by a cloud of seismicity that advances in a compact way at the front of the dike, towards Kozushima island. The focus of the hypocenters increasingly deepens, reaching a depth range between 10 and 15 km beneath the surface. After the propagation phase, the seismicity appears to move backward and forward along the dike length, with progressively decreasing seismic rates (fig. 1.10), as the dike continues to inflate. From figure 1.9 it can be seen that the seis-micity, for the two weeks after the propagation of the dike is concentrated in the front of the dike and to the north of it, with less shallow events and more deep ones. After that, in the fol-lowing five weeks earthquake hypocenters appear to cover a range of depth from the surface to 15 km, and they spread along the whole length of the dike and on branch to the north and to the south of the dike, obliquely to it. As reported on the same figure, five earthquakes of magnitude $M > 6$ occurred between 1 July (end of propagation) 18 August. While three of

them (two strike-slip and one normal faulting earthquakes) happened near the front edge of the propagated dike, the other two strike-slip events occurred on the two oblique branches of the cloud of seismicity, respectively to the north and the south of the dike.
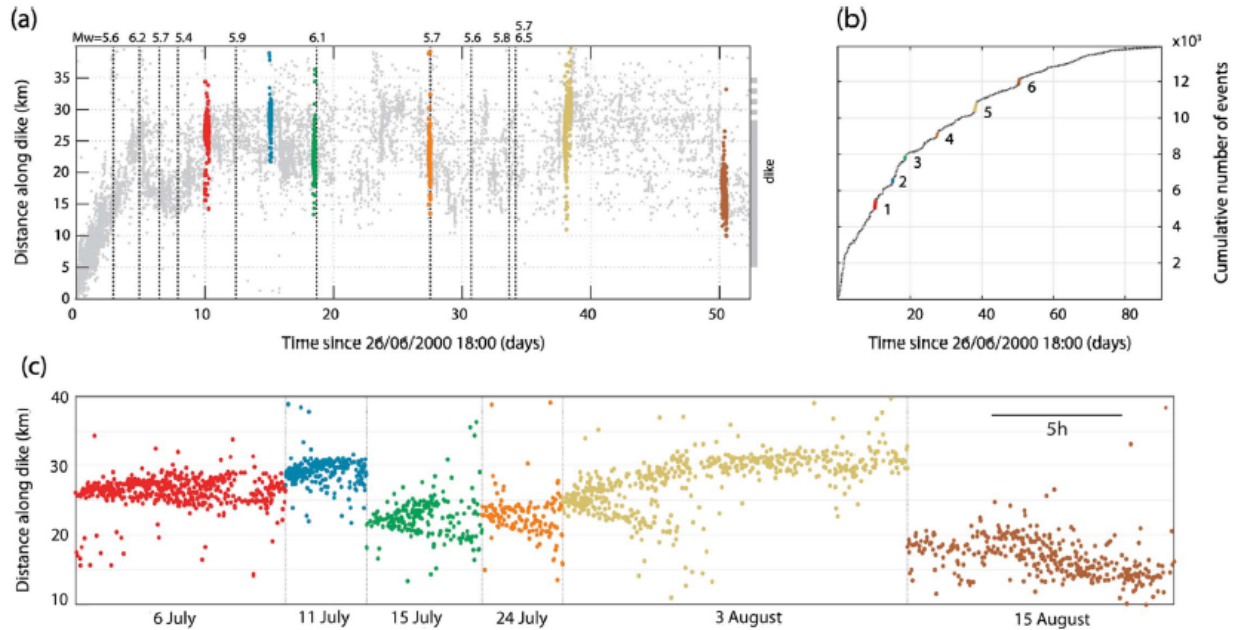
Figure 1.10: (a) Distribution of seismicity along the dike, from the catalog of the Japan Meteorological Agency (JMA). The different bursts (periods of elevated seismicity) are indicated in different colors. (b) Cumulative number of events vs time. (c) Spatial distribution of the various bursts relative to the six slow slip event candidates. Figure modified from Cattania et al. (2017).

Some results of previous studies

A joint analysis of some of the seismicity bursts together with ground deformation data have shown that aseismic slip triggered on faults around the dike have played a big role in the event (fig. 1.2). Cattania et al. (2017) have shown that there are six candidates of slow slip events, characterized by earthquakes bursts lasting few hours and moving at a velocity of about 1 kmh^{-1}. These are represented in different colors in figure 1.10. They have released moments, durations and migration velocities of seismicity consistent with other observed slow slip events and so Cattania et al. (2017) suggest that these seismic bursts are likely driven by slow slips and share properties with tectonic slow slip events. They differ from the latter because earthquakes happened on a set of nonaligned faults, while tectonic slow-slip tends to occur on roughly planar structures. This is consistent with surface layers which are weakly consolidated and with spatially heterogeneous and temporal variable stress field induced by the dike. Moreover, as shown in figure 1.10, the bursts nucleated from the tips of previous ones, suggesting stress interaction (Cattania et al. (2017)).
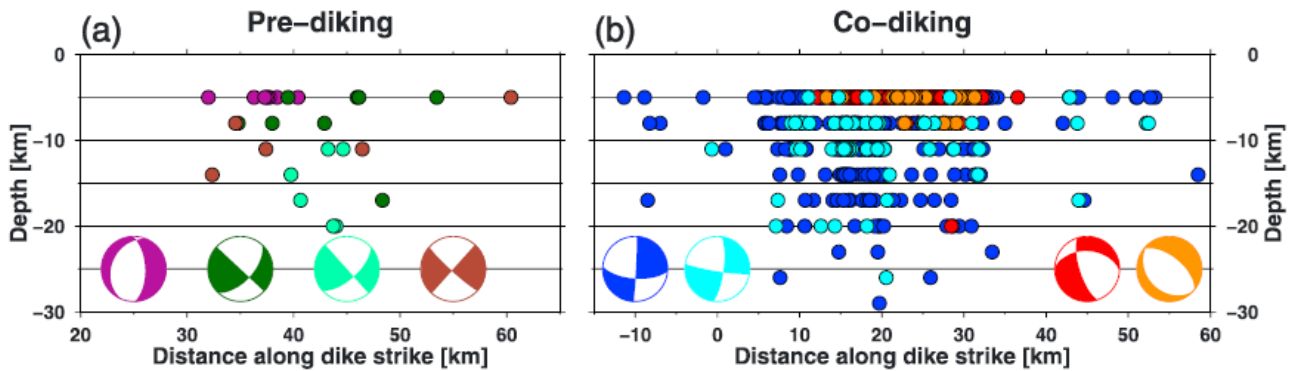
Figure 1.11: Spatial distribution of the hypocenters in cross section, in color code accordingly to the main focal mechanisms resulting from a cluster analysis by Passarelli et al. (2015) on the catalog of JMA, relative to before (a) and during (b) the dike event. Figure modified from Passarelli et al. (2015).
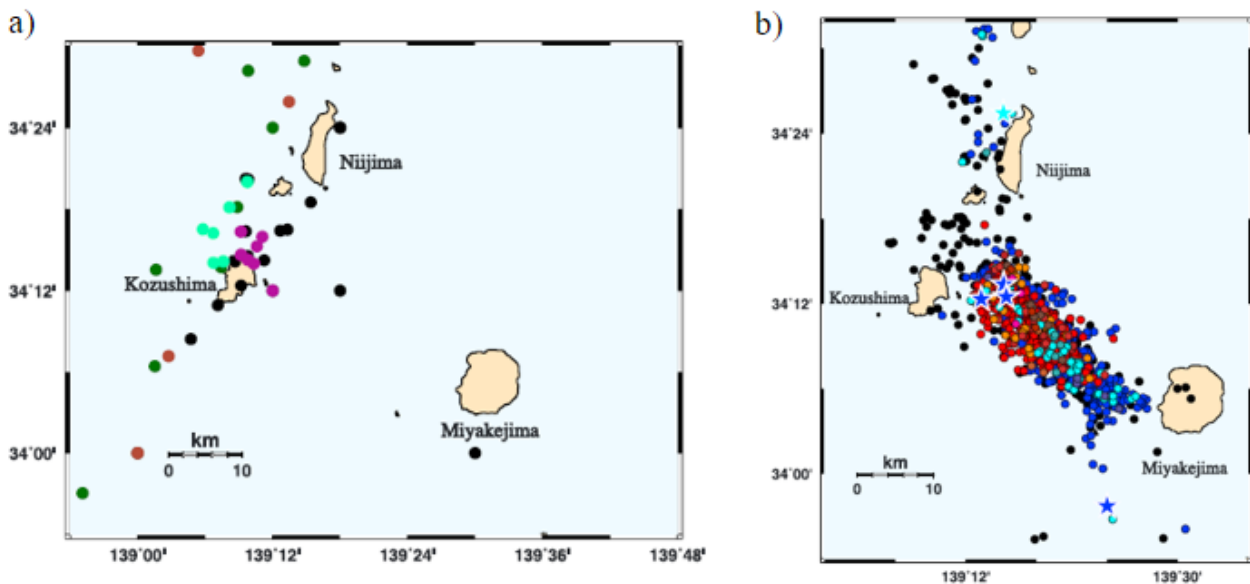
Figure 1.12: Map view of the spatial distribution of the epicenters, in the same color code of fig. 1.11, relative to before (a) and during (b) the dike event. Black dots are relative to earthquakes not classified in the four main clusters of each period. Figure modified from Passarelli et al. (2015).

Another important result on the seismicity at Miyakejima, comes from the cluster analysis of focal mechanisms from the Japan National Research Institute for Earth Science and Disaster Prevention (NIED) catalog, by Passarelli et al. (2015). For the periods before (fig. 1.11 (a)) and during (fig. 1.11 (b)) the dike event the earthquakes can be grouped in four main clusters of similar focal mechanisms, represented through color-coded beach balls. In cross section, the spatial distributions of color-coded hypocenters indicates earthquakes with a prevalent nor-

mal faulting mechanisms are located at shallower depths, while earthquakes with a prevalent strike-slip mechanism cover a depth range from the surface to around 25 km. In map view figure 1.12, the epicenters of predominantly normal faulting earthquakes coincide with the dike location, while the oblique branches are mostly linked to strike-slip mechanisms. The most evident results of the seismicity analysis by Passarelli et al. (2015) are that earthquakes were suppressed west of Kuzushima, and are still suppressed as of today (confer with fig. 1.13 (b)). The second important result is that the least compressive principal stress axis appears to change orientation with the appearance of the dike, from EW to SW-NE. This suggests that the stress field induced by the dike may exceed the regional stress, causing a rotation of the principal axes, at least in the near field (10 km distance) of the dike.
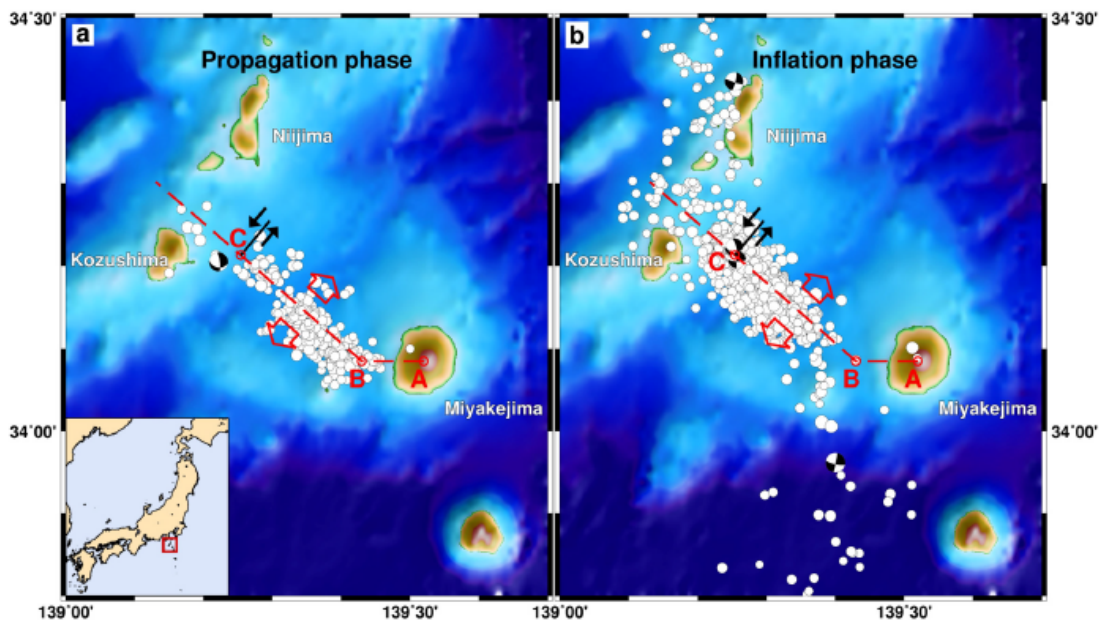
Figure 1.13: Map views of the distribution epicenters during the propagation (a) and inflation (b) phases of the dike event. The red dashed lines indicate the approximate trajectory of the dike. In black is represented the pre-existing strike-slip fault that induced the arrest of the dike. Figure modified from Maccaferri, Eleonora Rivalta, Passarelli, and Aoki (2016).

A last relevant study on the 2000 Miyakejima dike event is byMaccaferri, Eleonora Rivalta, Passarelli, and Aoki (2016). They examined the influence of topographic loading along the dike trajectory and of the stress induced by strike-slip faulting on the N oblique branch on the propagating dike (see fig. 1.13), with the aim of identifying the likely cause of premature dike arrest. They used a boundary element approach and energy release estimations to assess if the dike would have stopped at a certain location. They concluded that topographic loading was the main responsible for the observed shape of the dike, thinner at the back than at its front. Topographic loading also drove the propagation down the flank of Miyakejima and caused a decelerating propagation. In contrast, it was the interplay with the strike-slip fault that caused

the arrest of the dike and forced the dike to successively inflate in the same location. The strike-slip was pre-loaded with shear stresses, as indicated in figure 1.13. Furthermore, the opening of the dike relaxed stresses on the southwestern part of the fault suppressing seismicity in the area while promoting seismicity on the northeastern part.

1.4 Open scientific questions

The two main goals of this thesis are: 1) developing a model for the seismicity induced by a propagating dike and 2) testing the ability of this model to forecast the seismicity induced by dikes in general.

More detailed questions I aim to answer with my thesis work are primarily: what are the predominant physical mechanisms governing dike-induced seismicity? Can a simple model incorporating basic dike physics adequately reproduce the spatio-temporal pattern of earthquakes observed during the 2000 dike event at Miyakejima volcano? What upgrades of the models are needed to improve the agreement between observations and simulations?

Finally, I aim to discuss whether and how these models can be applied to simulate and forecast the distribution of seismicity for dike intrusions. Is it also possible to extend their application to hydrofractures in the context of industrial exploitation of georesources?

Chapter 2

Physical modelling of elastic stresses induced by deformation sources and associated seismicity rates

2.1 Stress accumulation and seismicity: the elastic rebound theory

The principal mediator of the relation between dikes and earthquakes is the stress generated by the dike. The first formulation of the concept of earthquake is the *elastic rebound theory* by Reid (1910). It defines the cause-effect link between earthquakes and the slow accumulation of elastic stress and strain, suddenly released when the stresses reach a threshold of rupture.
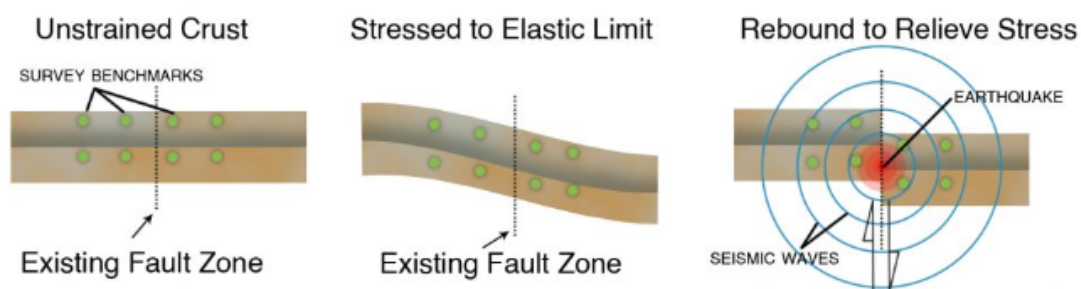
Figure 2.1: Illustration of the elastic rebound theory by Harry F. Reid, for a strike-slip fault in map view. Modified from Yeats (1998).

The theory asserts that the relative movement between two different portions of the Earth's crust can lead to accumulation of elastic strain around an area where two surfaces in contact

are locked together by friction, i.e. the fault zone (fig. 2.1). Here, if the strain overcomes the resistance of the rock to fracturing, it produces a slip, that is a relative movement of the two fault surfaces, with consequent release of strain energy in form of seismic waves.

Beside far-field tectonic forces, strain accumulation in the crust may occur due to local processes. For example, earthquakes both relieve strain accumulation on their fault plane and cause strain accumulation at their tiplines. Other strain-generating processes relevant for volcanic areas include gravitational loading due to the growth of volcanic edifices, pore pressure changes, dike intrusions.

Events like earthquakes and magma intrusions deform the host rock contributing to the loading of faults and fractures distributed in the medium. Crustal rocks are punctuated by plenty of fractures. The distribution of the size of these fractures depends on the history of stressing of a given area but tends to follows a power law type trend. The size of a fracture is proportional to the seismic moment $M_0 = \mu A s$ (where A is the area, μ the rigidity of the medium and s the slip on the fault), whose logarithm is its turn proportional to the magnitude M_w of the earthquake generated. This yields $log(A) \propto M_w$. The frequency-magnitude distribution of earthquakes generally follows the Gutenberg-Richter law (Gutenberg and Richter (1950)), which is a power law and will be presented and discussed in chapter 3. Thus the logarithm of the size follows a power law too. The earthquakes nucleate in small volumes where the stresses overcome the fracture threshold. If in that volume many small fractures slip, they can significantly contribute to shear stress release (see fig. 2.2).
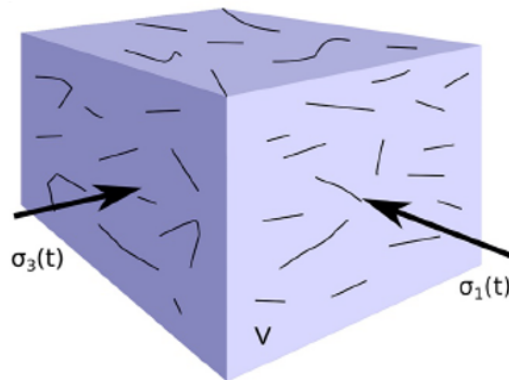
Figure 2.2: Example of a volume containing plenty of small potential fractures that if grouped together can form large sources of shear stress release, which means earthquakes. σ_1 and σ_3 are respectively the most and the least compressive principal stresses. Modified from Dahm and Hainzl (2022).

2.2   Diking: a mechanism of magma transport

The propagation of magma bodies through diking is recognized as the predominant mechanism of magma transport through the brittle upper crust. Diking transports magma to feed eruptions and accommodates plate splitting in zones of continental rifting and ocean spreading. Thus, diking is one of many fundamental processes underpinning plate tectonics. A better understanding of the dynamics of dikes is, thus, fundamental to both our comprehension of the mechanisms governing the dynamics of the Earth's lithosphere and for the practical need to protect human lives and assets from the damaging effects of volcanic eruptions.

Diking events cannot be observed directly but are often observed indirectly through the geophysical signals they induce, such as ground deformation and propagating swarms of earthquakes (Elías R Heimisson and Segall (2020)), as explained in chapter 1. Analysing the spatio-temporal pattern of seismicity and of the ground deformation caused by dikes can help us answering open questions about the physical controls of these processes. However, the importance of dike studies and modelling is not limited to better comprehending magma-related phenomena. Indeed, the knowledge gained on their behaviour can also be exploited, with the proper adjustments, to study industrial hydraulic fracturing processes, as these share common physics.
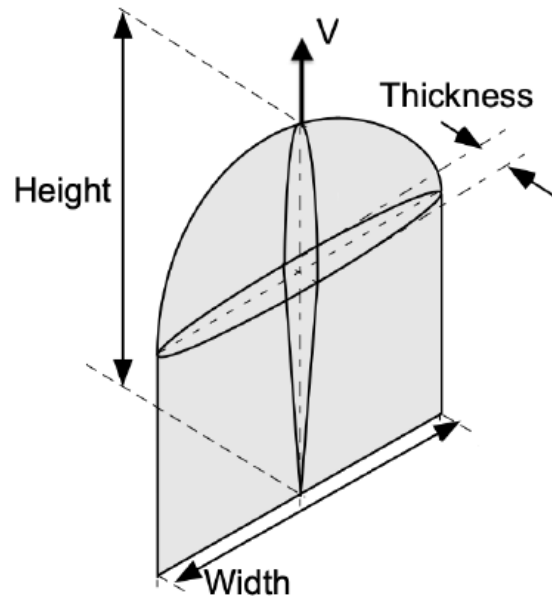

(a) West Spanish Peak in Southeastern Colorado   (b) Mount Etna in Southern Italy

Figure 2.3:   Examples of frozen eroded granitic (a) and basaltic (b) dikes.   References: (a) https://rdougwicker.com/tag/west-spanish-peak/ and (b) "Geomorphological Features" page on Facebook - post of the 28th of March 2022.

Figure 2.4: Simplified representation of a vertically propagating dike. Modified from Watanabe et al. (2002).

2.2.1   Dike geometry, formation and propagation

Dikes generally form and propagate as low-viscosity magmas accumulate above rock volumes of melt production. When a sufficiently large magma pockets accumulate, they force their way into the crust by fracturing the rock. From field observations, the geometry of dikes appears approximately planar with three different characteristic dimensions (for a visual reference see fig. 2.3). Two of them, *length* and *width*, are substantially more extended than the third, the *thickness*. When a dike is propagating vertically, the length is often called the *height* of the dike (fig. 2.4). The length is in general the largest dimension and extends from hundreds of meters to some tens of kilometers (Rivalta et al. (2015)). The width is generally smaller than, but of the same order of magnitude as the length. In contrast, the thickness, which corresponds to the opening of the dike, typically ranges from tens of centimeters to several meters.

Shallow dikes are formed when, upon pressurization, the walls of magma reservoirs rupture so that magma is released and the host rock is fractured. For a fluid-filled intrusion to form, a certain volume of magma is needed. As explained in section 2.3, Griffith (1921) theorized that, for all types of fractures, only if the strain energy release and the mechanical potential energy of the fracture are large enough to match the surface energy needed to create two new increments of crack surfaces, the fracture can elongate. This is equivalent to the existence of a critical volume of buoyant magma that needs to accumulate before the necessary strain energy release can be reached. Once the dike is formed it can continue to grow as magma from a pressurized magma chamber, is supplied through a channel. Otherwise, if the channel closes, the dike can detach and, if its volume is near the critical value, it can propagate fracturing the

surrounding rock.

Fluid intrusions in the form of hydraulic fractures are complex phenomena coupling rock deformation, fracturing, heat exchange, flow of compressible fluids between moving walls, and creation of host rock damage, just to name the most important processes involved. Simplifications are necessary if we want to understand the interactions of these factors. One way of simplifying the behaviour of dikes and the effects of dike propagation on the surrounding media is to use analytical solutions for their shape. In the next paragraphs, I will introduce the approximations I have made for the simulation of a magma-filled intrusion as a deformation source in a portion of the Earth's crust. I will also introduce how such approximations can be used, through a series of steps, to simulate, first, the stress field, and second, the seismicity, induced by the propagation of the dike.

2.3   Basics of Fracture Mechanics and dike propagation

Since dikes are sheet-like intrusions that propagate in the Earth's crust by fracturing the rock, when dealing with moving dikes fracture mechanics plays a primary role.

Griffith (1921) defined a criterion to determine favorable conditions for cracks to grow, based on energy considerations. He suggested, after experimental observations, that during crack propagation the material fails at low macroscopic stresses but locally high ones, as little flaws and cracks concentrate the stress.

The total energy of a cracked body, he considered, ignoring kinetic, thermal and chemical energies, was:

$$U_{tot} = U_0 + U_{strain} - W_L + U_{surf} \tag{2.1}$$

where U_0 is the energy of the uncracked and unstressed body, U_{strain} and W_L are respectively the elastic strain energy and the work done at the boundaries, which constitute the mechanical potential energy, and U_{surf} is the surface energy associated with the crack faces. If a crack is introduced in a medium the net mechanical potential energy decreases and it is exploited to create new crack surface, which means surface energy increases. In particular the mechanical energy decreases quadratically with the crack length (considering a 2D crack of length $2a$), while surface energy increases linearly, as shown in fig. 2.5. This yields to the existence of a critical stress σ_{crit} and crack length a_{crit} (indicated with a star in fig. 2.5) as in eq. 2.2, where γ is the surface free energy and μ and ν are elastic parameters. This condition predicts theoretically an unstable growth in case of values of σ or a greater than the critical ones, and an unstable closing of the fracture if they are not reached. In real cases other factors act to stabilize the propagation or inhibit crack healing. For instance, in the case of shear cracks that correspond to earthquakes, at the end of the slipping they stop for different possible

factors, including the presence of an heterogeneous stressing or friction conditions, such as the adsorption of chemical constituents on the faces of the crack (J. Rice (1978)).

$$\sigma_{crit} = \sqrt{\frac{4\gamma\mu}{\pi(1-\nu)a_{crit}}} \tag{2.2}$$

In the case of dikes, which can be regarded as fluid-filled fractures, the propagation never reaches an unstable condition, rather a characteristic speed, because of the finite fluid availability from a magma chamber, which limits the volume, dimensions and speed of the dike. Indeed magma flow into the new crack elongation takes time depending on fluid viscosity and density, so that catastrophic crack growth is inhibited.

In terms of energy, the fracture grows when the rate of mechanical potential energy decrease overcomes the energy lost in creating new crack surface. The negative of the change of the potential energy for a small elongation dl, $-\partial U_{mech}/\partial l$, which is denoted with G and referred to as *energy release rate* or *crack extension force*, allows to formalize this energy requirement for crack growth in the definition of a critical energy release rate G_{crit} that has to be matched or overcome for propagation to occur.
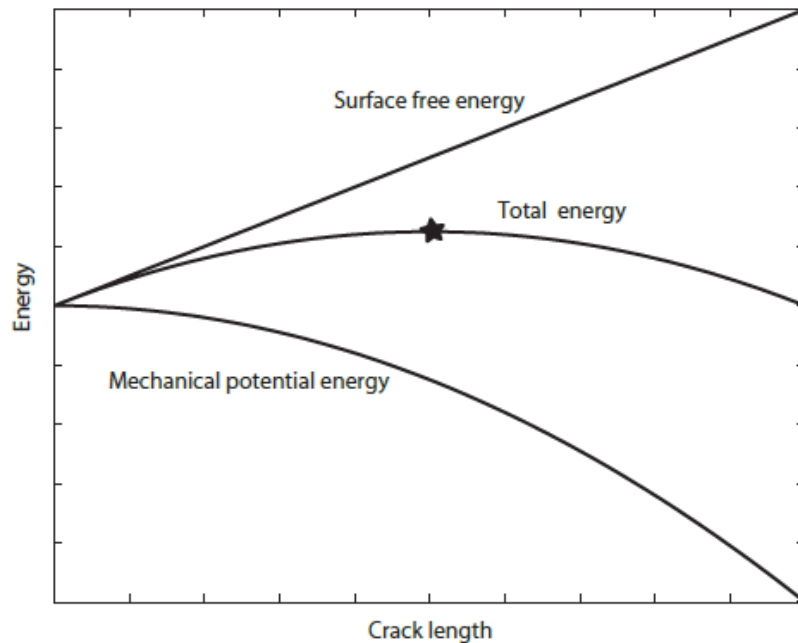
Figure 2.5: Variations of the various energy components and of the total with respect to the crack length a. With a star is indicated the critical crack length (from Segall (2010)).

Analogously, a condition on the stress field for crack growth can be established. Near the tip of a crack, the stress can be described by eq. 2.4, where I am considering a 2D crack for simplicity.

$$\sigma_{ij}(r, \theta) = \frac{K}{\sqrt{2r}} f_{ij}(\theta) + \text{higher order terms} \tag{2.3}$$

In this equation, the polar coordinates are centered at the tip of the crack, with r representing the distance, $f_{ij}(\theta)$ are functions of the angle with respect to the crack plane and are different for the three crack modes (mode I, II and III referring respectively to opening, in-plane shear and anti-plane shear). K is called *stress intensity factor* and characterizes the magnitude of the local stress near the tip, where it may be very large. This way the condition for crack propagation relative to a critical stress can be reformulated in terms of a critical K which is called *fracture toughness* and denoted as K_c. The rock fracture toughness is defined as the resistance of the material when undergoing fracturing (Gonnermann and Taisne (2015)). So when the mode I stress intensity factor, K_I reaches or overcomes the fracture toughness at a tip, it leads to crack growth or propagation. As further proof of the fact that the stress and energy perspectives are consistent with each other, a relation between G and K can be derived (Segall (2010)):

$$G = \frac{\pi(1-\nu)K^2}{2\mu} \tag{2.4}$$

## 2.4   Dike propagation and stress gradient

Dike shapes and trajectories can be very complex depending on the properties of the host rock and of the fluid, on the mass/volume of fluid involved and the external stress field. In general, propagation by hydraulic fracturing is driven by the buoyancy of the fluid/magma, less dense than the surrounding rock, and/or by a gradient in the stress field which can favour the propagation in the direction of decrease of the external normal stress.

An illustrative example of how a stress gradient can affect dike shape and propagation is shown in fig. 2.6 where a horizontal intrusion is supplied with further magma by a pressurized magma chamber which allows the dike to grow in volume and internal pressure. When the stress intensity factor at the tips reaches the critical value K_c, the rock fractures and dike grows or propagates. For what concerns the shape, it is given by the balance between internal pressure (p) and the external normal stress (σ_n, negative in compression), whose difference gives the overpressure $P = p + \sigma_n$. If the overpressure is uniform on the dike walls, the opening crack is elliptical (fig. 2.6 (1)). In contrast, if there is a uniform horizontal external stress gradient of the type of fig. 2.6 (3), the dike takes a tear-drop shape, because of the heterogeneous overpressure distribution. In this configuration, at one tip K_I is larger than in the elliptical case, while at the closing tip $K = 0$. In this configuration, the fracture can achieve self-sustained propagation.

A self-sustaining propagating fracture can form vertically, due to the difference between
the external lithostatic pressure gradient and the smaller internal hydrostatic one(fig. 2.7). This
is representative of a case when the magma is less dense than the host rock, generating a
buoyancy effect which may lead the propagation upward, if the fracture's volume is sufficient
to yield $K_I > K_c$.
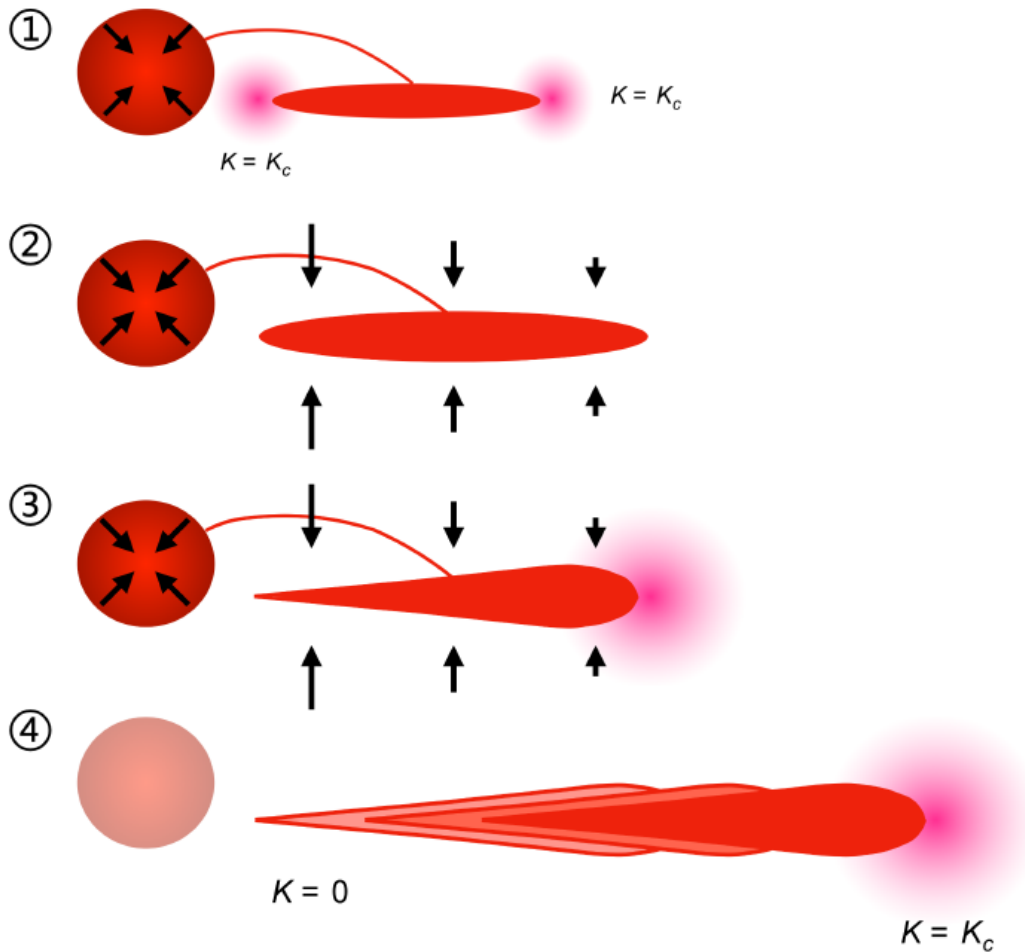
Figure 2.6: Illustration of a magma intrusion in presence of an external horizontal normal stress gradient. (1)
ellipsoidal dike, uniformly pressurized, supplied of magma by a pressurized magma chamber in contraction, and
K_I at crack ends at the critical state for propagation; (2) and (3) effect of an horizontal stress gradient on the shape
of the intrusion; (4) detached dike that starts to propagate without further injection of magma from the chamber
and stress intensity factor equal to K_C at the propagating end and equal to zero in the closing tail. (Modified from
a figure by E. Rivalta)

.
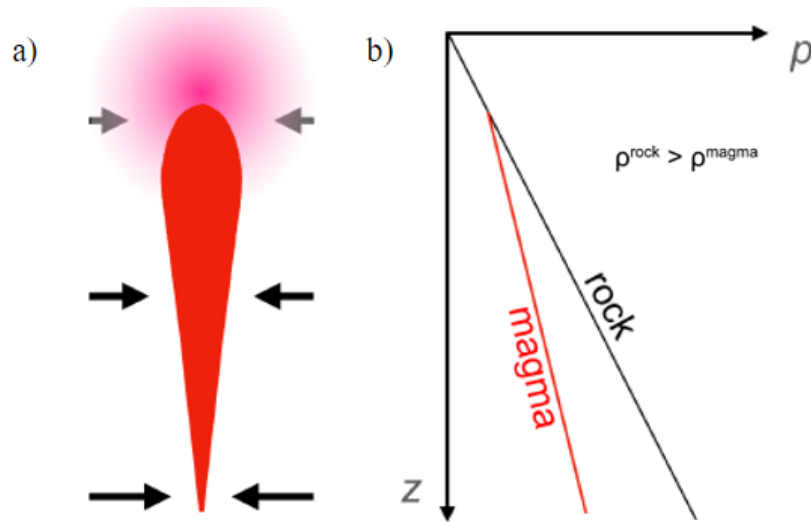
Figure 2.7: a) vertical dike shaped by a vertical gradient of the overpressure. b) diagrams of the pressures as functions of depth (z) inside and outside of the dike, differences caused by the minor density of the magma. (Modified from a figure by E. Rivalta)

.

2.5   Dike emplacement as a source of static stress change

2.5.1   Tensile dislocation in an elastic half-space

The simplest way to model the deformation induced by a static dike in the elastic host rock and displacements on the earth's surface is to use a rectangular tensile dislocation in an elastic half-space. Okada (1985) provided the analytical solutions of the elastostatic problem in an elastic half-space (Cauchy's equations 2.5) for the displacements (u_i) induced on the surface of the half-space, in the presence of a rectangular dislocation source. Successively, Okada (1992) complemented previous solutions with those for the stress, strain and displacement fields in the whole half-space. Recently, Nikkhoo et al. (2016) extended these solutions to rectangular dislocations with full degrees of freedom in terms of spatial orientation (one side of the Okada (1992) dislocations is bound to be parallel to the free surface), and removed artifact singularities affecting the Okada (1992) along the elongations of the dislocation sides (fig. 2.8).

These solutions can be used to calculate the deformations induced by earthquakes or fluid-filled intrusions when the parameters of the source and of the elastic medium are known or set. They can also be applied, conversely, to determine the unknown source parameters, such as the fault/dike size and geometry and the fault/dike slip, by inverting the observed surface deformation.
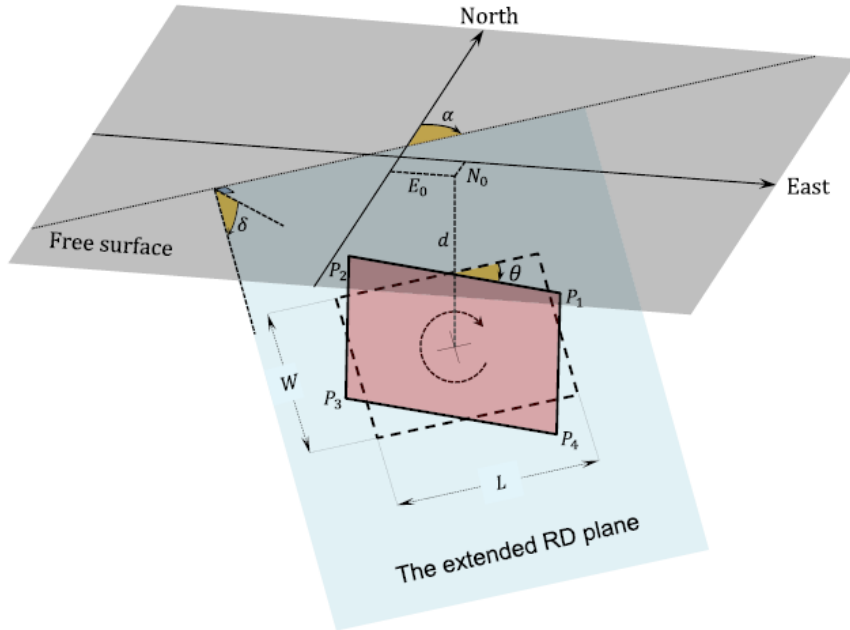
Figure 2.8: Geometries of the Okada (1985) and Okada (1992) solutions (dashed lines) and of the solution by
Nikkhoo et al. (2016) (solid line), for a rectangular dislocation in a half-space. The latter possesses full rotational
degrees of freedom because it has also the plunge angle θ. Figure from Nikkhoo et al. (2016).

A rectangular dislocation (RD) is a rectangular planar surface on which the displacement
field is discontinuous by a uniform quantity, b_i. b_i is a vector in the three dimensional (3D)
space with index i assuming values from 1 to 3. This vector is called the Burgers' vector and
is defined as the difference between the displacements on the two surfaces of the dislocation,
which were in contact before their relative movement $\Delta u_i = b_i$. So $b_i = u_i^+ - u_i^-$, where,
relatively to a normal versor, which defines the positive orientation of the dislocation area, u_i^+
is the displacement on the positive surface and u_i^- that on the negative one.

On the rest of the elastic medium the displacement field is a continuous function of the
position in space. In general b_i can have both shear and normal components with respect to the
discontinuity surface. The shear components are associated to sources called edge or screw
dislocations, for which b_i is parallel to the surface, while the normal component generates a
dislocation known as tensile.

Once the displacements are calculated, the stress and strain fields can be obtained using
equations 2.6 in the assumption of an isotropic homogeneous elastic medium. In equations
2.5 and 2.6 indexes i and j assume values from 1 to 3 and both the Einstein's notation and the
'comma notation' for derivatives are used.

$$\mu u_{i,jj} + (\lambda + \mu)u_{j,ij} + b_i = 0 \tag{2.5}$$

$$\varepsilon_{ij} = \frac{1}{2}(\frac{u_i}{x_j} + \frac{u_j}{x_i})$$
$$\sigma_{ij} = 2\mu\varepsilon_{ij} + \lambda\varepsilon_{kk}\delta_{ij} \tag{2.6}$$

In my case, since a fluid-filled intrusion is primarily a tensile source of deformation, I use a tensile RD in which the b_i vector has only the component normal to the plane of the source. Additional parameters required for the calculations of the displacements and stresses are the Lame's parameters (λ and μ), which characterize the brittle-elastic medium, the geometry (length, L, width, W, and depth, D), orientation in space (δ dip, α strike, θ plunge angles) and opening (b_i) of the dislocation.

2.5.2   Boundary Element Model representation: distributed opening

A single RD of uniform opening is inadequate to model the seismicity induced by a dike. This is because they provide only very rough approximations of the displacements, strains and stresses in the near-field of the source, especially close to its border, which is where seismicity is expected to cluster. Indeed dikes are extended sources which may not have planar shape and have 'tapered' opening at their tip line. The stress field, which is a required input for the seismicity simulations, is sensitive to the geometrical details of the source. Therefore a more complex representation of the dike is needed.

A fundamental requirement for a more realistic dike shape is that the boundaries of the intruded body gradually go to zero approaching the edges. For this purpose a more suitable choice of representing a dike is a numerical model in which the dike is discretized in many small tensile dislocations of appropriate openings. A convenient choice for the discretization is to use a crack model. In this case, differently from a dislocation model, the stress (difference between external stress and fluid pressure) acting on the fault/dike surface is specified as a boundary condition, rather than the displacement discontinuity (see for instance fig. 2.9 and chapter 4 of *Earthquake and Volcano Deformation* by Segall (2010) for more details).

The problem I address here is finding the opening distribution of a mosaic of rectangular dislocations representing a dike. The openings represent the distributed thickness of the dike.

A useful class of methods often used in representing dikes and their propagation is that of boundary element methods (BEMs). These methods are based on the discretization of the sole domain boundaries (as opposed to e.g. Finite Element methods, which discretize the whole volume). In particular the one I employ in this work is called the *displacement discontinuity method* (DDM, *Boundary Element Methods in Solid Mechanics* by Crouch and Starfield (1984)). The DDM exploits the knowledge of the analytical solution for displacement and
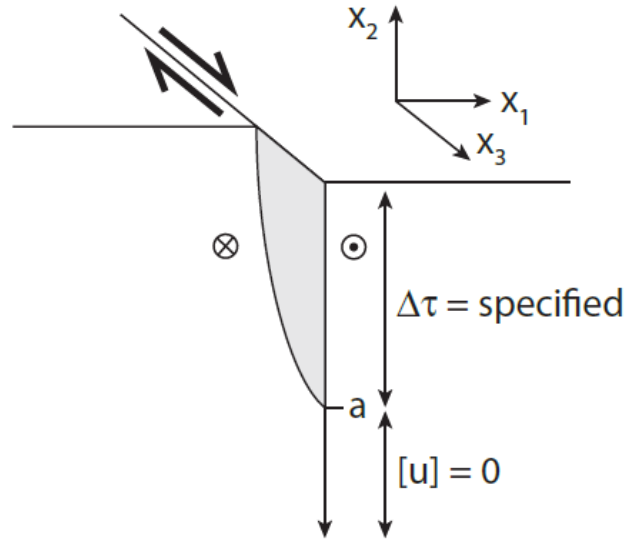
Figure 2.9: Crack model for a strike-slip fault. The stress drop $\Delta\tau$ within the slipping zone is specified while the slip (light gray area) there has to be solved for. Also the slip ([u]) is known outside the slipping zone and equals zero. (figure from Segall (2010)).

stress in an elastic medium due to a single dislocation characterized by a constant displacement discontinuity, to find the solution for a combination of N of them. Being valid the principle of superposition in the elastostatic context, a valid solution is achieved just by summing the effects of all N dislocations. Indeed, since a rectangular dislocation satisfies the elasticity equations and these are linear, also a combination of RDs satisfies them. In this way a crack, whose surfaces have been displaced relative to one another, can be represented through N dislocations with opening appropriately scaled so that the boundary conditions are satisfied on the crack plane.

When the displacement discontinuity distribution on the crack is unknown, it is possible to find it through setting and solving an inverse problem given the stress conditions on the N elements. Indeed by knowing the analytical solution for the stresses caused by all dislocations on the center of every element of the crack boundary it is possible to build a system of algebraic equations (2.7) in which the normal and shear stresses are written as combination of the displacement discontinuity of each element:

$$
\begin{cases}
\sum_{j=1}^{N} [b_j^n N_{ij}^n + b_j^s N_{ij}^s] = -\Delta P_i \\[2mm]
\sum_{j=1}^{N} [b_j^n S_{ij}^n + b_j^s S_{ij}^s] = \tau_i
\end{cases}
\tag{2.7}
$$

where b_j^n and b_j^s represent the normal and shear components of the Burgers' vector of the j-th dislocation; N_{ij}^n and N_{ij}^s are the influence coefficients of the j-th source for the normal stress on the i-th element, while S_{ij}^n and S_{ij}^s are those for the shear one; ΔP_i and τ_i are the overpressure and shear stress at the midpoint of the i-th element. The influence coefficients correspond to the effects on the stresses of the i-th element, of unit values of the Burgers' vectors $b_j^{n,s}$ of the j-th source.

In this manner if the stresses at the boundary are set, the system can be inverted for the displacements of the N sources. The solution to the problem is given by the $b_j^{n,s}$, with j=1, ...,N, that match the boundary conditions ΔP_i and τ_i, with i=1, ...,N. The overpressure $\Delta P_i(x,y,z)$ is the difference between the pressure of the fluid inside the crack and the external pressure of confinement, given by the lithostatic $P_{lit}(z)$ and the normal part $\sigma(x,y,z)$ of other potential source of stress. The shear component τ_i is of topographic or tectonic origin. For a schematic example of application of this method to a two-dimensional propagating dike see fig. 2.10, where instead of rectangular patches the elements of the boundary are segments.

Thus, system of equations 2.7 is simplified, in Einstein's notation, to:

$$b_j^n N_{ij}^n = -\Delta P_i \qquad (2.8)$$

with only the normal component (opening) of the Burgers' vectors of the N sources and the overpressure boundary conditions. Furthermore after the linear system is solved, I apply an additional constraint of non-negative opening, to avoid compenetration of the two opposite surfaces of a RD patch:

$$b_j^n \geq 0 \qquad (2.9)$$

This is made by putting to zero the negative openings on the non positive patches.

2.6   Coulomb stress change: a model for fault failure

2.6.1   Coulomb stress

The Coulomb stress CFS (also known as 'Coulomb failure stress') is a particular combination of shear (τ) and normal (σ_{tot}) stresses, relative to a stress field tensor and an oriented plane in 3D space, that expresses the propensity of a fault to slip. According to the Mohr-Coulomb criterion, failure on a plane is facilitated by a rise in shear stress while it is hampered if the normal stress increases. That is because a higher normal stress enhances the frictional force that opposes the slip. Thus a change in CFS may help predicting how a change in the local stress field can affect seismicity. The relation has the form

$$\Delta CFS = \Delta \tau + \mu_{fr} \Delta \sigma_{tot} \qquad (2.10)$$
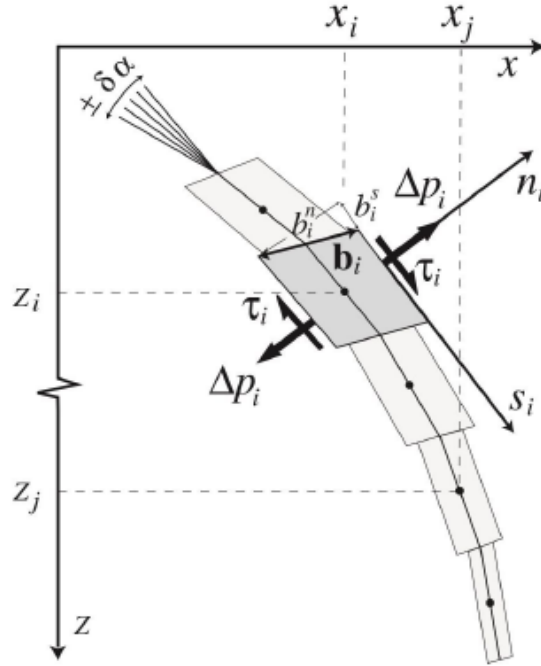
Figure 2.10: Two-dimensional fluid-filled crack modeling by Maccaferri, Bonafede, and Eleonora Rivalta (2011).

where μ_{fr} is the friction coefficient. The total normal stress is given by $\sigma_{tot} = \sigma_n + p$ with σ_n the stress normal to the fault (positive for extension) and p the pore pressure. There are different poroelastic models to describe the relation between a variation in the stress field and the pore pressure change (see Cocco and James R. Rice (2002) and references therein). I use the apparent friction poroelastic model as used in Simpson (1994) and King, Stein, and Lin (1994), which gives $\Delta p = -B\Delta\sigma_n$. This applies in undrained conditions, i.e. when the stress change in the rock is induced more rapidly than fluid pressure can change through flow. B is the Skempton coefficient which assumes values between 0.5 and 1. So substituting the last two expressions in equation 2.10 yields

$$\Delta CFS = \Delta\tau + \mu'_{fr}\Delta\sigma_n \tag{2.11}$$

with an effective coefficient of friction $\mu'_{fr} = \mu_{fr}(1-B)$ which has to be set as input parameter. It generally ranges between 0.0 and 0.75, in many cases the value $\mu'_{fr} = 0.4$ has been used (for example by King, Stein, and Lin (1994)), so this is also chosen here (see chapter 3).

2.6.2   Receiver faults

As illustrated in the previous paragraph, the Coulomb failure stress is a quantitative indicator of the state of stress of a fault and thus of the likelihood of an earthquake to occur on it. Indeed when the stress on the fault overcomes a critical value it will cause a slip along the direction of least resistance, which in the case of an unfractured medium, is determined by Anderson's theory of faulting. In support of this hypothesis, it has been observed (fig. 2.11) that there is a good spatial correlation between positive static Coulomb stress changes and aftershock distributions (Simpson (1994), King, Stein, and Lin (1994), Toda, Stein, Richards-Dinger, et al. (2005), Xu et al. (2010)). For this reason, methods employing the ΔCFS function (eq. 2.11) for simulating seismic rates in the presence of a source of stress change such as a mainshock or a dike emplacement, have been developed (see paragraph 2.7). In order to compute ΔCFS the parameters of the source, including geometry, position and slip (or opening) have to be determined. Moreover a receiver fault geometry, in terms of strike, dip and rake angles or of normal and slip vectors, has to be set. This can be set according to the expected or observed focal mechanism of an earthquake triggered by the stress change induced by the above-mentioned source.
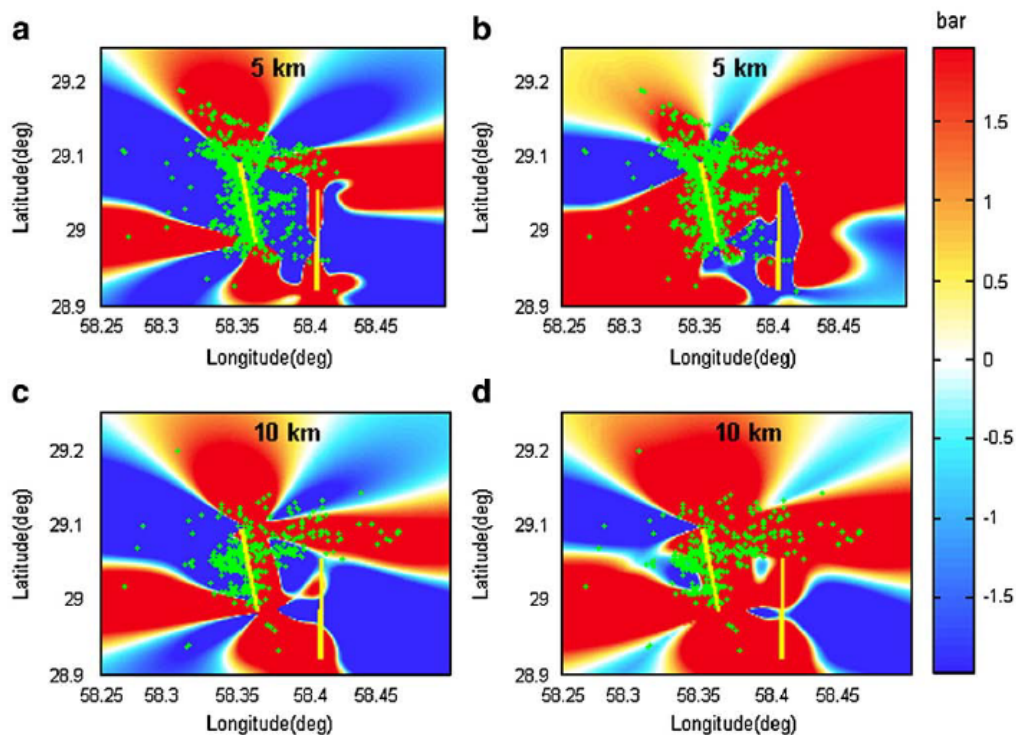
Figure 2.11: Maps at 5 and 10 km of depth, of the static Coulomb stress changes resolved on fixed receiver faults ((a) and (c)), parallel to the mainshock, and on OOPs ((b) and (d)), for the Mw 6.5 Bam earthquake of 2003. Figure from Xu et al. (2010).

2.6.3   Fixed fault orientations and OOPs

Depending on the problem, the receiver faults may have fixed geometry (see fig. 3.4) or may be 'optimally oriented', meaning that pre-existing cracks with all possible orientations exist in the medium, and those orientations receiving the largest Coulomb stress will fail (see fig. 3.5).

In published case studies on earthquake triggering, a variety of approaches have been adopted, including fixed orientation parallel to the mainshock fault, faults with fixed dip and rake angles, or the unified model proposed by Xu et al. (2010) in which all three angles of the faults correspond to degrees of freedom. In other words, the parameters for the optimization are the three angles instead of the sole strike angle. This was suggested by Mallman and Zoback (2007), who proposed that correlation between aftershocks and positive ΔCFS on receiver faults could be improved by means of Optimally Oriented Planes (OOPs). The OOPs are planes on which the Coulomb stress is maximum. In the most general case, theoretically, they can be obtained by finding the maximum of a functional of the type $f(\phi, \delta, \lambda)$, representing, respectively, the strike, dip and rake angles. In the case of an elastically uniform and uncracked medium, they are found by applying Anderson's theory of faulting. According to this theory, the OOPs are 2 planes forming an angle γ with respect to the most compressive axis on the plane of the minimum and maximum principal stresses (see fig. 3.3 as reference).

The angle γ depends on the friction coefficient as (*"Fundamentals of Structural Geology"* by Pollard and Fletcher (2005)):

$$\gamma = \frac{1}{2} tan^{-1}(\frac{1}{\mu'_{fr}}) \tag{2.12}$$

where μ'_{fr} is the effective coefficient of friction mentioned in eq. 2.11. The choice of OOPs in different locations of the region around a mainshock or a source of elastic deformation, seems the most reasonable in general cases, because aftershocks following a mainshock or earthquakes induced by a dike, can follow different focal mechanisms in different positions. Thus this type of fault planes can better represent the variability, in space and time and from event to event, of real episodes, than fixed fault planes that are chosen on the base of similar previously observed events. Nevertheless, fixed/aligned receiver faults can still be an effective choice, especially if the focal mechanisms of the observed seismicity are similar. In figure 2.11, as an example from Xu et al. (2010), are shown the Coulomb stress changes computed for the 2003 Mw 6.5 Bam earthquake, relatively to fixed (panels (a) and (c)) and optimally oriented planes (panels (b) and (d)), and the aftershocks' distribution. As it was said before, the OOPs increase the spatial correlation between aftershocks and positive Coulomb stress changes.

2.7   Seismicity rate models based on Coulomb stress changes

The main goal of seismicity rate models is to simulate, and eventually forecast, the changes in seismicity rates for the short (from days to weeks) and medium (months) period. There two classes of methods in this field, statistical and physics-based, although many methods are hybrid. The general purpose of these models is to test, apply and develop our understanding of the statistical properties (in case of statistical methods) or the causative physical mechanisms (in the case of physics-based methods) of seismicity with the ultimate goal of better estimating seismic hazard, so that effective operational earthquake forecasting can be achieved in the future. Although less exploited in the operational field than the statistical models, physics-based seismicity models are of great value because they seek to relate seismicity to physical quantities in order to clarify the cause-effect relationship between them. These models consider for instance the redistribution of stresses in the crust caused by rapid or slow slip/opening events on faults/dikes, respectively, or by postseismic relaxation. In particular those methods taking advantage of the Coulomb stress changes and of the rate-state constitutive law proposed by J. Dieterich (1994), are called Coulomb-rate-state models (CRS).

2.7.1   The rate-state seismicity evolution

In the context of earthquake triggering, aftershocks sequences are in general a good target for the study of physical mechanisms driving seismicity and for the development of forecasting models. That is because they are abundant and the first order features in space and time are well understood (for instance the well known Omori-Utsu law of the temporal decay of aftershocks, Utsu, Ogata, et al. (1995)). The triggering of earthquakes in the near-field, at a distance of a few fault lengths from a seismic source, is thought to be dominated by the stresses induced by static deformation (Felzer and Brodsky (2006), Hainzl, Moradpour, and Davidsen (2014)). Static stress transfer largely explains the spatial distribution of aftershocks and the scaling of their abundance with the size of the mainshock (magnitude). In contrast, if the location or abundance of triggered events evolve in time in a way that static stress changes cannot explain, then a time-dependent process should be considered. For this purpose, J. Dieterich (1994) introduced a constitutive law for the evolution of seismic events triggered by stress changes. He based it upon experimental results of frictional properties of rocks (J. H. Dieterich (1979)). The idea behind this theory is that, on a population of faults, the aftershocks' triggering caused by a sudden stress change may be delayed due to a finite time of nucleation (time-dependent frictional response). This theory for instance can describe an Omori-type time-dependent seismicity which decays with a power law after a instantaneous stress change.

The rate-state model (RS)

The rate-state model, theorized by J. Dieterich (1994) as a tool for simulating the changes in seismicity rates due to static stress changes, is based on a rate-sate friction law. The latter was

introduced in the widely used form:

$$\mu = \mu_0 + A log(\frac{v}{v_0}) + B log(\frac{\theta}{\theta_0}) \tag{2.13}$$

by J. H. Dieterich (1981) and Ruina (1983), where v is the sliding velocity, θ is a state variable depending on time, slip and normal stress; μ_0, A and B are coefficients determined experimentally. Eq. 2.13 is used to reproduce not only earthquake nucleation but also creep processes.
In the RS model other assumptions, besides the friction constitutive law, are made. Firstly it is considered that a large number of faults/sites exist in any given volume of the crust, for which the above-mentioned friction law holds and on which earthquakes can nucleate independently of each other. Secondly, in absence of a stress perturbation the system is characterized by a constant earthquake rate r_0, also known as background seismic rate. Lastly, the system is loaded by a constant tectonic stressing rate $\dot{\tau}$ which is the same before and after the earthquakes. The expected seismicity rate R, above a certain reference magnitude, is found to evolve according to eq. 2.14, where besides r_0 and $\dot{\tau}$, there is a dependence of R on the state variable γ.

$$R(t,\mathbf{x}) = \frac{r_0(\mathbf{x})}{\gamma(t)\dot{\tau}} \tag{2.14}$$

The evolution with time of the state variable γ is governed by the equation

$$d\gamma = \frac{1}{A\sigma_{tot}}(dt - \gamma dS) \tag{2.15}$$

where $\sigma_{tot} = \sigma_n + p$ is the effective normal stress, A is a dimensionless fault constitutive friction parameter (usually around 0.01, J. Dieterich (1994), J. Dieterich, Cayol, and Okubo (2000)). The steady state case, i.e. for $\frac{d\gamma}{dt} = 0$, takes the value:

$$\gamma_{ss} = \frac{1}{\dot{\tau}} \tag{2.16}$$

which gives $R = r_0$ according to eq. 2.14.

A related parameter to those of the RS model, is the aftershock duration time t_a (eq. 2.17), which controls the time taken by the seismicity to return to the background level r_0 after an instantaneous stress step (J. Dieterich (1994)). Indeed, it is observed that the rate-and-state model well reproduces the aftershock temporal behaviour after a mainshock earthquake event.

$$t_a = \frac{A\sigma}{\dot{\tau}} \tag{2.17}$$

This relation is sometimes used to estimate R-S model parameters from observed Omori decays.

Considering at a certain location $\mathbf{x}$ and a process involving a single stress step ΔS at time $t = 0$, it can be shown that the seismicity rate evolution $R(t)$ takes the following form (Hainzl, Steacy, and Marsan (2010)):

$$R(t) = \frac{r_0}{1 + [e^{-\frac{\Delta S}{A\sigma}} - 1]e^{-\frac{t}{t_a}}} \tag{2.18}$$

with the above-mentioned aftershock relaxation time t_a. If $t \ll t_a$, eq. 2.18 can be approximated as

$$R(t) \approx \frac{r_0}{\psi - (\psi - 1)\frac{t}{t_a}} \tag{2.19}$$

with $\psi = e^{-\frac{\Delta S}{A\sigma}}$ (Hainzl, Steacy, and Marsan (2010)). This latter equation has the form of the Omori-Utsu law for the decaying rate of aftershocks following a stress change step generated by a mainshock:

$$R(t) = \frac{K}{(t + c)^p} \tag{2.20}$$

with a p-value equal to 1 (typically from 0.7 to 1.5), the c-value given by $c = \frac{\psi t_a}{(1-\psi)}$ and the productivity $K = \frac{r_0 t_a}{(1-\psi)}$.

To sum up, in general, with eq. 2.14, after the estimation of parameters $r_0(\mathbf{x})$ and $\dot{\tau}$ in the region under study, the calculation of $\gamma(t)$ for a particular history of the stress field in the same region, allows to estimate the time variation of the seismicity rate $R(t)$ (for earthquakes over a magnitude of reference) in a certain location $\mathbf{x}$, as it will be shown for a particular case in the next paragraph. Moreover for the particular case of a single Coulomb stress change step ΔS in a certain location, the time variation of the seismic rate $R(t)$ is given once the parameters r_0, $A\sigma$ and t_a are estimated and, following the eq. 2.18, the stress change ΔS is set as input.

2.7.2   Implementation of the model for an arbitrary stress history

The model can be adapted to the case of an arbitrary stress history. For the implementation of the rate-state model in this context, there is an algorithm (eq. 2.22) by Hainzl, Steacy, and Marsan (2010), which, given the model parameters, provides seismicity rates for an arbitrary step-like stressing history.

Algorithm for multiple stress-steps with constant stressing rate

Considering a scenario of a series of stress jumps ΔS_k at times t_k, with $k = 1, ..., K$, caused for example by the coseismic slip of a mainshock followed by afterslip, or by a propagating

dike, the seismicity rate can be computed by applying the following procedure to eq. 2.14, supposing the stressing rate $\dot{\tau}$ and the background seismicity rate r_0 constant.

The procedure steps are:

1. Before the first stress step ($t < t_1$), $\gamma(t) = \gamma_0 = \frac{1}{\dot{\tau}}$ and therefore $R(t) = r_0$ is the background seismic rate;

2. After the first step and before the second ($t_1 \leq t < t_2$),

$$\gamma(t) = \frac{1}{\dot{\tau}} + (\gamma_0 e^{-\frac{\Delta S_1}{A\sigma}} - \frac{1}{\dot{\tau}})e^{-\frac{t-t_1}{t_a}};$$

3. The correspondent seismic rate $R(t)$ is calculated with eq. 2.14 (this is also applied in next steps after every new calculation of $\gamma(t)$);

4. For the time interval $t_2 \leq t < t_3$, before calculating $\gamma(t)$, the parameter γ_k is calculated according to:

$$\gamma_1 = \frac{1}{\dot{\tau}} + (\gamma_0 e^{-\frac{\Delta S_1}{A\sigma}} - \frac{1}{\dot{\tau}})e^{-\frac{t_2-t_1}{t_a}};$$

5. Then, the state variable is updated:

$$\gamma(t) = \frac{1}{\dot{\tau}} + (\gamma_1 e^{-\frac{\Delta S_2}{A\sigma}} - \frac{1}{\dot{\tau}})e^{-\frac{t-t_2}{t_a}}$$

using the parameter γ_1 just obtained;

6. The procedure is iterated, first updating the parameter γ_i with eq. 2.21 and then calculating the respective $\gamma(t)$ with eq. 2.22 (where γ_{k-1} is γ_i);

$$\gamma_i = \frac{1}{\dot{\tau}} + (\gamma_{i-1} e^{-\frac{\Delta S_i}{A\sigma}} - \frac{1}{\dot{\tau}})e^{-\frac{t_{i+1}-t_i}{t_a}} \tag{2.21}$$

$$\gamma(t) = \frac{1}{\dot{\tau}} + (\gamma_{k-1} e^{-\frac{\Delta S_k}{A\sigma}} - \frac{1}{\dot{\tau}})e^{-\frac{t-t_k}{t_a}} \tag{2.22}$$

7. After the last event, $t > t_K$, the state variable is given by $\gamma(t) = \frac{1}{\dot{\tau}} + (\gamma_{K-1} e^{-\frac{\Delta S_K}{A\sigma}} - \frac{1}{\dot{\tau}})e^{-\frac{t-t_K}{t_a}}$.

In the limit of sufficiently small time steps Δt, these formulas can be extended to an arbitrary stressing history $S(t)$ which may be the resulting effect of tectonic stressing together with coseismic, postseismic and dynamic stress changes (Hainzl, Steacy, and Marsan (2010)).

Chapter 3

Simulations of seismicity rates for a propagating dike

In this chapter, I apply the models presented in the previous chapter to calculate the stress changes induced/imparted by a moving dike and to estimate the expected triggered seismicity rates. I approximate the moving dike quasi-statically, as a series of snapshots taken at different times along the propagation trajectory. At every snapshot, I simulate the intrusion as a Boundary Element dike composed with rectangular tensile dislocations, modelling them as static sources of stress change. I assume the quasi-static approximation holds because the dike is moving at a velocity that, in comparison with the speed of sound in rock, is much smaller. The long-term goal of this thesis is to contribute to a better insight on the properties of the seismicity induced by natural fluid-filled propagating cracks, and to progress on validating physical-based models devised to reproduce such induced seismicity. With this purpose in mind, I have devised two different simplified scenarios that capture some essential characteristics of the natural process. I intend to test models against observed patterns of seismicity, starting from simple ones, to verify if they can reproduce the observed spatio-temporal distributions of seismicity and, thus, if they capture the dominant physical factors of the phenomenon. In this thesis, I aim to pave the way for future more complex applications of this models for forecasting the seismicity due to propagating magmatic intrusions and man-made fluid injections.

I focus on producing simple simulations for the propagation phase (5 days) of the 2000 dike at Miyakejima volcano, described in chapter 1. For the stress computations, I use MATLAB codes that I have written and that employ the *RDstressFS* and *RDstressHS* functions by Nikkhoo et al. (2016). These functions compute the stresses generated by rectangular dislocations (RD) in full and half-spaces.

In the first part I present a simple example of application of the Coulomb stress change calculation, for a single rectangular dislocation, in order to show what kinds of patterns can be obtained for different parameters' conditions. Then I present an example of boundary elements dike representing a more complex model of the source of deformation, which is needed when dealing with stresses induced in the near field.

In the second section I describe the first scenario of simulated seismicity. In this simplified case, a circular horizontal teardrop-shaped dike propagates horizontally at a constant velocity, equal to the average speed of the Miyakejima dike. The depth of the source is also constant. Given the source of deformation I then calculate the Coulomb stress changes and the consequent seismicity rates using the rate-and-state model on a discretized spatial grid.

In the third section I present the second scenario of seismicity induced by a propagating dike. This second case is more complex than the previous one, adding a new element of the natural Miyakejima dike, which is a variable surface topography along the dike's path. The teardrop-shaped dike, whose shape is given by a horizontal gradient in the external stress field, still moves horizontally at the same depth, but under a variable surface topography, and, thus, variable normal stress. The latter is a factor not yet extensively considered in literature when simulating seismicity induced by a propagating dike, and so it is quite new. In this context the opening distribution and velocity of the dike undergo changes while it moves, influencing the related seismic rates' spatio-temporal pattern.

3.1 Examples of Coulomb stress change generation and a static boundary elements dike

3.1.1 A simple example of Coulomb stress calculation

The Coulomb approach has been widely used to seek potential correlation between changes of *CFS*, caused for example by an earthquake main shock, and the spatial distribution of the subsequent aftershocks. Less often it has been applied to a tensile source, which is the case of this study. Since positive values of Coulomb stress changes promote slip, in absence of more specific geological information that may help building a more detailed model, it is expected that earthquakes will be triggered in the areas of positive change (red areas in following figures). Conversely they will be suppressed where the change is negative (blue areas).
Here I construct simple applications of a ΔCFS calculation to shear and tensile sources of stress change, to show the spatial patterns they produce. Figures are freely inspired by some of the images by King, Stein, and Lin (1994).
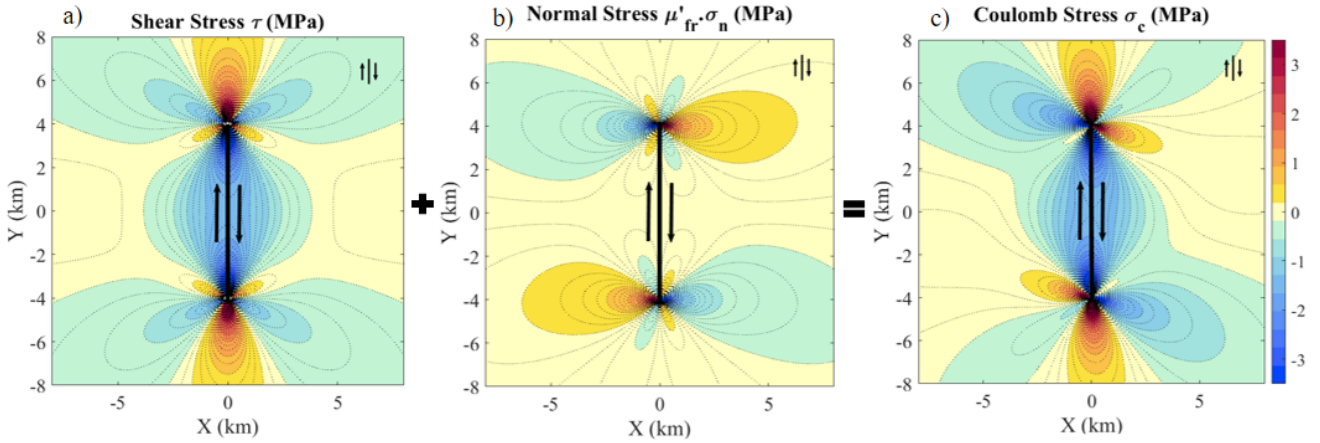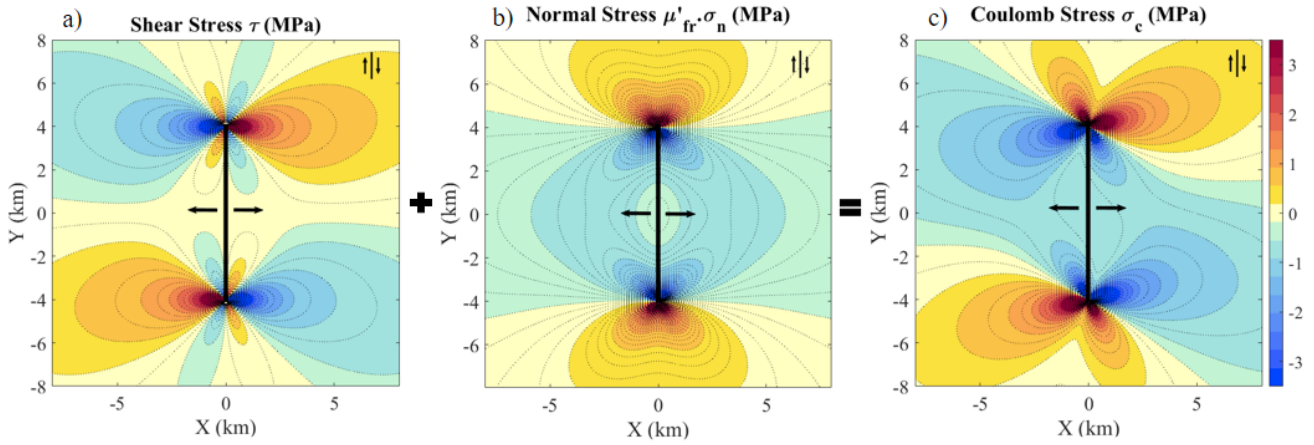
Figure 3.1: Map view of static stress changes for a vertical strike slip dislocation, on a plane parallel to the free surface at a 2 km depth. The source is a rectangular dislocation 8 km long and 6 km wide with its center point 5 km distant from the surface and a slip of 1 m. a) shear, b) rescaled normal and c) Coulomb stresses for receiver faults of the same geometry of the source (orientation is shown in the insets in the top right corners of all panels). The values of stress change (MPa) exceed the colorbar range near the source edges.

In fig. 3.1 I show the static stress changes generated by a vertical right-lateral strike slip fault on receiver faults with the same orientation. The fault is modelled as a finite rectangular dislocation in an elastic half-space (stress computing codes by Nikkhoo et al. (2016)). The first two panels show the spatial distribution of the components of the Coulomb stress of eq. 2.11, of which the last panel is the sum. Values are reported on a color scale from blue, for the most negative changes, to red for the most positive ones. According to the Coulomb stress analysis, in panel c) we expect an increase of vertical right-lateral strike slip events in the orange/red areas and a decrease of them in the blue ones.

Fig. 3.2 shows the contour plots of the stress changes for the same receiver faults' geometry of the first scenario but in case of opening of a tensile rectangular dislocation. The source has the same dimensions of the previous source but it undergoes opening instead of slip. Comparing the two examples shows clearly how shear and normal stresses have different patterns while for the resulting Coulomb stresses some basic similarities can be recognized: a negative diagonal band and two pairs of positive lobes in the upper-right and lower-left sides of the sources. This highlights how it may be difficult to constrain the type of source (tensile or shear), given a pattern of observed seismicity, if there is no other physical information. It is important to remind that the pattern depends on both the source and the receiver faults.

If a regional stress field is taken into account, as in King, Stein, and Lin (1994), this may inform the choice of the receiver faults' geometry, that can be chosen consistent with such pre-stress condition. Another good option is to assume optimally oriented faults (OOPs, see also paragraph 2.6.3) for which the Coulomb stress is maximized. For the simulation of fig. 3.4 I apply a regional uniaxial stress with the most compressive principal axis forming a clockwise
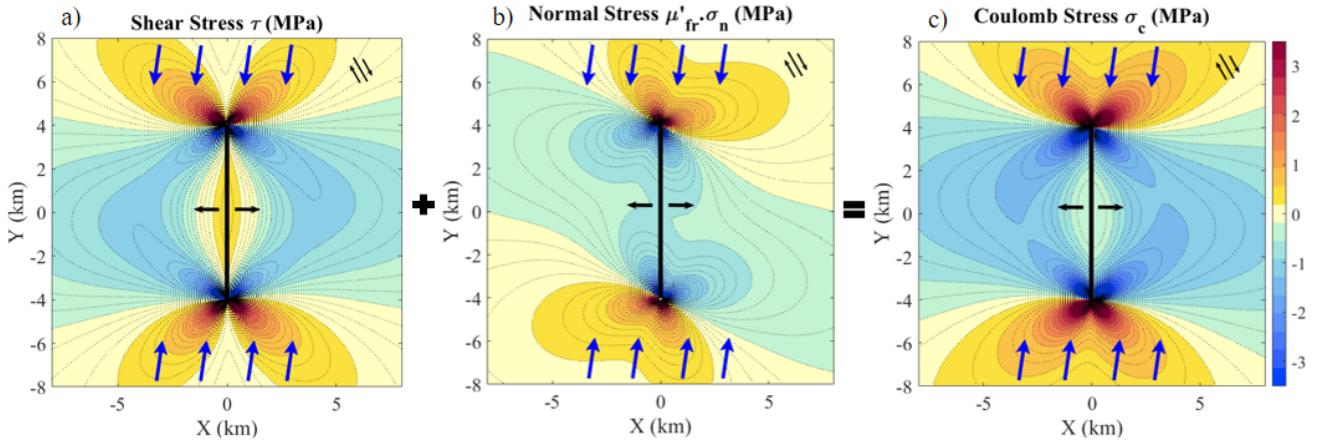
Figure 3.2: Map view of static stress changes for a vertical tensile dislocation, on a plane parallel to the free surface at a 2 km depth. The source is a rectangular dislocation 8 km long and 6 km wide with its center point 5 km distant from the surface and an opening of 1 m. a) shear, b) rescaled normal and c) Coulomb stresses for receiver faults of the same geometry of fig. 3.1 (orientation is shown in the insets in the top right corners of all panels). The values of stress change (MPa) exceed the colorbar range near the source edges.

angle of 7° with respect to the y-axis, and the other principal stresses negligible with respect to the former.
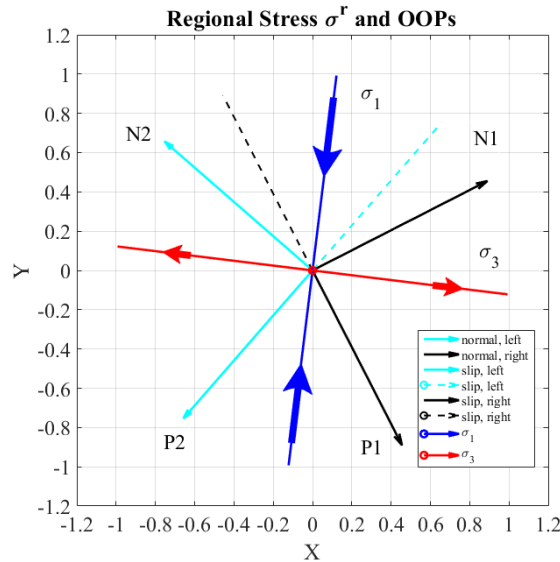
Figure 3.3: Principal values and axes of the regional stress in map view (xy-plane). Principal stresses: $\sigma_1 = 10$ MPa and σ_2 and σ_3 negligible with respect to the former. In the plane of the most and the least compressive axes there is a couple of OOPs: in black the right-lateral fault and in cyan the left-lateral one. In blue is indicated the most compressive principal axis and in red the extensional one.

Figure 3.4: Map view of static stress changes for a vertical tensile dislocation, on a plane parallel to the free surface at a 2 km depth. The source is a rectangular dislocation 8 km long and 6 km wide with its center point 5 km distant from the surface and an opening of 1 m. a) shear, b) rescaled normal and c) Coulomb stresses for receiver faults which are right-lateral vertical OOPs (orientation is shown in the insets in the top right corners of all panels). The values of stress change (MPa) exceed the colorbar range near the source edges. Blue arrows indicate the direction of the compressive component of the regional stress.

As it can be seen in fig. 3.3 there are two OOPs relative to the regional stress examined, which are vertical strike slip faults. Properly the OOPs are generally considered varying from location to location accordingly to the total stress in a certain place, given by the regional stress added to that of a new source. In this case I mean that the fault planes considered are optimal oriented relatively to only the regional stress, assumed uniform in all the area under study. The fault planes obtained are in accordance with the Anderson's theory of faulting that predicts two optimal directions of slip, in relation with the most and the least compressive principal axes of stress, depending on the coefficient of friction. In this case, for the Coulomb stress calculation I choose the right-lateral one, as shown in the insets of the figures, and I consider it as the receiver fault for the Coulomb stress change calculation in every point of the xy-plane. Fig. 3.4 shows the stress pattern induced by a tensile source that opens in a pre-stressed region, on right-lateral vertical OOPs. It can be seen that if the receiver faults are rotated determined for instance by a preexisting stress field, has a clear influence on the static stress change of the receiver faults themselves. If I had chosen the left-lateral configuration I would have found an identical Coulomb stress but different shear and normal ones. The case plotted in fig. 3.4 is realistic because in general tensile sources like dikes open along the direction of the least compressive principal deviatoric stress but sometimes along small deviations of that direction (Ruch et al. (2016), Passarelli et al. (2015)).

A more detailed evaluation of the Coulomb stress changes induced by a source of stress change in a certain location, can be made considering in each point of the xy-plane the OOPs relative to the total stress given by the regional stress and that generated by the source. For

instance, I use a regional stress field given by equation 3.4, in a cartesian reference frame with the z-axis perpendicular to the horizontal xy-plane represented in figure 3.5, and a stress field with the following (deviatoric, thus with lithostatic pressure removed) principal stresses, from the most to the least compressive: $\sigma_1 = -10$ MPa and $\sigma_2 = 0$ MPa and $\sigma_3 = 1$ MPa.

$$\sigma_r = \begin{pmatrix} \sigma_3 & 0 & 0 \\ 0 & \sigma_1 & 0 \\ 0 & 0 & \sigma_2 \end{pmatrix} \tag{3.1}$$

The source is a tensile vertical rectangular dislocation, 4 km long and 3 km wide, with an opening of 0.5 m and a depth of 5 km. Following the above-mentioned Anderson's theory of faulting, the optimally oriented point-faults, which are chosen left-lateral with respect to the most and the least compressive principal axes of stress, are displayed in figure 3.5, for a plane parallel to the free surface ad intersecting the dislocation at its midpoint. As shown in the figure, on one hand the orientation of the OOPs is consistent with the regional stress from about one source length away from the dislocation. On the other hand, in the central portion of the figure, near the dislocation, the influence of the stress changes modifies the direction of the least compressive principal stress axis, inducing a tilt of the OOPs. This result highlights the importance of considering optimally oriented planes when dealing with intense sources of stress changes and in general for near-source evaluations of Coulomb stress changes. In figure 3.5 are also reported the Coulomb stress changes generated from the tensile crack, relative to the OOPs estimated.

Although theoretically the OOPs can be preferred instead of fixed receiver faults, they can still be affected by errors. If the stress field is not well known, its uncertainties propagate onto the determination of the OOPs giving an uncertainty on the Coulomb stress change. Thus considering this type of receiver faults makes the treatment of the phenomenon more complex also from a computational point of view. At the stage of modelling of my scenarios of next sections, to maintain them simple, and since I have no detailed information on the stress field before the dike emplacement, I choose to evaluate the Coulomb stresses on fixed receiver faults. The choice of the receiver faults will be made upon the focal mechanisms expected for the stress field of a tensile dislocation and on the basis of field observations, as I will discuss in next sections.

Since my simulations address also the near field of the dike, I need to represent the source of deformation and of Coulomb stress changes with more details. As shown in fig. 2.11 (see chapter 2), relative to the Mw 6.5 Bam earthquake of 2003, the correlation between the spatial distribution of the aftershocks and the positive Coulomb stress changes is good in the far field. In that case the source of stress change, a mainshock earthquake, is represented by a single rectangular shear dislocation. To improve the above-mentioned correlation in the near field, the source of stress and deformation can be modelled with boundary elements. Indeed in this way the single dislocation is replaced by multiple and smaller dislocations making the source
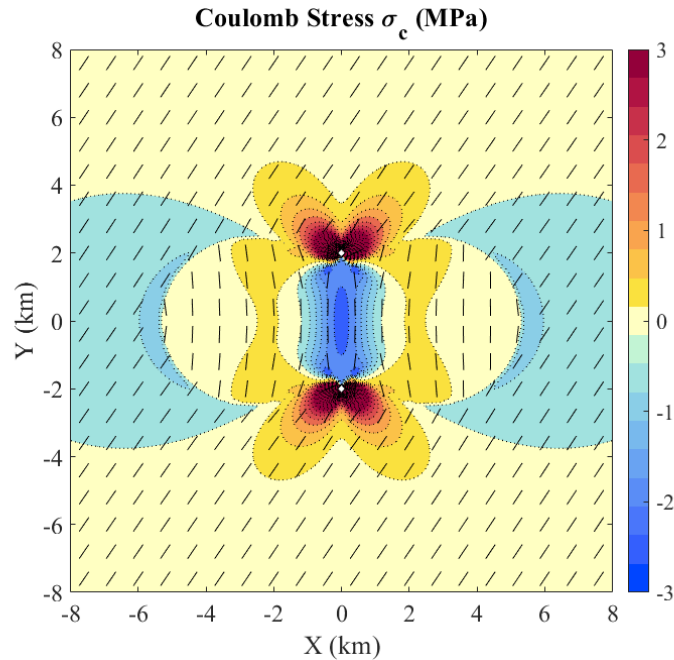
Figure 3.5: Map view of static Coulomb stress change generated by a vertical rectangular tensile dislocation on OOPs. The optimally oriented planes are calculated in each point of the xy-plane according to the Anderson's theory of faulting, relative to the total stress field, given by the regional stress (eq. 3.4) and the source stress. The source is 4 km long extending in the y-axis direction, 3km deep, centered at a depth of 5 km from the free surface and with an opening of 0.5 m.

more detailed and the edge effects reduced in space. In the case of earthquakes the source surface can be very complex to model due to the great heterogeneity of the friction in the host rock. In contrast, the presence of a fluid in fluid-filled intrusion sources, makes them of a simpler shape and so easier to represent with more details and less approximation through boundary elements.

In the next paragraph I describe the model of dike I have implemented with boundary elements for the seismicity simulations. I also show an example of dike in the more general case of an ellipsoidal cross section crack.

3.1.2 A teardrop-shaped dike represented with BEM

In order to build a realistic representation of a dike source, that will be used for seismic simulations in next sections, I have to set a certain distribution of the boundary elements and the conditions on the stresses at the crack boundaries. Here I develop a source model taking inspiration from the analytical and numerical simulations by Davis, Eleonora Rivalta, and Dahm (2020) (fig. 3.6). I create an elliptical domain of RD elements in the y-z plane (fig. 3.7) and apply a horizontal pressure gradient $\Delta\gamma$.
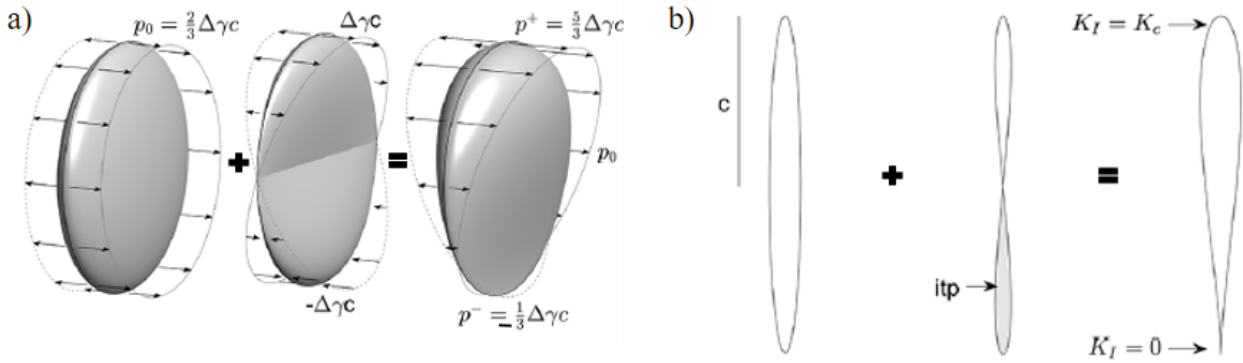

Figure 3.6: a) penny-shaped crack with different overpressure conditions, the right one is given by the combination of the first two: uniform pressure and vertical linear gradient cases respectively. b) vertical sections of the cracks of part a). Modified from davis2020critical.

The boundary conditions of pressure at the left (-) and right (+) edges of the crack I impose are the following:

$$p^{\pm} = (\frac{2}{3} \pm 1)\Delta\gamma c \tag{3.2}$$

which are obtained setting $K = K_c$ (critical value, here of about 10^8 $Pam^{0.5}$ (Maccaferri, Eleonora Rivalta, Passarelli, and Aoki (2016))) at the rightmost end and to zero at the leftmost one (see fig. 3.6). In this case c corresponds to the major semi-axis of the ellipse. Since this conditions are suited for a penny-shaped crack (circular domain of discretization) and the limitation given by a discretized domain, the simulated source I obtain (fig. 3.7), does not perfectly close at the edges. An elongated crack instead of a circular one better reproduces various scenarios both in numerical simulations (Davis, Eleonora Rivalta, and Dahm (2020)) and analog laboratory experiments (Eleonora Rivalta and Dahm (2006)). The following figures (fig. 3.10, 3.8, 3.9) show the geometry of the crack in two cross sections and a perspective view in 3D. The last figure (3.11) illustrates the oversimplification of representing an intrusion with a single rectangular dislocation. In the following sections I will use a BEM dike propagating horizontally and subject to a horizontal linear gradient, taking a circular discretized dike rather than ellipsoidal.
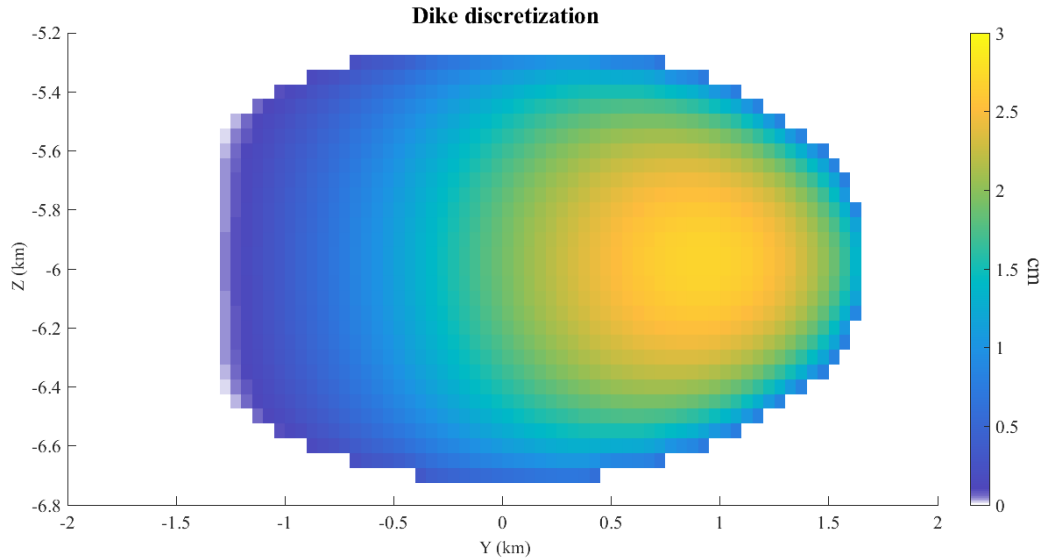
Figure 3.7: Vertical section view of the ellipsoidal crack domain in the y-z plane. The minor semi-axis is of 0.75 km while the major one is of 1.65 km. Rectangular elements are equiareal of 0.05x0.05 km^2. The color scale that shows half of the opening of each patch is in cm.
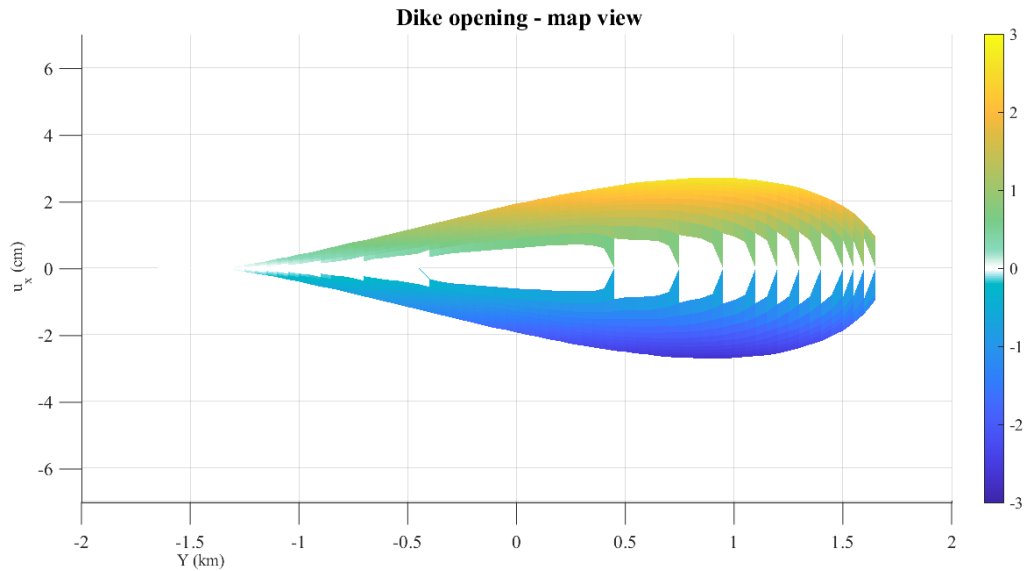

Figure 3.8: Map view of the u_x component of the displacement of the RDs, values in cm.
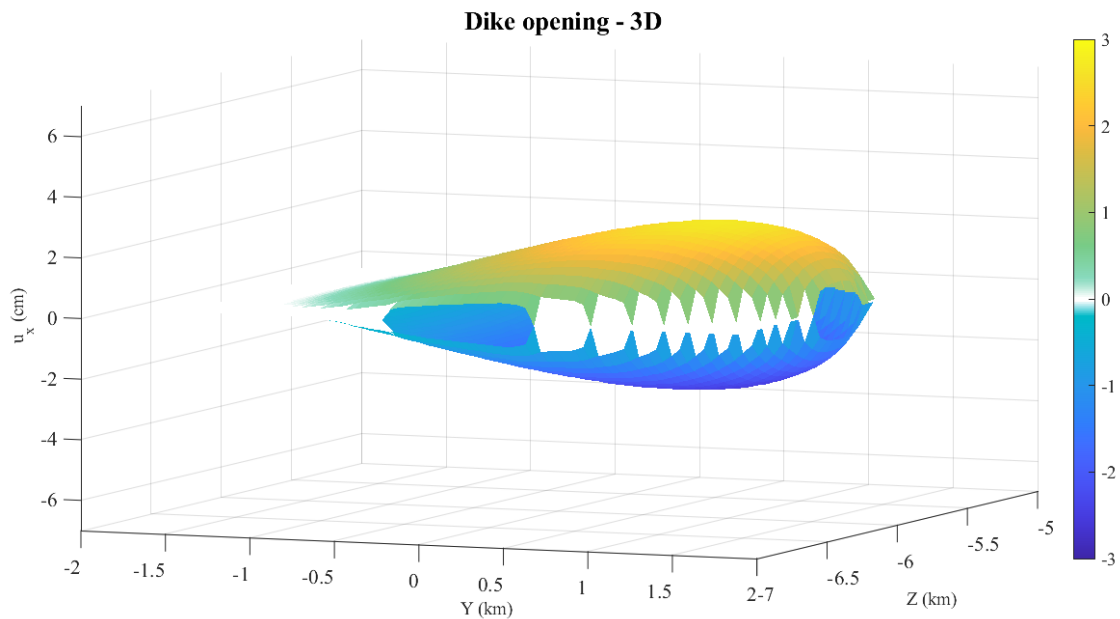
Figure 3.9: 3D representation of the ellipsoidal dike. The dike is rotated of 90° about an axis parallel to the y-axis of the figure, i.e. is lying horizontally. The vertical dimension is the displacement of the boundary elements while the dike is vertical in the y-x plane. The displacement is in cm and the density contrast used here is of 100 Kg/m^3.
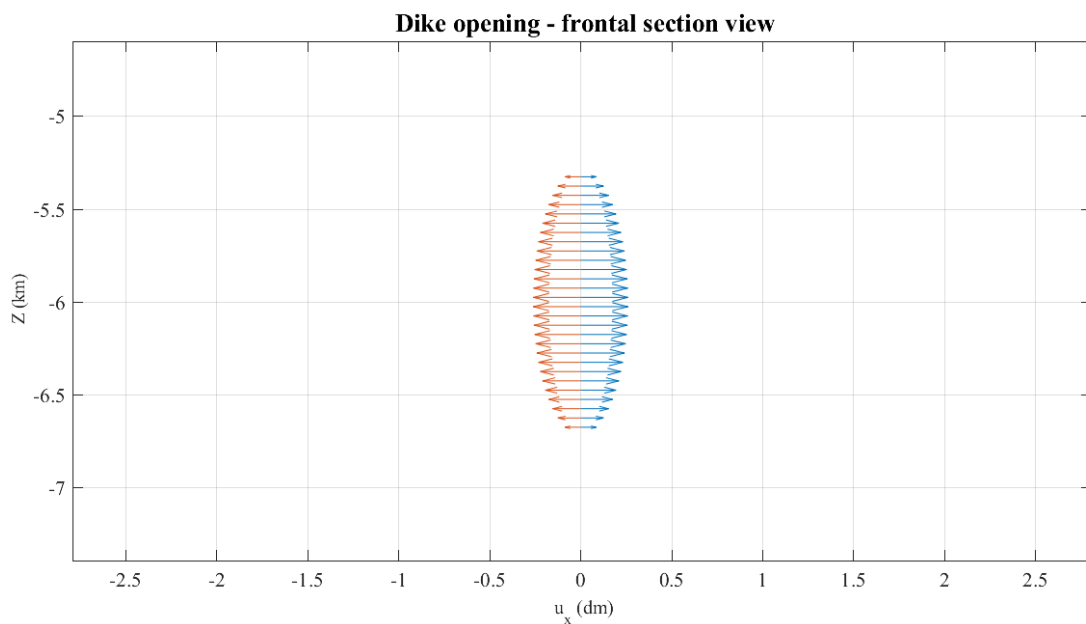
Figure 3.10: Vertical frontal cross section in the x-z plane (at mid-length), of the u_x component of the displacement of the RDs, values in dm.
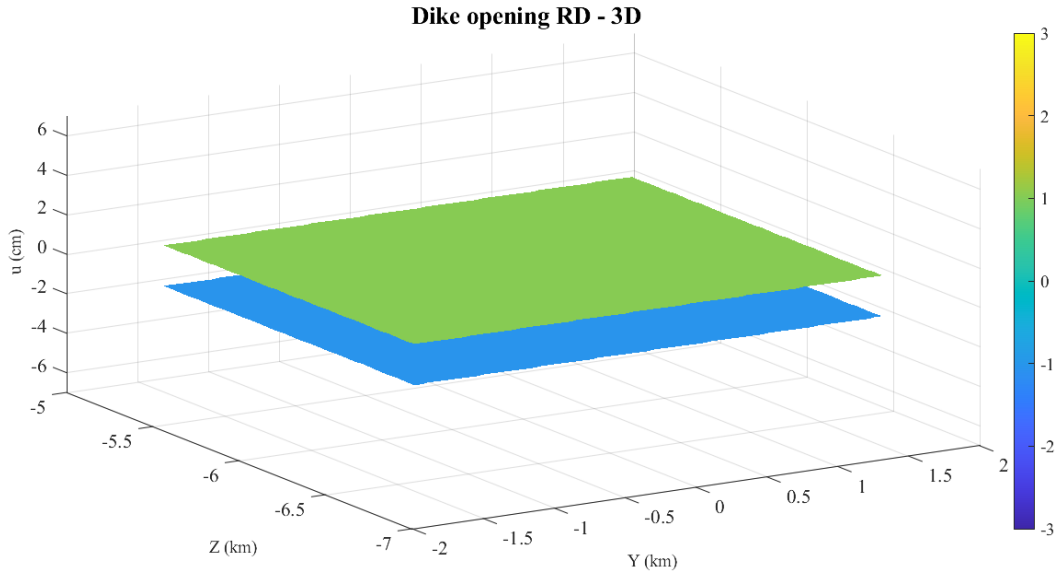
Figure 3.11: 3D representation of the dike if modelled with a single RD of opening equal to the mean one of fig. 3.9. The dike is rotated of 90° about an axis parallel to the y-axis of the figure, i.e. is lying horizontally. The vertical dimension is the displacement (cm) of the dislocation. The density contrast used here is of 100 Kg/m^3.

3.2 Scenario 1: constant shape and velocity

The first scenario involves a circular dike subject to a linear pressure gradient (section 3.1.2), propagating horizontally. Relatively to a Cartesian right-handed reference system with x and y axes horizontal and the z-axis vertical and positive upward, the dike lies on the yz-plane and propagates in the y-direction. I assume that the dike keeps its shape and volume while propagating at constant velocity. In the following paragraphs I will illustrate the time and spatial grids I used for the calculations of the stress changes and the corresponding simulated seismic rates and the characteristics of the dike and of the receiver faults.

3.2.1 Computational grids and temporal discretization

The dike center is initially positioned on the yz-plane at a depth of 4.4 km and at a horizontal distance of 4 km from the origin of the reference system, along the y-axis. The dike lies in the yz-plane for all the steps of its temporal evolution (as reference see fig. 3.12). To build the dike geometry I used the analytical model of Davis, Eleonora Rivalta, and Dahm (2020) as presented in chapter 2. It has a circular cross section of radius c while its thickness varies from point to point over the cross section. The distributed opening, which is calculated through boundary elements, is due to a horizontal overpressure linear gradient $\Delta\gamma$, such that along the direction of the gradient the thickness takes the shape of an elongated teardrop. The pressure
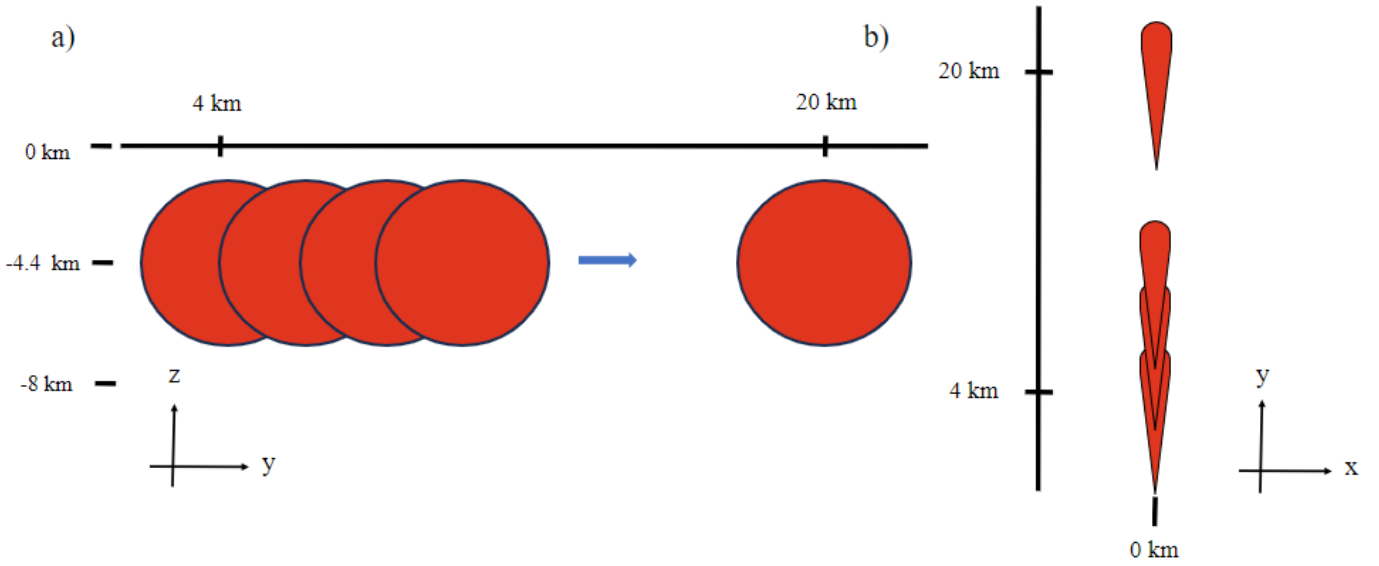
Figure 3.12: Schematic illustration, in cross section (a) and map view (b), of the evolution of the propagating dike described in scenario 1.

along the horizontal extension of the dike is determined following the analytical model Davis, Eleonora Rivalta, and Dahm (2020) which prescribes the pressures at the two extremities ($p^{\pm}$) considering between them a constant increase per unit length, given by γ.

Along the direction perpendicular to the overpressure gradient, the overpressure is uniform. The opening approaches zero towards the edges of the crack. I set the diameter of the crack at about 6 km and the overpressure linear gradient at 1550 Pam^{-1}. For a $\Delta\gamma$ given by a topographic loading, holds the relation $\Delta\gamma = \frac{Hg\rho_{rock}}{L}$, in which ρ_{rock} is the rock density, g the gravitational acceleration, L the horizontal extension of the topography above the dike and H the difference in height of the topography, between the front and the back of the dike. The overpressure gradient I set, would be given for example by $H = 330$ m, $L = 6$ km and a $\rho_{rock} = 2800$ kgm^{-3}. I calculate the opening with boundary elements using 749 patches and considering the intrusion within an half-space, resulting in a mean and a max openings of about 12 and 30 cm respectively. For visual reference see fig. 3.13 and 3.14.

The spatial grid of calculus has equal steps Δx, Δy and Δz in the three Cartesian directions. I use $\Delta x = \Delta y = \Delta z = 0.4$ km, with x ranging from -6.2 km to 6.2 km, y ranging from -1.2 km to 29.2 km and z ranging from -9.0 km to -0.2 km.

For the spatio-temporal evolution of the dike, I chose to apply spatial steps of 0.4 km (equal to the grid step) in the positive direction of the y-axis, maintaining constant the z and x coordinates of the dike center. Later I will also consider a larger spatial step of 4 km with the purpose of evaluating the effects of a coarser discretization of motion on the modelled seismic rates.
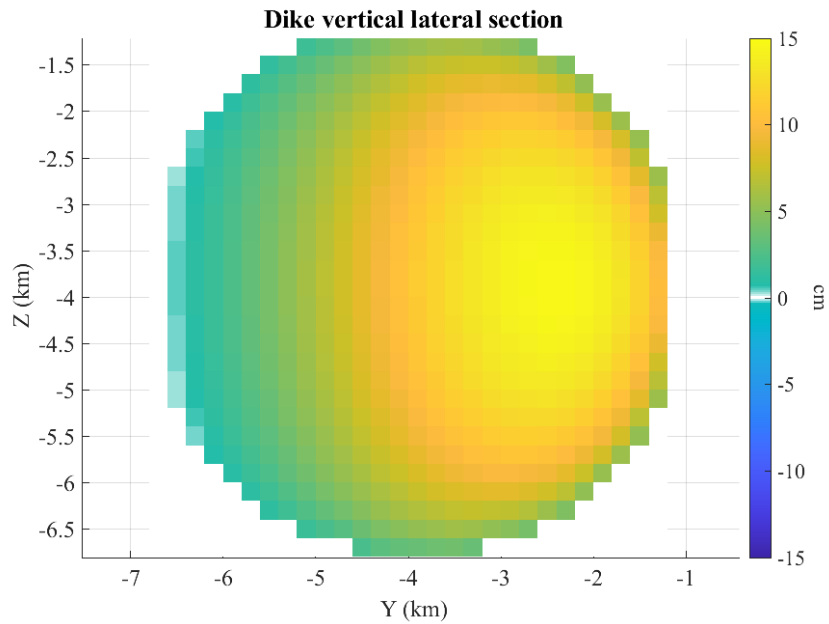
Figure 3.13: Vertical lateral cross section of the circular dike used in the simulation of the first scenario. The diameter is about 6 km and the source is calculated through 31x31 boundary elements in a half-space. In the figure only half of the opening (cm) of each patch is shown, the other half is symmetric. The initial coordinates of the center, for the simulation (not represented here) are: (0,4,-4.4) km.
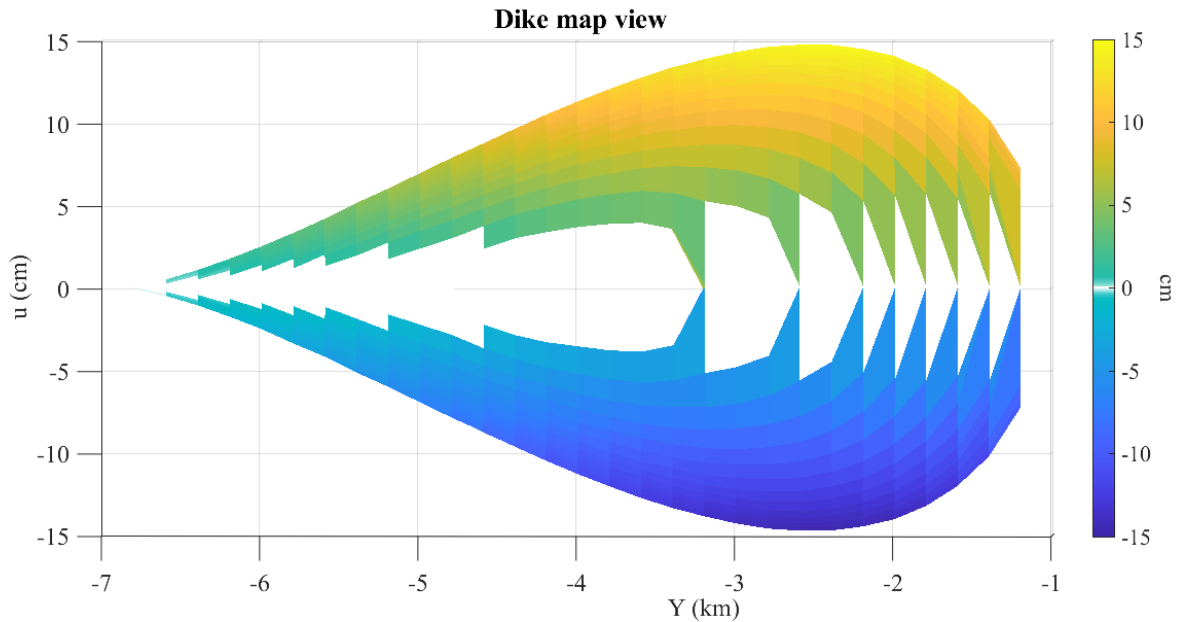
Figure 3.14: Map view of the same dike of fig. 3.13. Note that the scales of the two axes are different.

For the velocity I use the equation

$$v = \frac{4(1-\nu)}{27\pi^2\mu} \frac{\Delta\gamma^2 V}{\eta} \tag{3.3}$$

by Davis, Eleonora Rivalta, Smittarello, et al. (2023),where $\mu = 33$ GPa is the rigidity, $\nu = 0.25$ is the Poisson's ratio, $V = 5.8 \cdot 10^6$ m^3 is the critical volume and $\eta = 100$ Pas is the fluid viscosity. Eq. 3.3 is valid for a fluid-filled intrusion with constant and near critical (or greater) volume (see as reference for a basaltic dike Davis, Eleonora Rivalta, Smittarello, et al. (2023)).

With the numerical values indicated, $v = 0.047$ ms^{-1} which is very close to the quasi-stationary velocity of 0.05 ms^{-1} of the first days of seismicity evolution of the 2000 Miyake-jima dike (see Maccaferri, Eleonora Rivalta, Passarelli, and Aoki (2016)). As a consequence of velocity and spatial step assumptions, the time array is chosen extending from 0 to 7 days, divided into time steps of 2.5 hours.

The simulation starts with the dike emplacement after the first time step, then it continues with the dike propagating of Δs every time step Δt for 40 spatial steps in total. Then it stops after had traveled for about 16 km, while the seismicity simulation continues for another 2 days.

3.2.2 Stress changes calculation and receiver faults

For the stress change calculations needed for the seismic rate formula implementation I use the MATLAB code in appendix A. Firstly I compute the stress changes on the spatial grid, induced by the tensile dislocations resulting from the opening of the dike source, estimated through the boundary element method previously mentioned. The stresses are evaluated for every shift of the dike in the y direction. Afterwards I compute the ΔCFS for every dike position and in each grid point, assuming a prescribed fault orientation of the receiver faults, which is taken the same everywhere.

The receiver faults are determined as OOPs relative to a regional tectonic stressing rate field which is set, all over the computing volume, as:

$$\dot{\sigma}_r = \begin{pmatrix} \dot{\sigma}_{xx} & 0 & 0 \\ 0 & \dot{\sigma}_{yy} & 0 \\ 0 & 0 & \dot{\sigma}_{zz} \end{pmatrix} \tag{3.4}$$

where $\dot{\sigma}_{xx} = 25$ kPayr^{-1} is extensional while $\dot{\sigma}_{yy}$ and $\dot{\sigma}_{zz}$ are compressive and four orders of magnitude lower than the former. The stressing rate is chosen in order to be tensile in the direction of opening of the dike because often magma intrusions are oriented perpendicular to the minimum compressive axis of stress. This configuration of receiver faults allows to

compute the Coulomb stress changes in a simpler way because it assumes that the stresses induced by the dike do not produce relevant tilting of the OOPs and so only the regional stress is taken into account for the computation of the optimal planes. Thus the receiver faults are fixed: constant in time and uniform in space (i.e. the same in each grid point) throughout the whole simulation. The fixed receiver faults are two couples (fig. 3.15): one of normal dip-slip faults with $dip \approx 56°$ and one of vertical strike-slip faults.
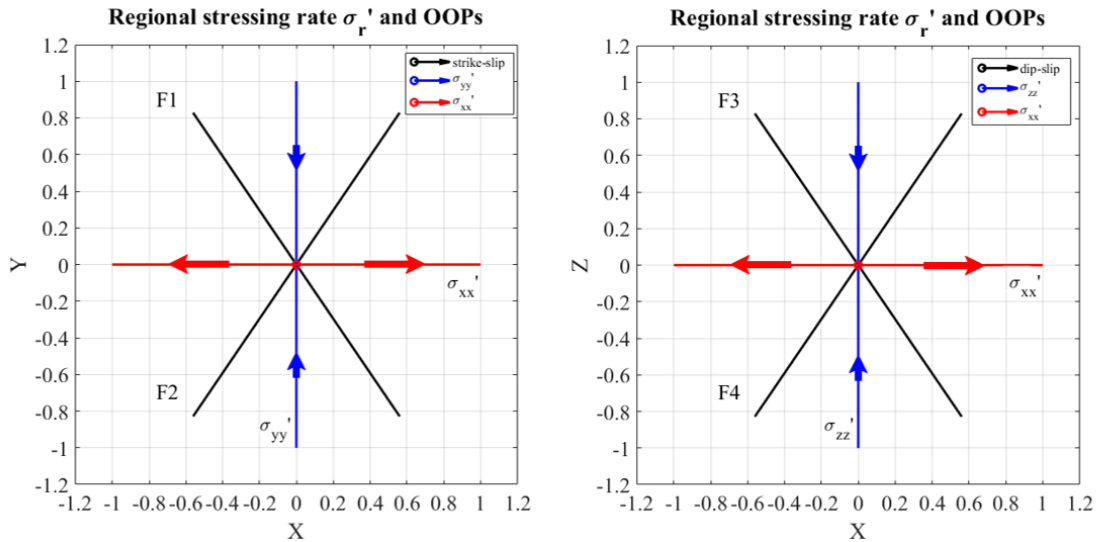

Figure 3.15: Fixed receiver faults for scenario 1, relative to an uniaxial stressing rate field in which the principal axis in the x direction is extensional and the principal axes in the y and z direction are compressive, a lot smaller than the former and similar to each other. F1 and F2 are a couple of vertical strike-slip faults while F3 and F4 are a couple of normal dip-slip faults. These are the receiver faults geometries considered for the simulations.

It is important to add another assumption on the computation of the Coulomb stress changes. Since the stresses are derived by rectangular dislocation sources and the minimum distance from their edges is equal to a dislocation length (0.2 km), in order to avoid singularities of the RD solutions, I impose a cut-off value for ΔCFS of 0.5 MPa. It is a common approach, for example Cattania (2015) uses values of 10 MPa and 1 MPa in modelling aftershock sequences with the rate-and-state seismicity model for respectively the M_w 9.0 Tohoku earthquake of 2011 and M_w 6.0 Parkfield earthquake of 2004.

3.2.3 Relative seismic rate simulations

The seismicity rates I compute in my simulations are relative seismic rates R/r_0 from which, once the background seismic rate r_0, relative to a magnitude of completeness M_c and a certain computing volume, is estimated, the absolute rates R are determined in a straightforward way by multiplication with the former rates. Generally r_0 can be evaluated by examining seismic catalogues of the region under study.

In my MATLAB script I implement equations 2.22 and 2.21 in each point of the spatial grid and for every time step. The parameters of the rate-state model $A\sigma$ and $\dot{\tau}$ are set respectively to 0.05 MPa, taking as reference the range of values $0.01 - 0.1$ MPa, and 0.012 MPayr^{-1}, which is obtained projecting σ_{xx} on the receiver fault planes; these values are within the range used in literature (see Dahm and Hainzl (2022) and Toda, Stein, and Sagiya (2002)). This choice of values gives a decay time of the aftershocks t_a of about 4 years, later its effects will be compared with those of a t_a of 1 year which was considered, for instance, by Maccaferri, Eleonora Rivalta, Passarelli, and Jónsson (2013) in modelling the seismic rate changes on the Husavik-Flatey Fault, following the rifting episode with dike emplacement of 1975-1984, near the Krafla volcano.
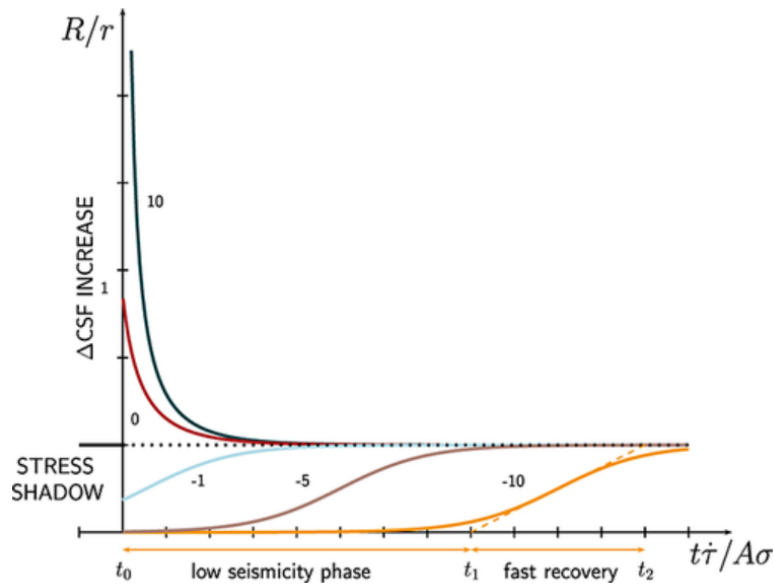
Figure 3.16: Examples of relative seismic rate time evolution for different single ΔCFS steps (black numbers in units of $A\sigma$). (Modified from a figure of Maccaferri, Eleonora Rivalta, Passarelli, and Jónsson (2013)).

In the scenario represented here, a dike with constant shape and velocity, propagates along the positive y direction maintaining constant the x and z coordinates, as it can be visualized in the schematic representation of fig. 3.18 and 3.19. At each step of the shift, the dike elongates and opens as it closes at its back. This corresponds to a series of successive stress steps that results in ΔCFS increases or decreases in each grid point. The effect of a stress step on the relative seismic rate, using the rate-and-state model, is illustrated in fig. 3.16. A positive change in the Coulomb stress in general produces relatively short bursts of seismicity, which intensity increases with the ΔCFS magnitude, and has a time scale of decay of the order of t_a, till the background rate is restored. In contrast negative variations of Coulomb stress leads to periods of suppressed seismicity rates, called *stress shadows*. In this case it takes longer for the seismic rate to recover the stationary value r_0 through the tectonic stressing rate $\dot{\tau}$: the

| positions	P1	P2	P3	P4	P5	P6	P7	P8	P9
x (km)	2.2	2.2	2.2	2.2	2.2	2.2	2.2	2.2	2.2
y (km)	4.0	4.0	4.0	12.0	12.0	12.0	20.0	20.0	20.0
z (km)	-0.6	-4.2	-8.2	-0.6	-4.2	-8.2	-0.6	-4.2	-8.2

Table 3.1: Coordinates of the evaluation points.

time scale is of the order of $\frac{-\Delta CFS}{\dot{\tau}}$ (see Maccaferri, Eleonora Rivalta, Passarelli, and Jónsson (2013)).

In the following paragraphs I am going to present the results concerning the seismicity rates' evolution with time, from different points of view: firstly I consider some punctual outcomes, then the seismic behaviour integrated on columns and rows of the volume of the spatial grid.

Results: relative seismic rates vs time in different grid points

To study the phenomenon of induced seismicity modeled in this scenario, I begin by considering the effect of the moving dike on nine single points distributed in space as in figures 3.18 and 3.19. Since the dike geometry is symmetric about the y-axis, the evaluation positions are taken only on one side (right from the point of view of fig. 3.18) of the dike. Furthermore they are located at depths above, at the center and under the dike, relatively to the positions occupied by the dike at the start, halfway and finish of its propagation.
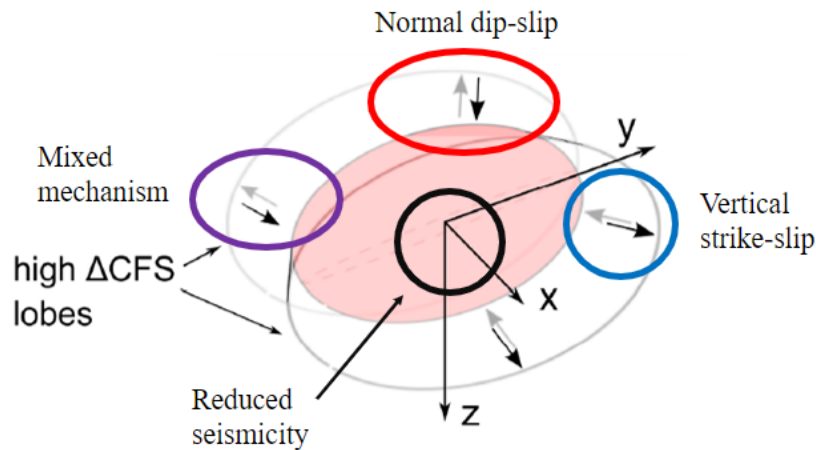

Figure 3.17: Modified from Passarelli et al. (2015), elliptical dike and favoured fault geometries.

The simulations have been done for both the couple of dip-slip normal faults and that of strike-slip ones. This because they have been observed for the Miyakejima event both focal mechanisms (Passarelli et al. (2015)) but also because from a theoretical point of view, for stress fields such those generated by a dike, lobes of high ΔCFS on which these types of faults (and mixed ones) form, are expected (see fig. 3.17 and Passarelli et al. (2015)).
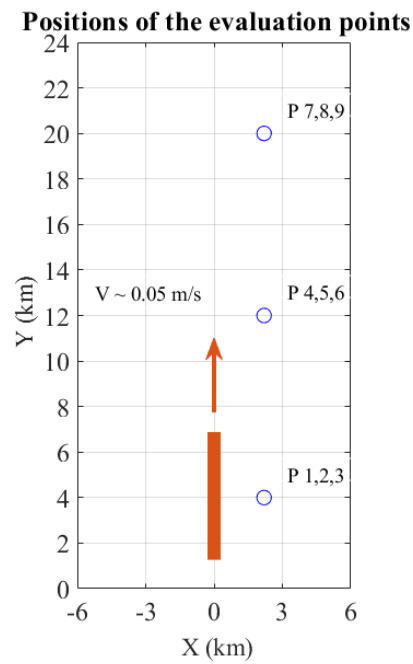
Figure 3.18: Schematic map view of the dike motion in the xy-plane and of the positions of the nine evaluation points of the induced seismicity.
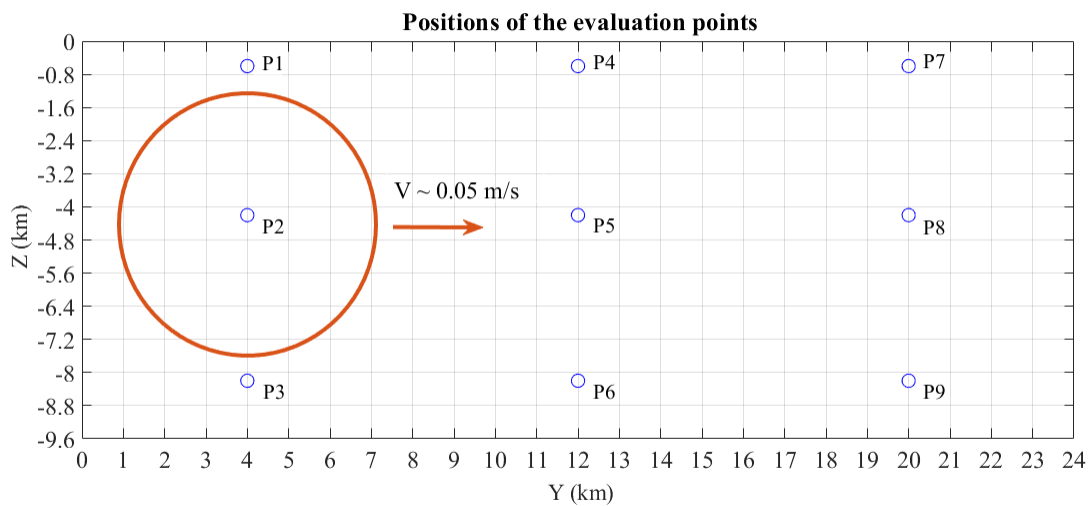

Figure 3.19: Schematic lateral view of the dike motion in the yz-plane and of the positions of the nine evaluation points of the induced seismicity.

In the following figures I represent the logarithm of the relative seismic rates at some of the nine evaluation points (the others are contained in appendix B)), as a function of time. A comparison is made between the dip-slip faults and the strike-slip ones. Since the time steps are compressed on the horizontal axis of the figures because of their large number, and they are sufficiently small (with respect to t_a), the diagrams appear quite smoothed. It has to be precised that the ΔCFS generated by the source opening at different stages, are included between the temporal steps 1 and 40, corresponding to the dike moving. Furthermore, here the decaying time t_a is set to 4 years.

In figures 3.21 and 3.22 are reported the evolution of the rates for P1, P4, P7, which are the positions at minor depth (-0.6 km) and those of P2, P5, P8, which are near the dike center depth (-4.2 km). Referring to fig. 3.17, the former group of points will be more sensitive to stress changes for the dip-slip faults because they are the favourable geometries for these positions relative to the dike. Conversely, the latter group of positions will be more affected when considering the configuration of strike-slip faults, for analogous reasons. Indeed this is what is observed in the simulations.

In the first step of each diagram, the rate change is due to the sudden appearance of a source of stress in an unperturbed state, and positive or negative values depends on the position with respect to the intrusion. For the upper points the Coulomb stress increases because they are near an area of increased shear stresses. Conversely, faults near the middle of the dikes, experience more compression that decreases the Coulomb stress. The rest of the time steps follow essentially the evolution of CFS: rates increase and decrease accordingly to a combination of the effects of Coulomb stress changes and aftershock decaying or background rate restoring from a stress shadow (which depend on t_a). This can be seen by comparing the temporal evolution of ΔCFS with that of the seismic rate. Indeed placing side by side fig. 3.20 with figures 3.21 and 3.22, for the positions P1 e P5, it is possible to note how the rate variation with time is modulated by the ΔCFS evolution. Moreover the peaks in the evolution of the rates can be interpreted as the passages of the "high ΔCFS lobes" of fig. 3.17, on the points of evaluation, while the dike is propagating. The diagrams of the lower points P3, P6, P9 (depth of -8.2 km), are similar to those of the upper points, mainly because they are at similar distances from the dike center. For this reason they have been placed in appendix B. The principal difference is that their values are smaller because the simulation is carried out in an half-space, this means that nearer the free surface strains and normal stresses are less negative and thus the corresponding Coulomb stresses are higher.

Next, I examine how the seismicity rates are influenced by the decaying time of the aftershocks. In fig. 3.23 are reported the evolution of rates at the medium depth points P2, P5, P8 for two values of t_a: 1 and 4 years. The main effects on the curves that can be noticed are the amplification of the peaks and valleys and the greater velocity of the rate decays. Thus to a minor t_a correspond more intense and shorter bursts of seismicity, peaks that are achieved earlier in time and, if they are present, stress shadows deeper and longer.
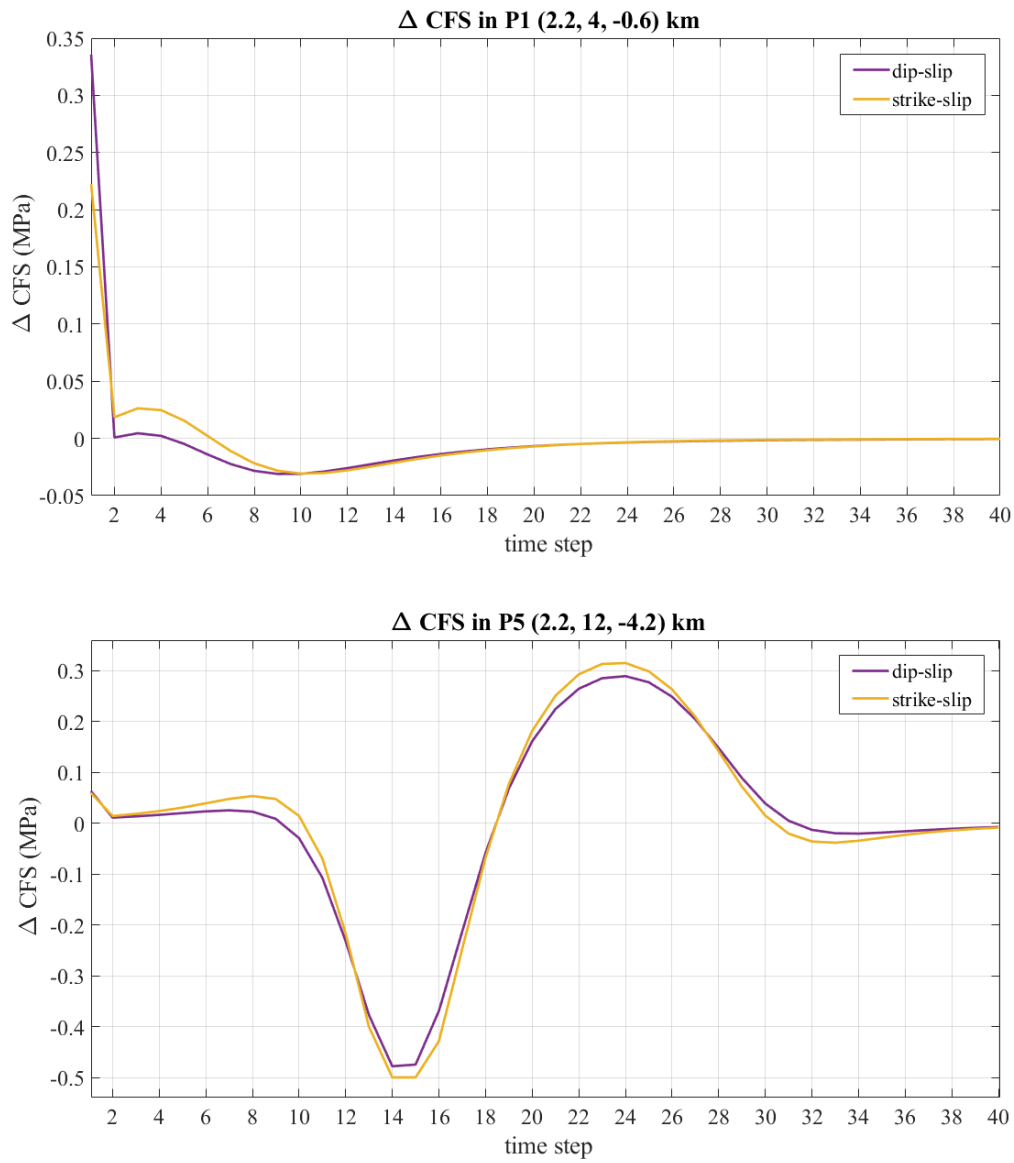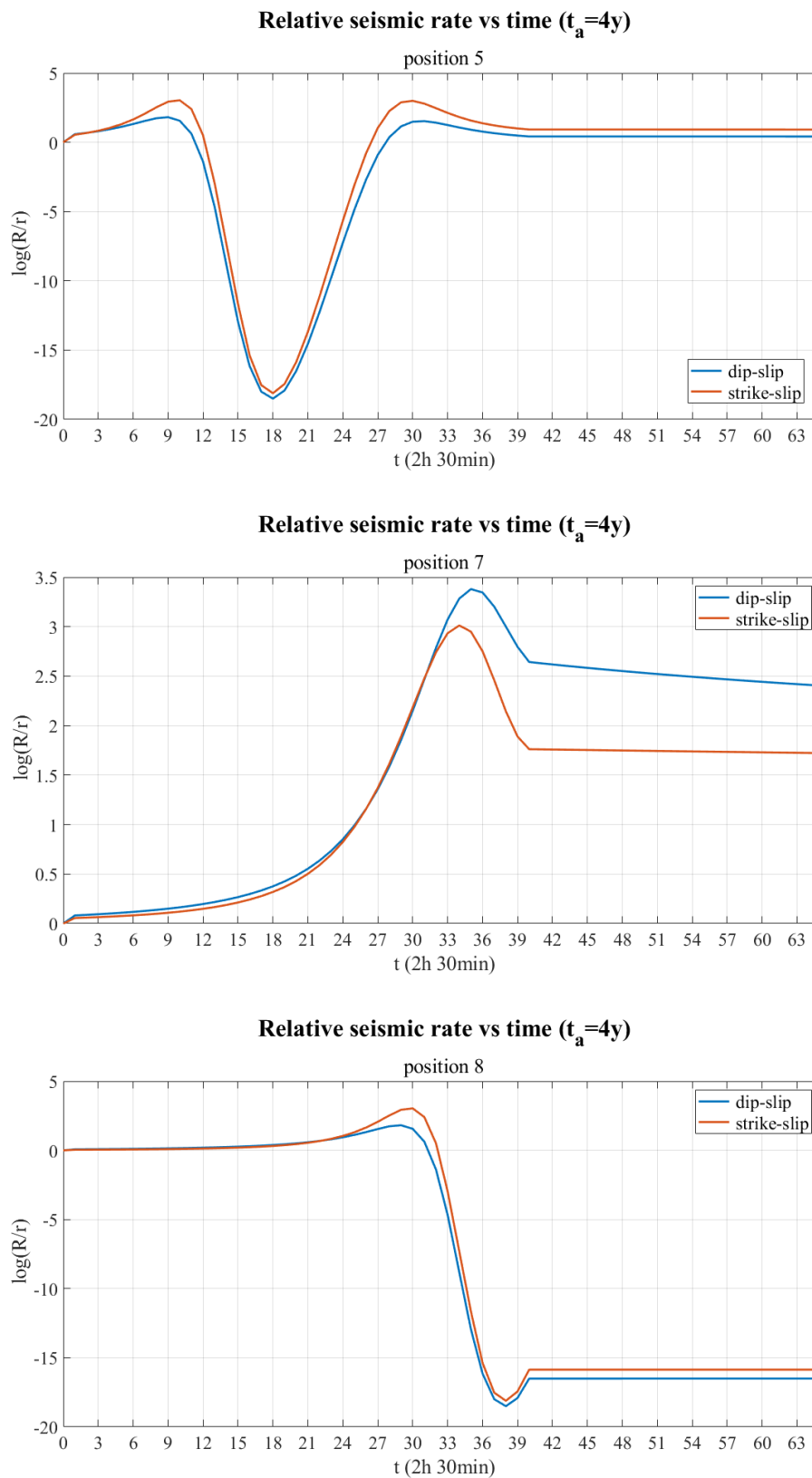
Figure 3.20: Subsequent Coulomb stress changes versus time steps, in positions P1 and P5, for dip-slip and strike-slip faults.
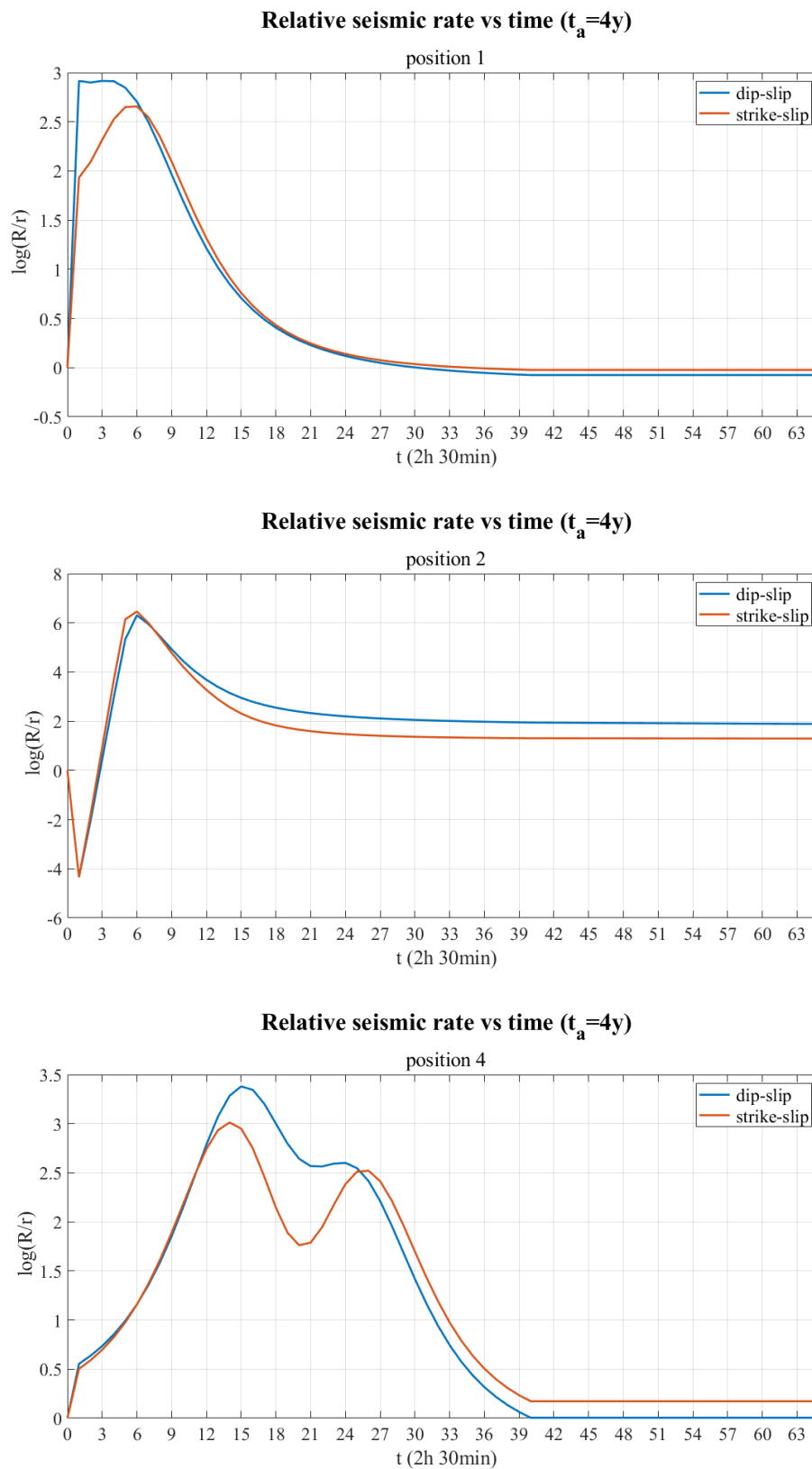
Figure 3.21: Decimal logarithm of relative seismic rates versus time, for positions P1, P2 and P4, for both dip-slip and strike-slip faults.
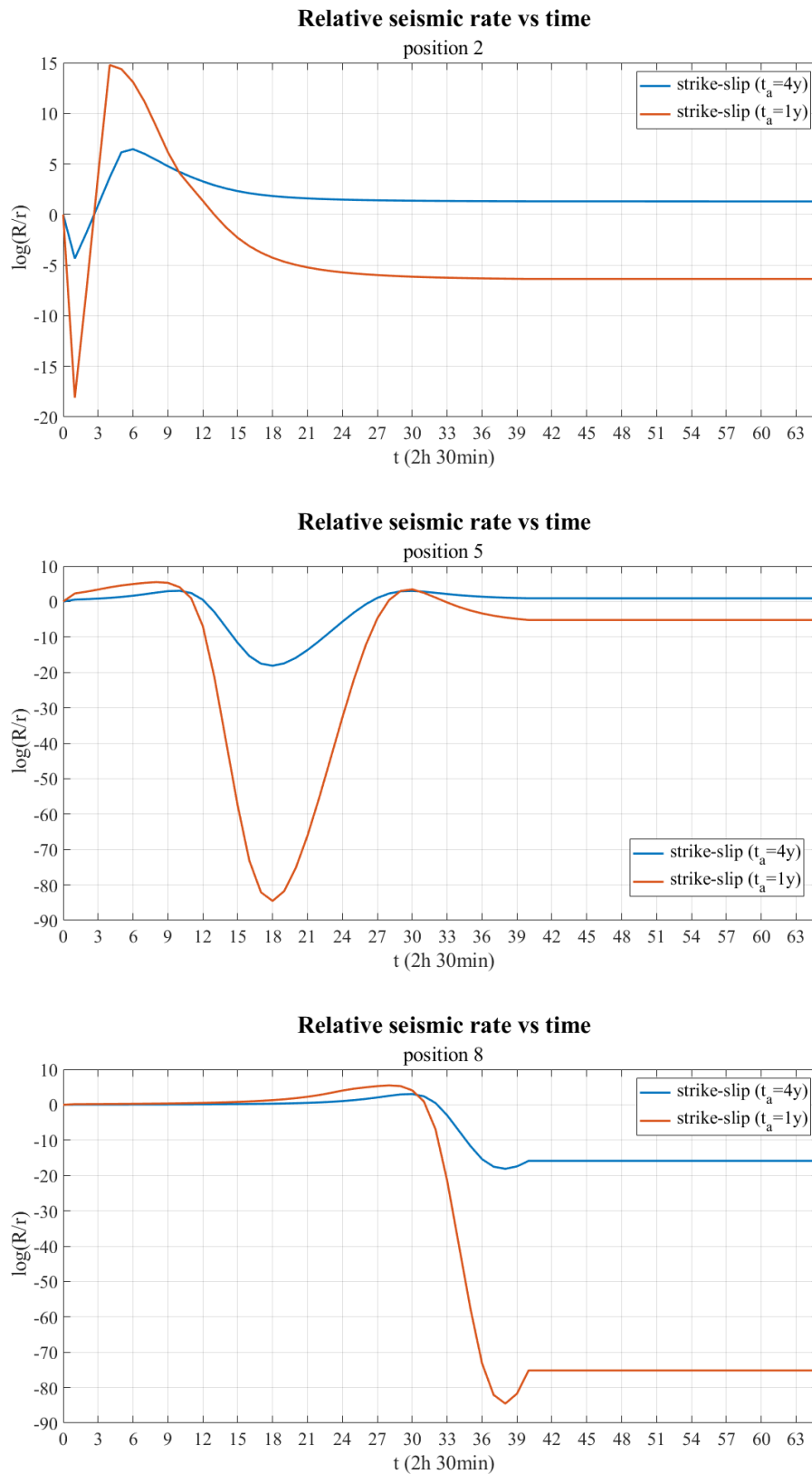
Figure 3.22: Decimal logarithm of relative seismic rates versus time, for positions P5, P7 and P8, for both dip-slip and strike-slip faults.

Figure 3.23: Decimal logarithm of relative seismic rates versus time, at positions P2, P5 and P8, for strike-slip faults and two different t_a of 4 and 1 years respectively.

Results: relative seismic rates integrated on columns or rows of the volume of calculus

In this paragraph, I present my results from the perspective of how seismicity is usually depicted in diagrams. I calculate and plot seismicity rates by summing them on columns along the z-direction, or on rows along the x- or y-direction. This allows to visualize the spatial distributions of rates relative to column or row volumes, at different time steps. In order to have reasonable results, not depending on the number of grid points for one column or row, the relative rate of a grid point is weighted with the elemental volume: in my case it is $6.4 \cdot 10^{-2}$ km^3. Successively, considering r_0 a rate of background per unit volume, the resulting rates are normalized with respect to the total rate r of a column or row relative to before the dike emplacement. Thus in expression $\frac{R}{r}$, R is the absolute rate and r is the background rate, both relative to a column or row.

In the following images I illustrate some frames of the spatial evolution of seismicity rates at different instants, that is the first event of dike emplacement at time 2.5 hours from the start of the simulation and other five representative moments. The second to the fifth frames are relative to the early propagation stages (times at 10 h, 15 h, 22.5 h and 1 d 23.5 h from the beginning), while the last one is at 2 days and 2 hours after the dike stops. An exception is the case of lateral section figures (3.29, 3.30 and 3.31), which instead of instant 15 h, are considered instants 5 h and 7.5 h. Figures 3.24, 3.25, 3.26 and 3.27 represent the mentioned frames in map view, the former two figures are relative to dip-slip receiver faults and the latter two to strike-slip ones. In map view the rate of each pixel, refers to that of a column in a range of depths from -0.2 km to -9.0 km. In figure 3.28, I report the distributions of rates in frontal vertical sections and in figures 3.29, 3.30 and 3.31 in lateral vertical sections.

In frontal sections rates are relative to rows in the y-direction while in lateral sections they refer to rows along the x-direction. Since the results of the frontal and lateral sections for the strike-slip faults are similar to those of the dip-slip ones, their plots are not reported here. The plots in frontal section, since they are a little more different than those in lateral section, can be found in appendix B. Moreover in the following figures, the range of the colorbar is everywhere the same from a minimum of 10^{-4} to a maximum of 10^7, the latter is somewhere exceeded, especially near the borders of the dislocations.

Examining the distributions of rates in map view, the zones of low seismicity in blue are well distinguishable from those of pre-event values (of the order of 10^0), in light blue, and those of enhanced seismicity in orange. It is worth to notice that near and on the line of the rectangular dislocations, in particular in the frame at time 2.5 h, some discontinuities are evident: they are due to the finite dimensions of the patches used for the discretization of the dike, that produces border effects. To reduce this effect, smaller patches can be exploited, but these imply a larger number of them for the same dike size and more computational cost, or the grid points may be set more distant from the source. In this simulation the closest grid points are at a distance of a patch length.

As expected theoretically (confer with fig. 3.17), low seismic rates are observable on the pro-

jection of the dike on the xy-plane and medium ones along the diagonals that move from the corners of the mentioned projection. These regions is where the shear stresses are higher and so are the Coulomb stresses for strike-slip, dip-slip and mixed faults. In contrast the zones laterally to the dike, experience high values of compressive normal stresses which suppress seismicity. These characteristics are present in all the frames of figures 3.24, 3.25, 3.26 and 3.27. The essential difference among them, is that in the former two groups of figures, which consider normal faulting, high seismicity rates are more concentrated above the dike and less on the diagonals from the corners of the xy-plane dike projection. Instead in the last two groups, relative to strike-slip receiver faults, there are higher rates along the diagonals, ahead and behind the intrusion. The interpretation here presented is also supported by looking at frontal and lateral sections. In frontal view (fig. 3.28) the high rates are at the center of the xz-plane projection and at the diagonals from its corners. In lateral view (figures 3.29, 3.30 and 3.31) a circular crown in yellowcan be seen, with at its center a blue circle seismicity in stress shadow.

Observing the dike moving forward, it can be noticed that the shape of the rate distribution does not change in the front and ahead of the dike, this is because the front of the dike acts on similar conditions of pre-loaded faults of the background seismicity. It is a different situation that behind and at the center of the dike, in which seismicity continues to change. The rate-and-state formula is sensitive to the history of the rate, i.e. its time series: it means that the same ΔCFS step generates different outputs for different states of the rate at the moment it is applied. So when the dike closes at its tail to open in another location, the rate between the closing and the new opening is not restored to the pre-event conditions but to a different value (see formulas 2.22 and 2.21). Thus when the dike reopens in its forward movement, partially contrast the stress shadow of the previous step, this can be seen in lateral section figures.

From the inspection of figures in map and frontal view, it can be seen how after the dike completely passes its initial position, the pattern of seismicity stabilizes. In contrast, laterally to the dike's initial position two lobes of enhanced seismicity tend to form. In these areas the receiver faults experience an increase in Coulomb stress during dike propagation. Nevertheless, a low seismicity tail/trace is created behind the dike where the Coulomb stresses increase a lot less. This behaviour can be seen also in figures 3.21 and 3.22, in central positions P2 and P5: P1 experiences an increase in seismicity that ends with a greater rate with respect to that of P5. The position P5 sees a minor increase, followed by a decrease and a successive new increase. This latter type of time evolution is more typical of points ahead of the dike. Therefore the lobes are probably linked to when the dike starts to move from its initial position. Although P1 and P5 at some point in the simulation experience the same trend of increasing rate, the former starts it at a value around 10^{-4}, the second at around 10^{-17}.

Therefore, this behaviour is probably linked to the stress history of the specific position on the grid. The effect of the two lobes probably can be attenuated by introducing an initially smaller dike that successively inflates gradually until it reaches the size of that used in this simulation.
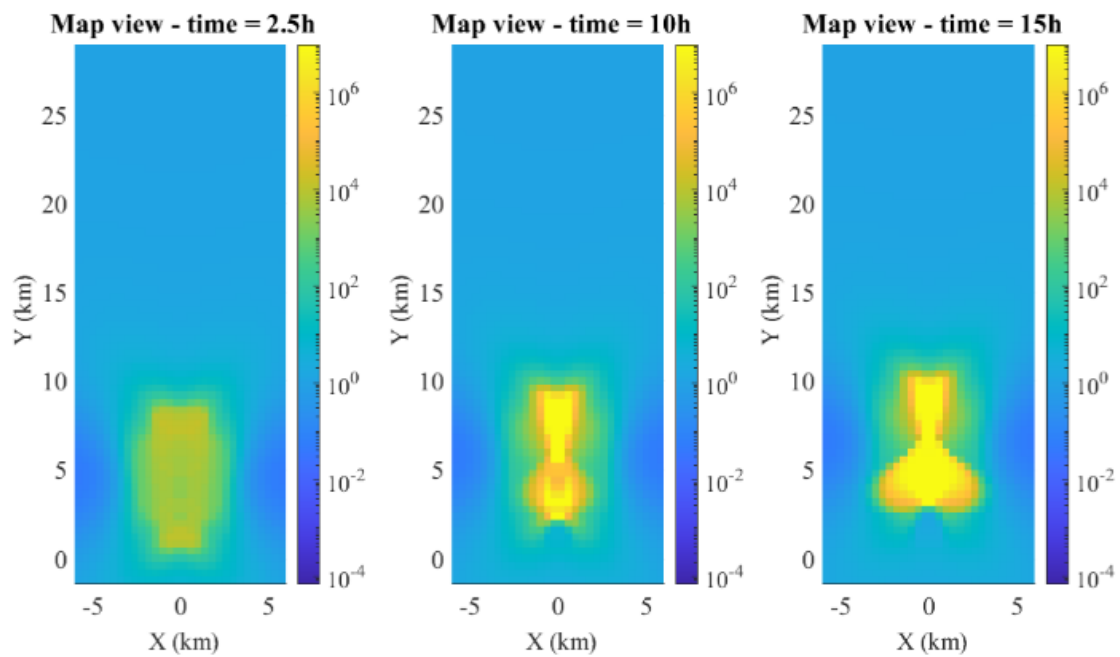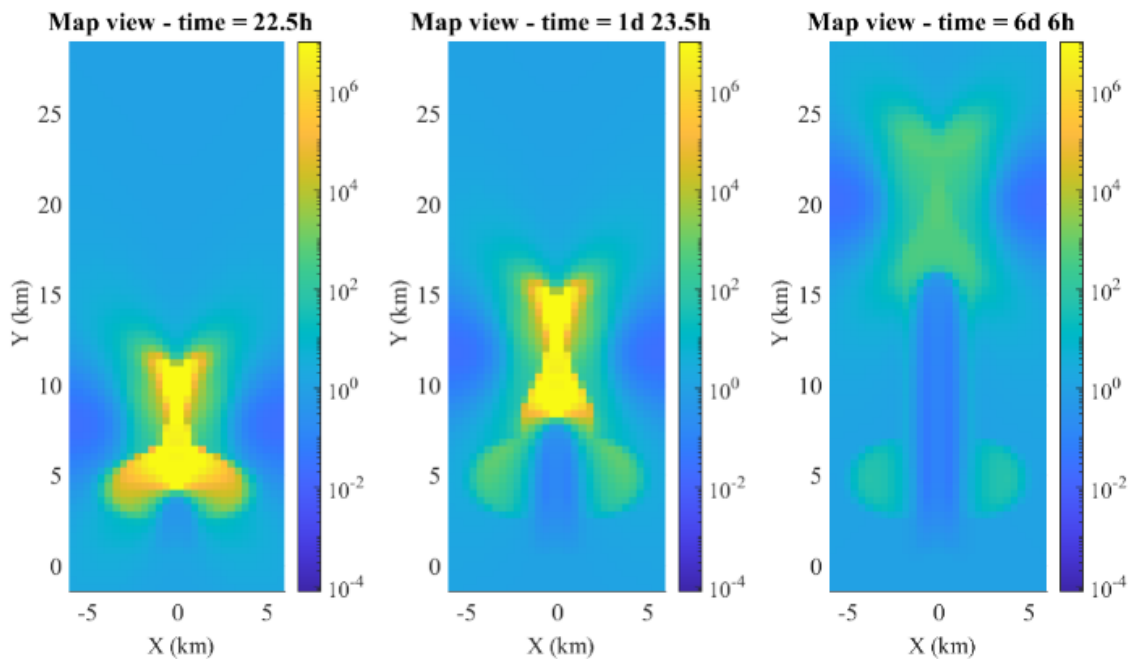
Figure 3.24: Map view of the spatial distribution of seismic rates, for dip-slip faults, at 2.5 h, 10 h and 15 h.
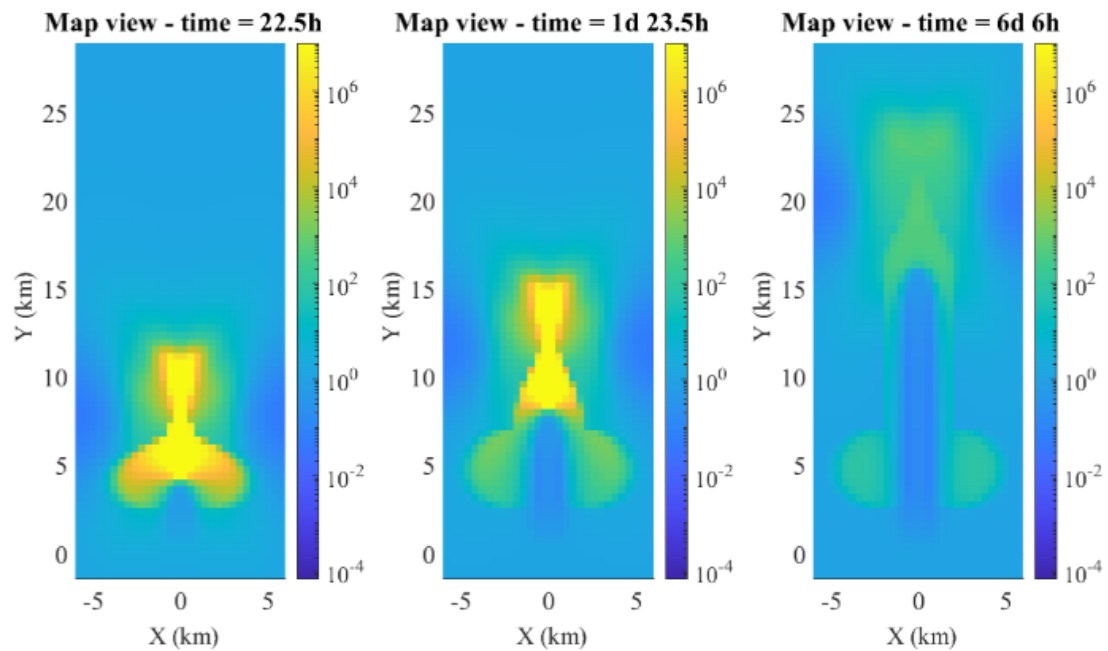
Figure 3.25: Map view of the spatial distribution of seismic rates, for dip-slip faults, at 22.5 h, 1 d 23.5 h and 6 d 6 h.
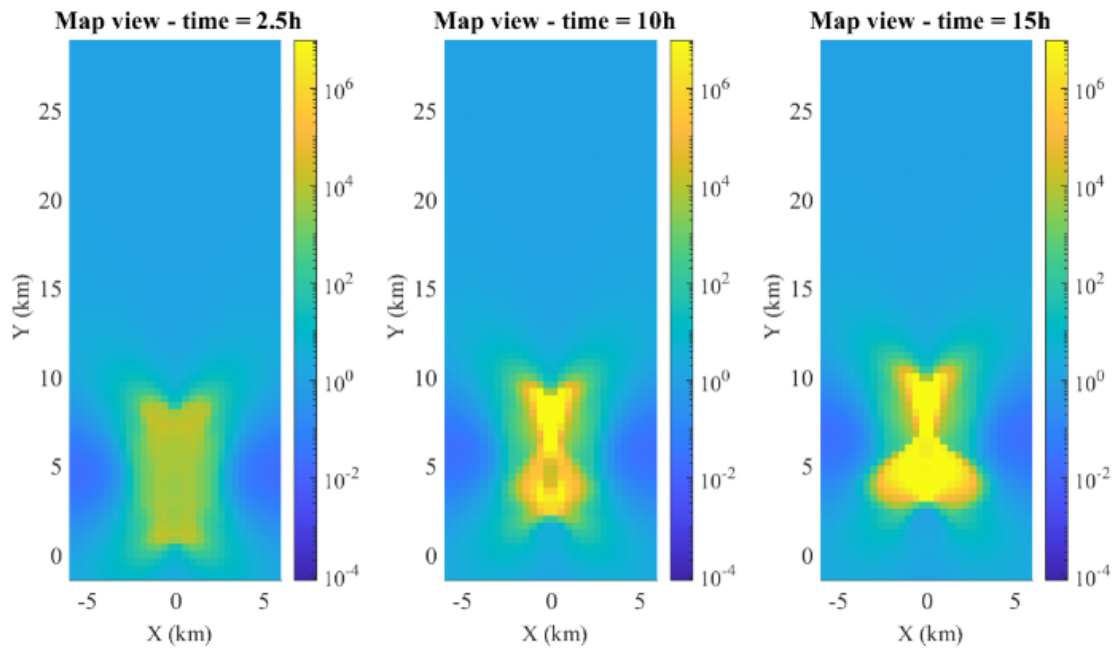
Figure 3.26: Map view of the spatial distribution of seismic rates, for strike-slip faults, at 2.5 h, 10 h and 15 h.
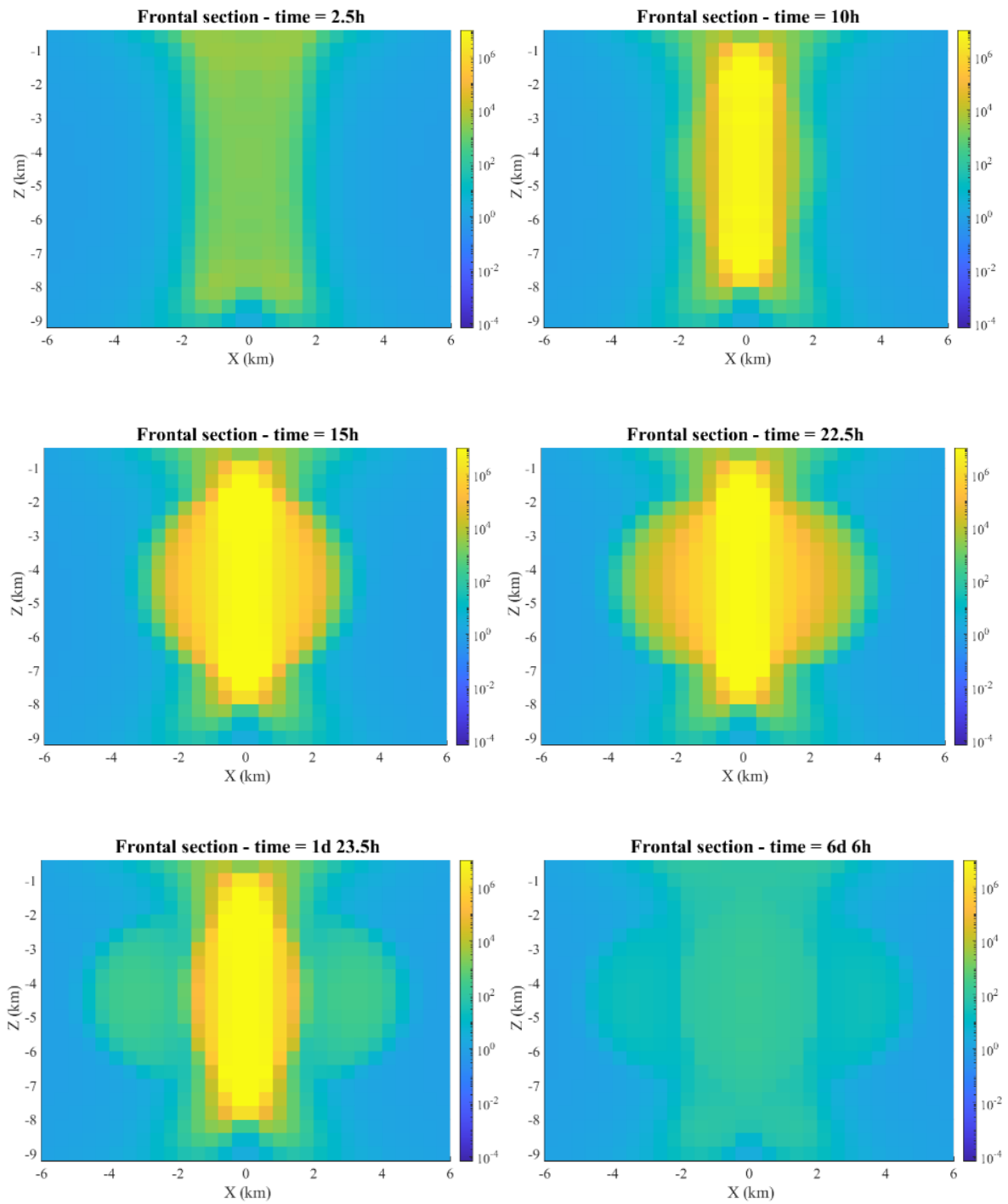

Figure 3.27: Map view of the spatial distribution of seismic rates, for strike-slip faults, at 22.5 h, 1 d 23.5 h and 6 d 6 h.

Figure 3.28: Frontal section view of the spatial distribution of seismic rates, for dip-slip faults, at 2.5 h, 10 h, 15 h, 22.5 h, 1 d 23.5 h and 6 d 6 h.

Figure 3.29: Lateral section view of the spatial distribution of seismic rates, for dip-slip faults, at 2.5 h, 5 h and 7.5 h.
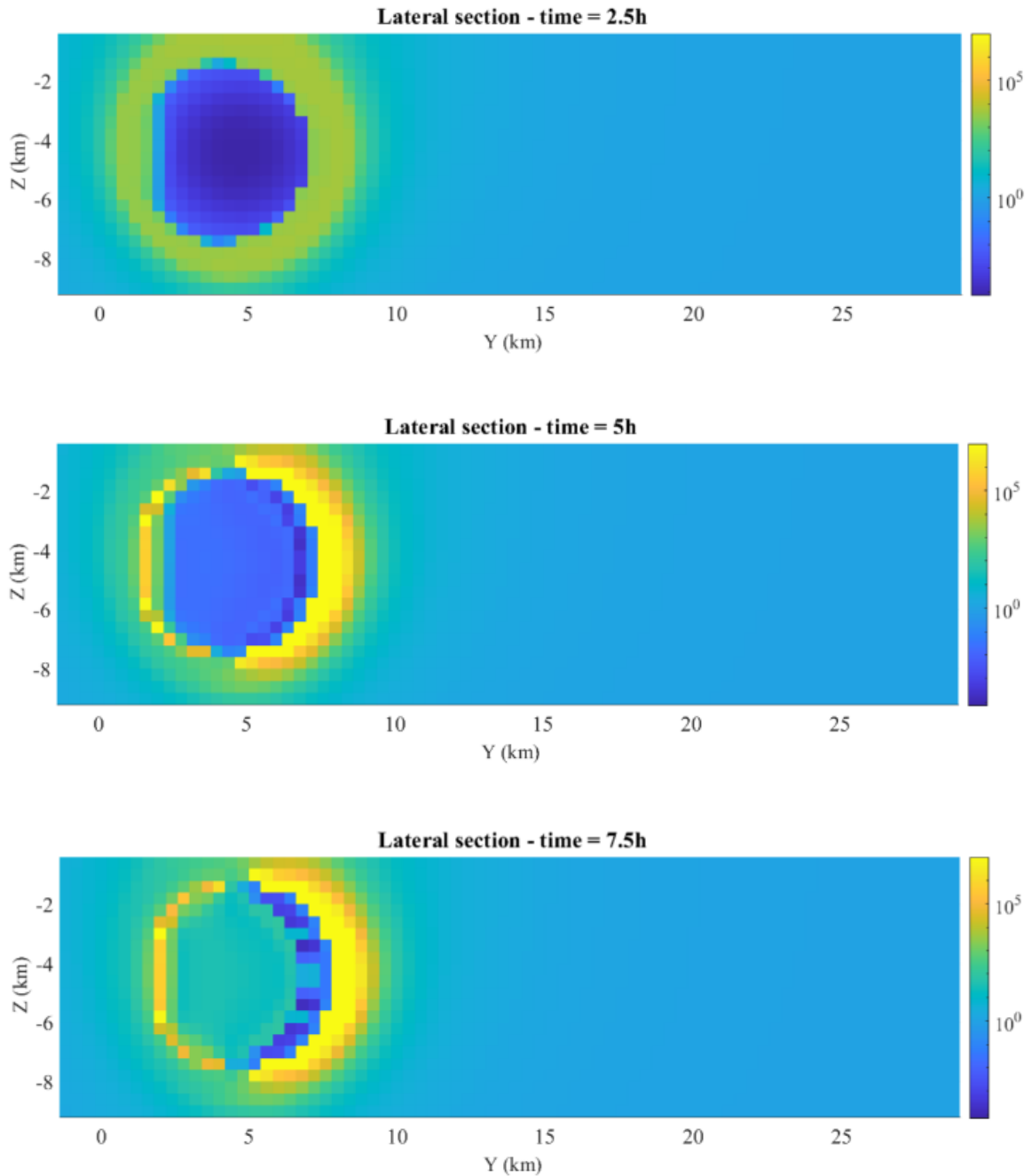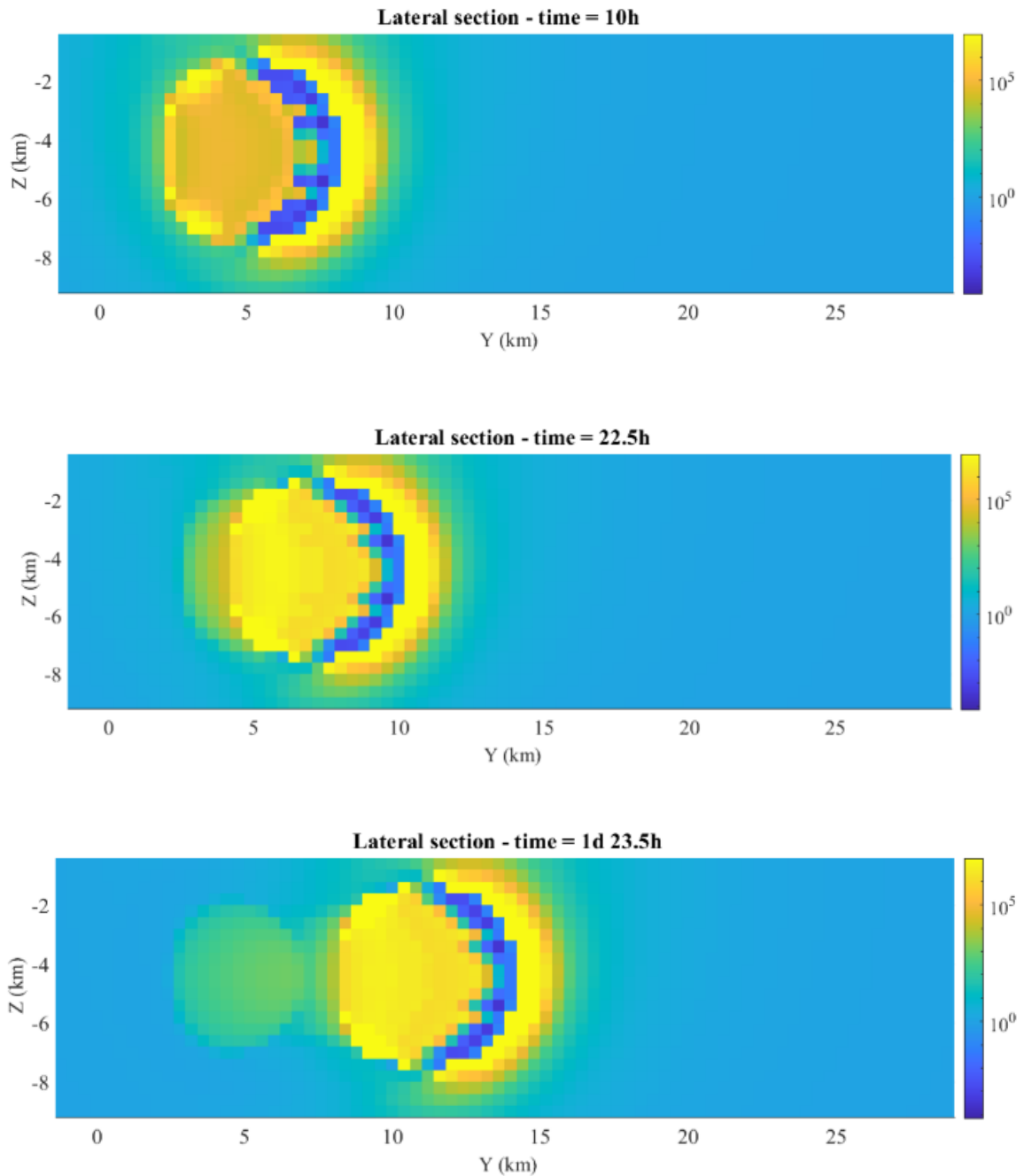
Figure 3.30: Lateral section view of the spatial distribution of seismic rates, for dip-slip faults, at 10 h, 22.5 h and 1 d 23.5 h.
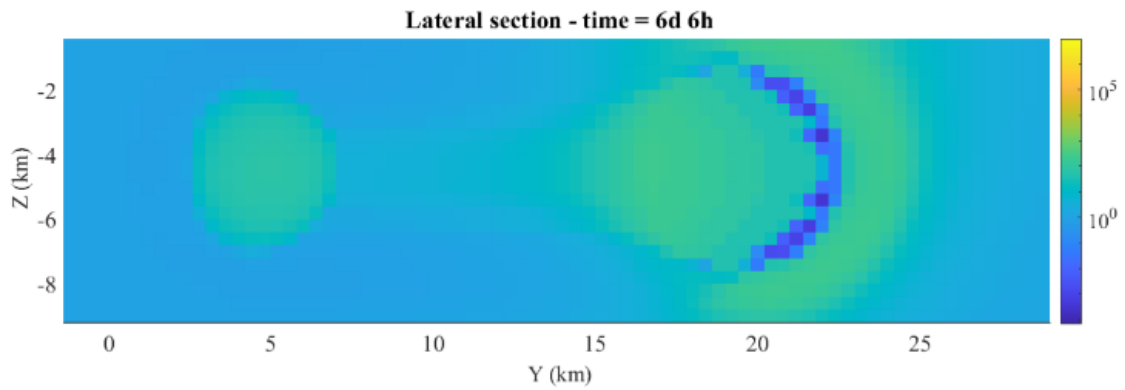
Figure 3.31: Lateral section view of the spatial distribution of seismic rates, for dip-slip faults, at 6 d 6 h.
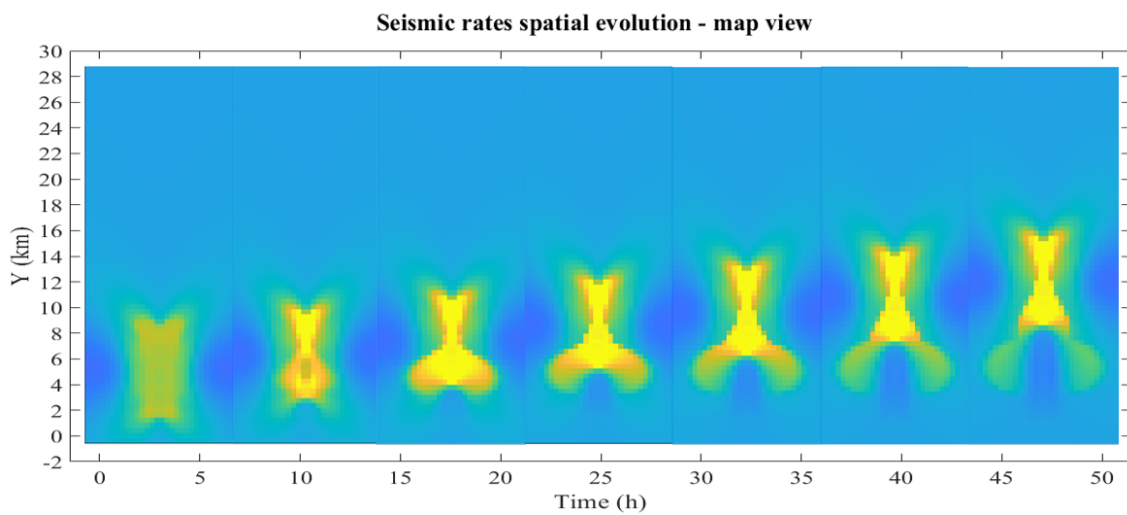
Figure 3.32: Temporal evolution of the seismicity rate distribution in map view. The dike is propagating along the y-direction at constant velocity, thus the motion of its center versus time is described by a straight line. To note the changing with time of the pattern of the spatial distribution.

The evolution of seismicity in map view, at a constant velocity, can be well visualized also in figure 3.32 in which the rates for strike-slip faults are represented for the first seven steps at intervals of 7.5 h. The values of the rates can be interpreted considering the Gutenberg-Richter law (Gutenberg and Richter (1950)) on the frequency of earthquakes in a determined region.

$$N(M) = 10^{a-bM} \tag{3.5}$$

Equation 3.5 gives the number of earthquake N in a certain region and for a given interval of time T, with magnitude equal or greater of M. The parameter a and b characterize the GR curve for the area, with the so called b-value that takes values around 1. The GR law implies that for every earthquake of a certain magnitude M typically there will be ten earthquakes of magnitude $M-1$, one hundred of magnitude $M-2$ and so on. Thus for example a value of the order of 10^3 of the relative seismic rate $\frac{R}{r}$ of the simulation, given the background rate r referred to a magnitude of completeness M_c of 3, equal to 1, can be interpreted as involving 10^3 earthquakes of magnitude 3, 10^2 of magnitude 4, 10^1 of magnitude 5 and 10^0 of magnitude 6.

Results: simulation with larger steps Δs and Δt for the dike translation

A simulation with a coarser representation of the dike movement has been tested to examine the effect of larger spatial and temporal increments Δs and Δt, maintaining the same velocity, on seismic rates: Δs is set to 4 km and Δt to 6 h. In particular, the time domain is divided in 30 steps by Δt, while the dike changes in position along the positive verse of the y-axis, of the quantity Δs, happens at the following times from the start: 6 h (for the emplacement event), 1 d 6 h, 2 d 6 h, 3 d 6 h, 4 d 6 h and 5 d 6 h. The results in map view for dip-slip faults can be seen in figures 3.33 and 3.34. Results in frontal and lateral views are found in figures 3.35, 3.36 and 3.37.

The dike in this case takes longer steps in space and time. The effect on rates is that of a less gradual and thus more abrupt change in stress. As it can be seen in the map view figures, the formation of localized tails of high seismicity alternated to low seismicity zones, after every new movement of the dike. In this way the spatial pattern of seismicity appears more fragmented making the modelling of the dike propagation, for most real cases, less representative. I conclude that a finer discretization in space and time is necessary in order to have usable results.

Figure 3.33: Map view of the spatial distribution of seismic rates, for dip-slip faults and a large spatial step of translation of the dike, at 6 h, 1 d and 1 d 6 h.
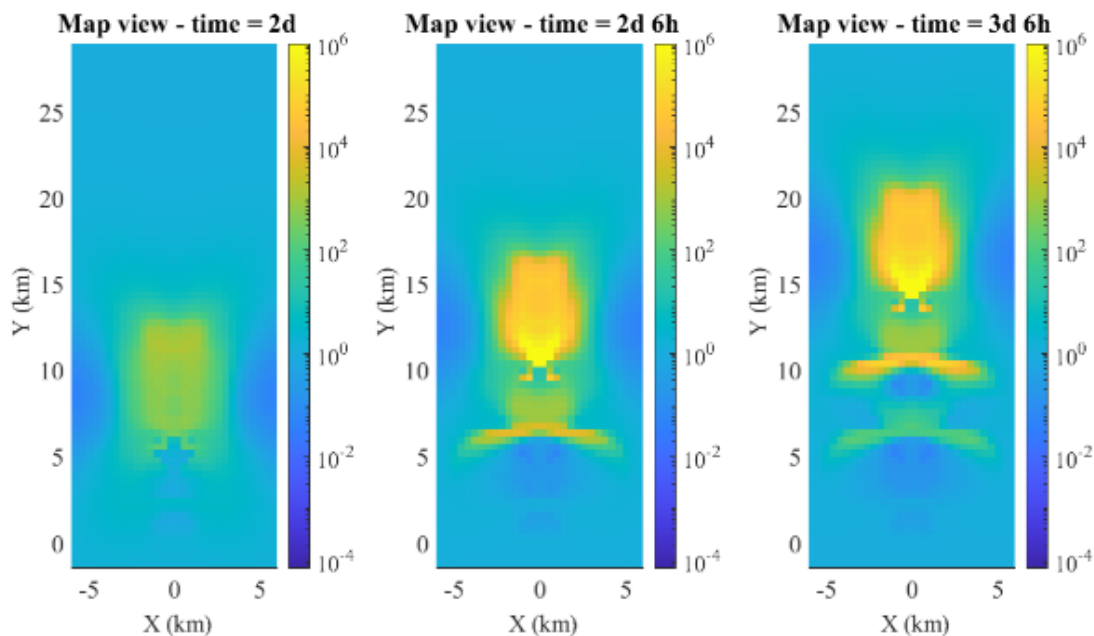
Figure 3.34: Map view of the spatial distribution of seismic rates, for dip-slip faults and a large spatial step of translation of the dike, at 2 d, 2 d 6 h and 3 d 6 h.
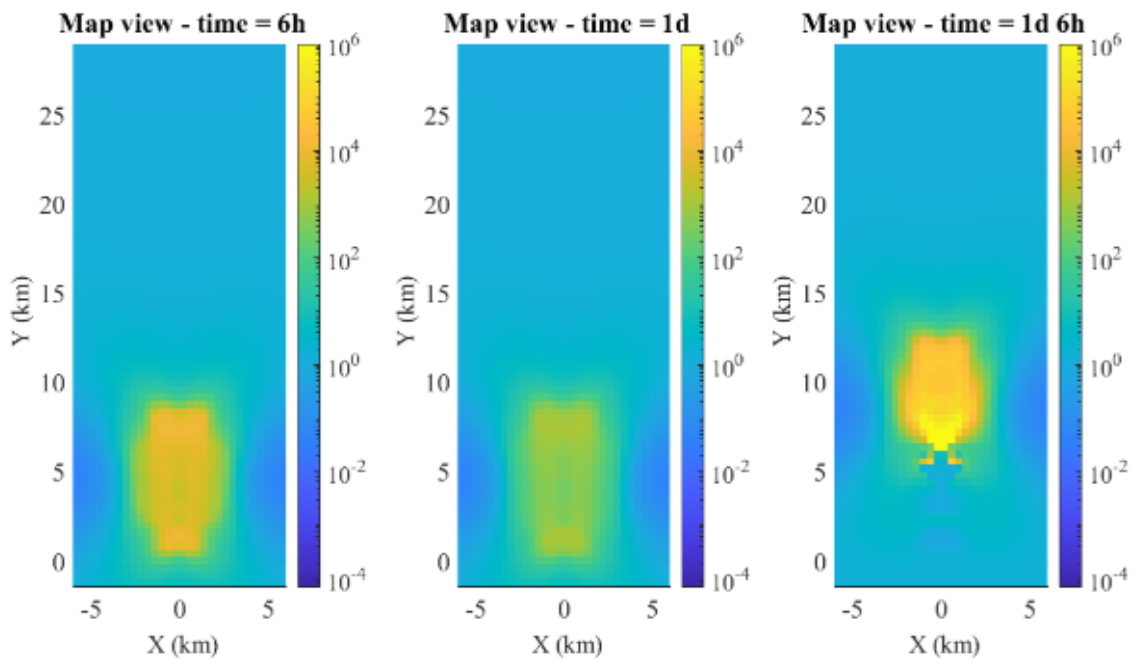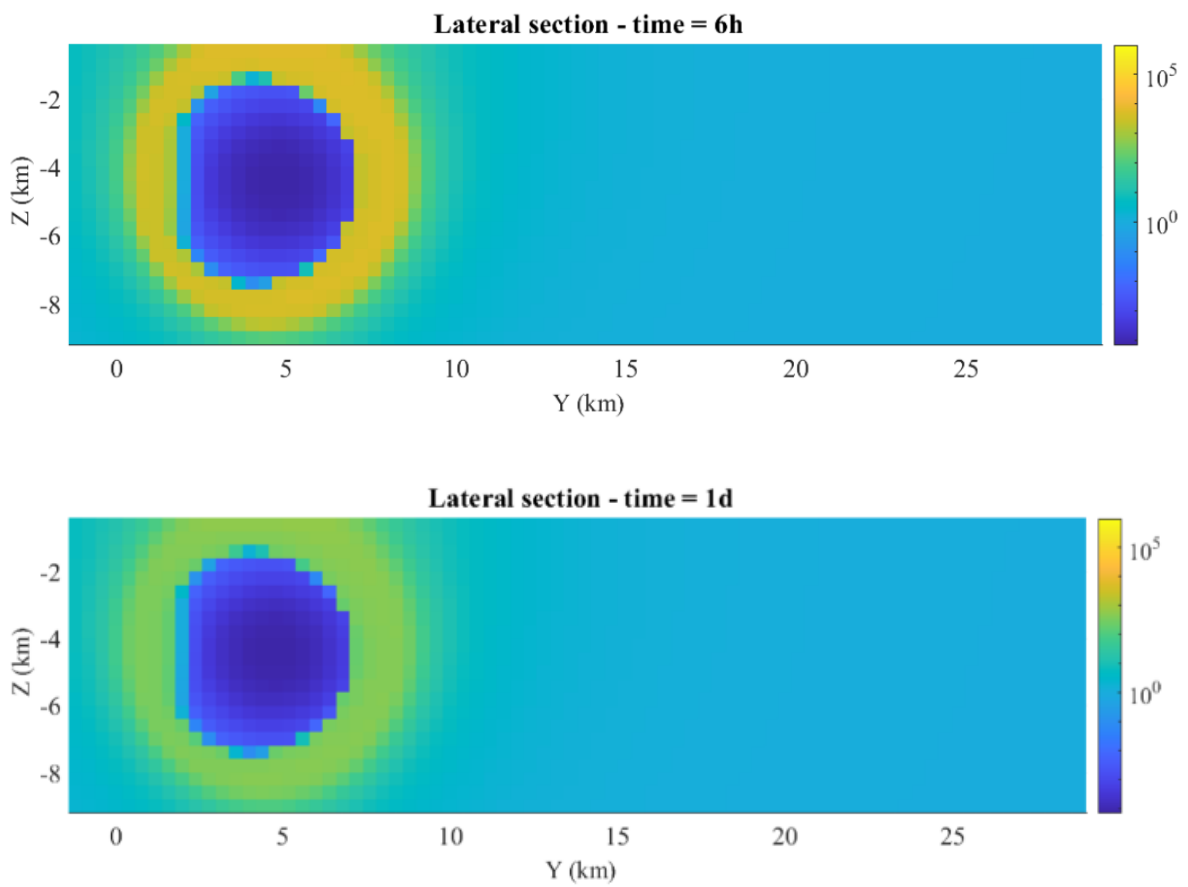
Figure 3.35: Lateral section view of the spatial distribution of seismic rates, for dip-slip faults and a large spatial step of translation of the dike, at 6 h and 1 d.

Figure 3.36: Lateral section view of the spatial distribution of seismic rates, for dip-slip faults and a large spatial step of translation of the dike, at 1 d 6 h, 2 d and 2 d 6 h.

Figure 3.37: Frontal section view of the spatial distribution of seismic rates, for dip-slip faults and a large spatial step of translation of the dike, at 0 h, 6 h, 1 d, 1 d 6 h, 2 d and 2 d 6 h.

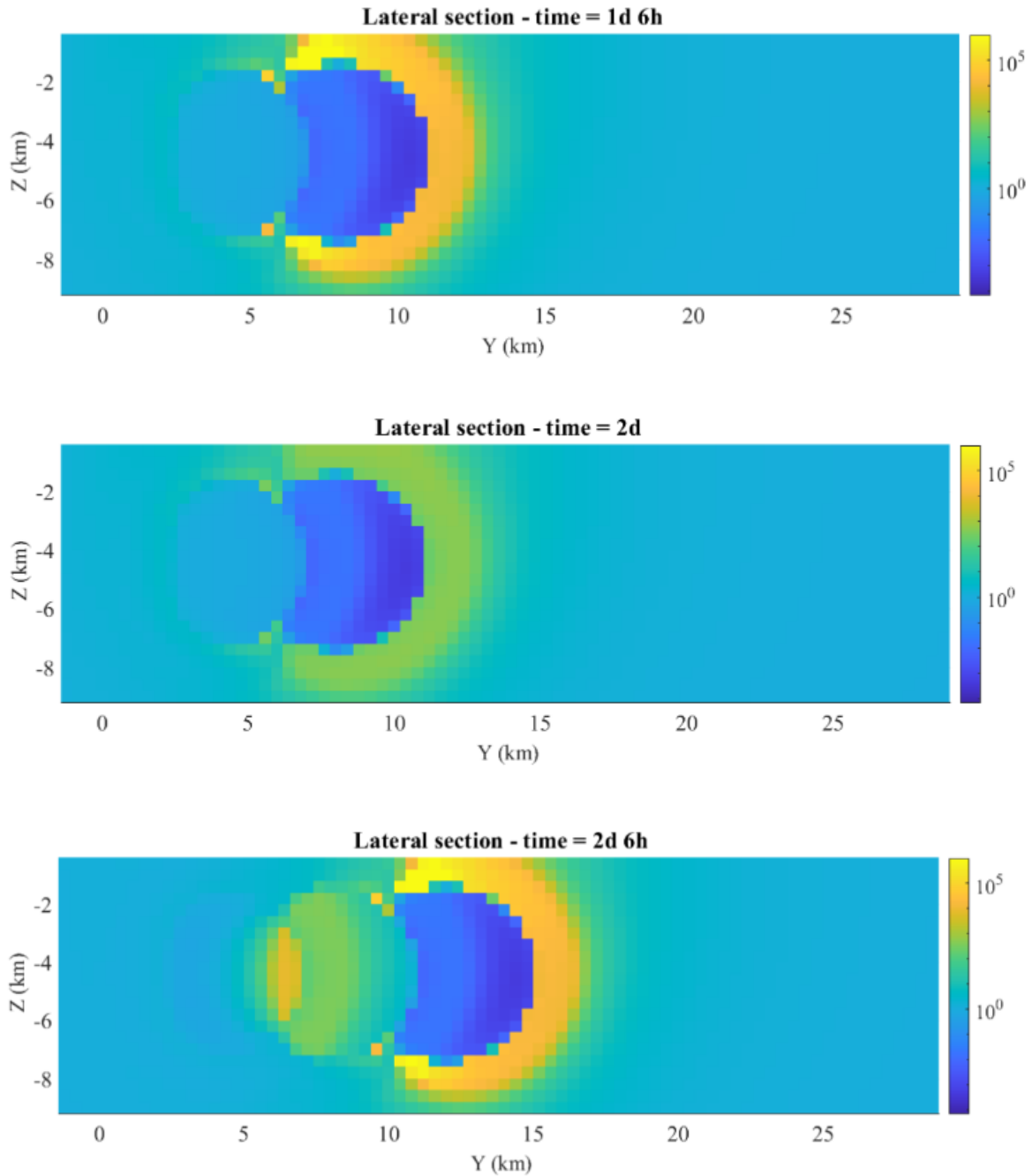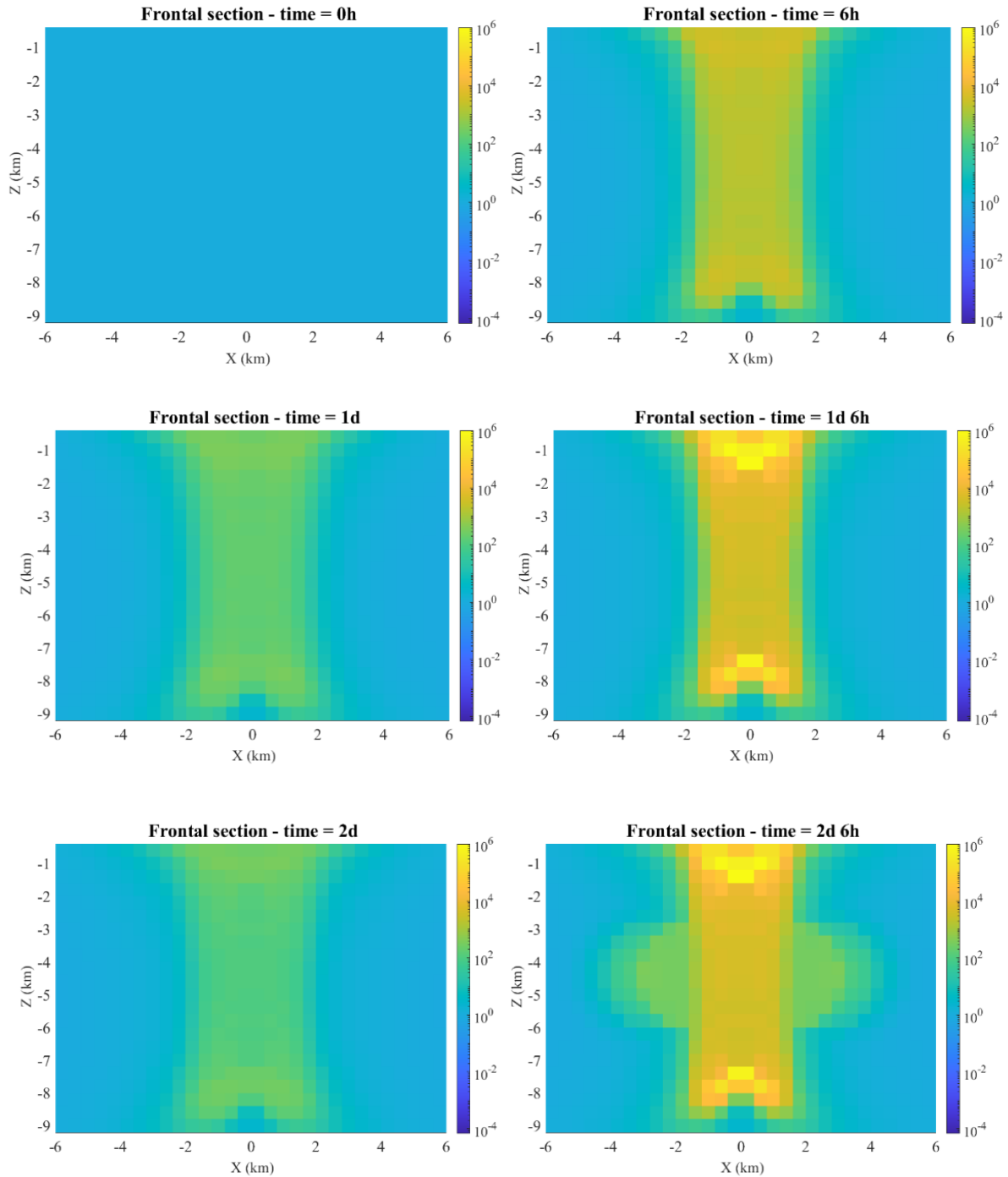## 3.3 Scenario 2: variable shape and velocity

In this second scenario, the propagating dike has the same teardrop-shaped geometry but with different conditions on the size and velocity of the intrusion. Since the dike episode at Miyakejima involved a topography at the surface, in this scenario the intrusion changes size and velocity (see fig. 3.38). Indeed when the dike passes under a variable topography it experience a variable horizontal overpressure gradient $\Delta\gamma$. Recalling equation 3.3, the velocity depends on the volume, here set to be approximately constant, and the overpressure gradient.
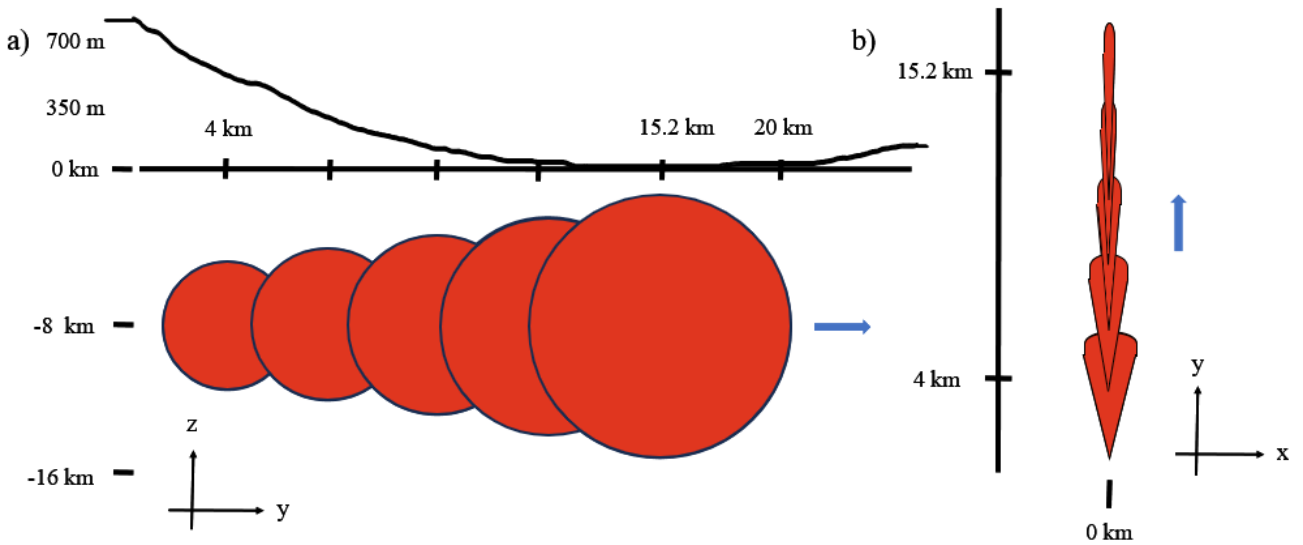
Figure 3.38: Schematic illustration, in cross section (a) and map view (b), of the evolution of the propagating dike described in scenario 2. In this case in figure (a) there is a draw of a topography distribution along the dike path, obtained as a simplified version of that of the 2000 Miyakejima volcano event, as it will be described later.

3.3.1 Spatio-temporal calculation grid and dike representation

The spatial calculation grid is defined as in the previous simulations. The extensions of the volume of calculus in the three orthogonal directions are: a x-range from -7.4 km to 7.4 km, a y-range from -1.2 km to 25 km and a z-range from -16.8 km to 0 km. The time array is composed of 785 temporal steps Δt of 10 min each. For the spatial increment of the dike position I choose to set the step Δs to 0.8 km; since the velocity changes (dike decelerates), at different moments of the simulation, the spatial steps are covered in different time intervals.

The dike is still modelled as a circular BEM crack after Davis, Eleonora Rivalta, and Dahm (2020), except that I vary the diameter of the circle and the distributed opening, with the constraint that the volume remains the same. In table 3.2 I report the emplacement event and the successive four changes of position. The volume V of the dike is maintained around a

source	$\Delta\gamma$ (Pam^{-1})	radius (km)	patches	v (ms^{-1})	Δh_{eq} (m)
1	3500	3.1	742	0.54	775
2	3550	3.1	742	0.57	785
3	2733	3.3	852	0.33	644
4	2550	3.3	852	0.27	600
5	1675	3.7	1076	0.12	443
6	1425	3.9	1192	0.092	397
7	1300	3.9	1192	0.070	362
8	1100	4.1	1304	0.052	322
9	963	4.3	1448	0.042	296
10	900	4.3	1448	0.034	276
11	840	4.5	1588	0.033	270
12	775	4.5	1588	0.026	250
13	660	4.7	1732	0.019	222
14	635	4.7	1732	0.017	213
15	180	6.5	3302	0.0014	84

Table 3.2: Some parameters of the circular cross section dike at different locations along y-axis. The area of one patch of the boundary element discretization is of $0.2 \cdot 0.2$ km^2.

source	y-coordinate (km)	Δt (h min)		time (d h min)			mean, max opening (cm)	
1	4	-	-	0	00	10	45	86
2	4.8	0	30	0	00	40	45	88
3	5.6	0	20	0	01	00	40	77
4	6.4	0	40	0	01	40	37	72
5	7.2	0	50	0	02	30	31	59
6	8	1	10	0	03	40	29	56
7	8.8	2	25	0	06	10	26	51
8	9.6	3	10	0	09	20	24	47
9	10.4	4	16	0	13	40	24	46
10	11.2	5	17	0	19	00	23	44
11	12	6	32	1	01	30	22	43
12	12.8	6	44	1	08	10	21	40
13	13.6	8	33	1	16	40	19	37
14	14.4	11	42	2	04	20	18	36
15	15.2	13	04	2	17	20	10	19

Table 3.3: Parameters of the dike at different locations along y-axis. The time interval Δt is considered between the new position and the previous one. The Δt in the simulation have been rounded up or down to the nearest multiple of 10 min, which is the step employed for the time array in the code.

value of $1.3 \cdot 10^7$ m^3. The overpressure gradient $\Delta\gamma$ is calculated from the average topography the dike meets in its way, which is represented in fig. 3.39 by Maccaferri, Eleonora Rivalta, Passarelli, and Aoki (2016). To calculate the pressure gradient, I estimate the increment of lithostatic pressure as the dike migrates $\rho_{rock}g\Delta h$, where ρ_{rock} is the rock density (here set to 2800 kgm^{-3}), g the gravity acceleration and Δh is the height of topography. So I estimates a mean linear gradient in lithostatic pressure $\frac{\rho_{rock}g\Delta h}{\Delta y_{dike}}$ considering the average of linear gradients for distance steps of 1 km along the dike. These $\Delta\gamma$ change accordingly to the dike center position and the equivalent topography Δh_{eq} around it, the equivalent slopes for each dike are represented in fig. 3.40.
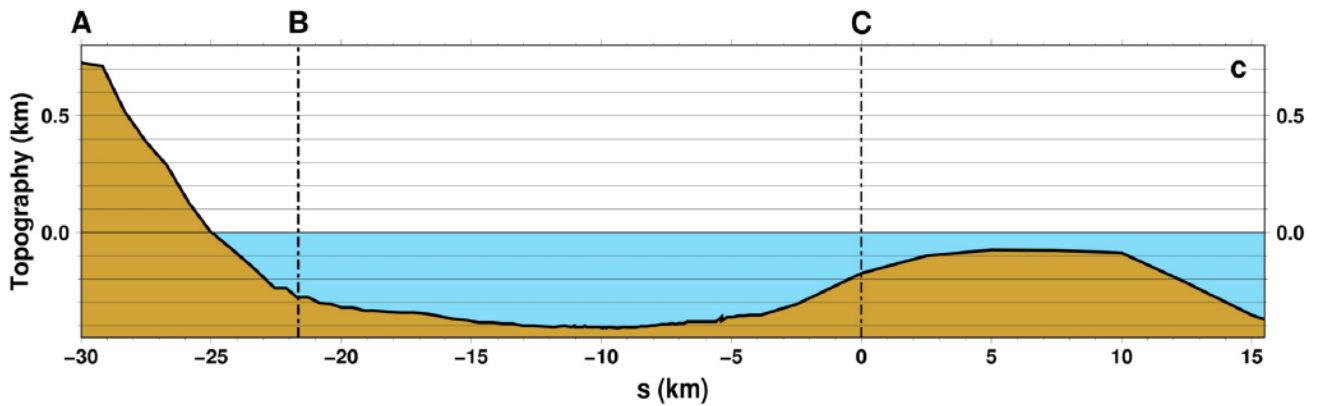
Figure 3.39: Topography profile obtained by averaging the topographic data from ETOPO1 (Amante and Eakins (2009)) on a circle of 1 km radius along the dike trajectory. Modified from a figure by Maccaferri, Eleonora Rivalta, Passarelli, and Aoki (2016).

3.3.2 Stress changes calculation and receiver faults

For computational efficiency reasons, the stresses and the opening of the dike are calculated in this case in a full-space elastic domain. The increasing number of patches for representing the sources, as it can be seen in table 3.2, and the large number of grid points for the computation of the stresses would generate too long computation times if the half-space medium is considered. Nevertheless the effect of the free surface would be not too large at this level of complexity of the modelling: I am primarily interested on examining the pattern of the spatial distribution of seismicity. As it can be seen in figures of the first scenario, the free surface essentially produces higher seismic rates above the dike than below it, because stress and strain are more concentrated. The Coulomb stresses in this case are considered only on dip-slip receiver faults.
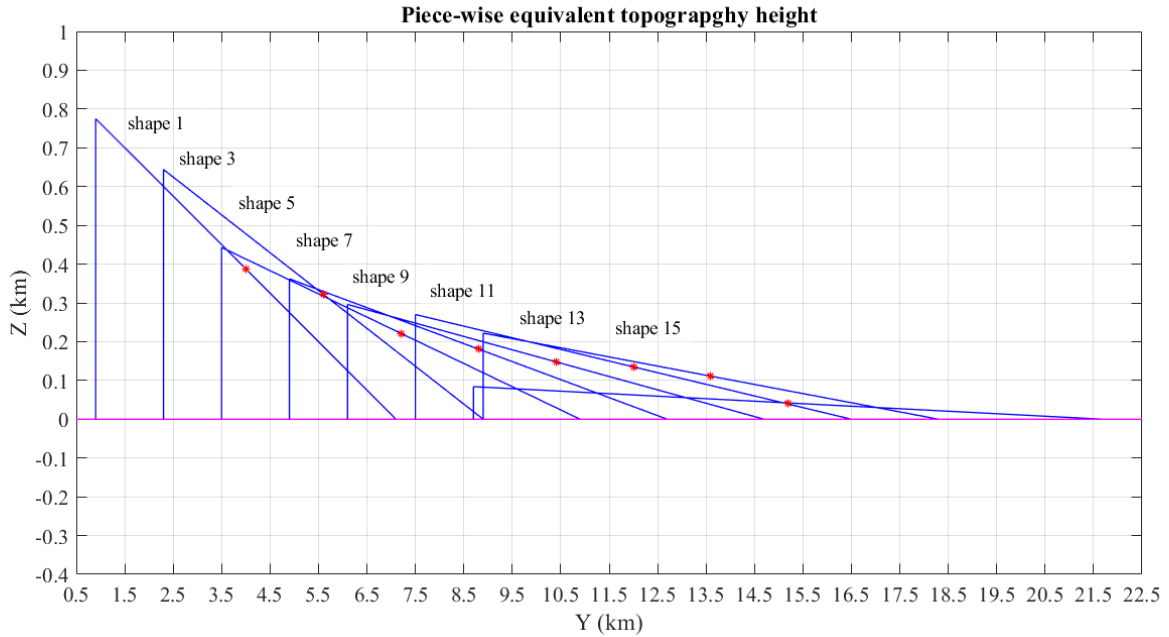
Figure 3.40: Diagram of the equivalent topography Δh_{eq} (Z) relative to the mean linear horizontal pressure gradient along the dike in some of the positions it takes during its propagation. Only odd number sources are represented for a better visualization. The simplified topography and mean linear gradients are estimated from fig. 3.39, considering the length covered by the dike in this scenario, from position -30 km to -8 km. Red dots indicate the positions of the dike center along the y-axis and the horizontal magenta line represents the baseline of topography, which corresponds to the lowest ocean bottom of fig. 3.39.

3.3.3   Relative seismic rate simulations

Results: relative seismic rates integrated on columns or rows of the volume of calculus

In the following figures (3.41, 3.42, 3.43, 3.44, 3.45, 3.46, 3.47, 3.48, 3.49 and 3.50) are reported the results relative to the simulation of the seismic rates for the second scenario and for dip-slip faults, as seen in map, frontal and lateral sections of the computation volume. In the figures the rates of each pixel are relative to the total amount of seismicity in the row/column perpendicular to the plane represented. Moreover only some instants are represented as it can be seen in the figures (details in the captions).

Analysing the figures in map view, it can be seen that the spatial pattern of seismicity develops while the dike decelerates and change its shape and size. The seismic rates concentrate upon the projection of the dike on the xy-plane and the diagonals that depart from its vertices, as expected for normal receiver faults. While the source of deformation proceeds the high seismicity pattern moves forward in a compact shape that becomes gradually thinner in the x-direction but elongates in the y-direction. Indeed while decelerating, the dike, which approximately maintains its volume, diminishes in thickness.

The front part and the region ahead of the dike are not particularly affected by previous opening events but only by the front of the dike propagating. Indeed the stress perturbation of the dike acts on the same background seismicity. In contrast the central and rear regions of the volume around the dike are more affected by every spatial step of the dike. The seismicity pattern develops two lateral tails of higher rates than the surrounding area. This is linked to when the dike starts to propagate and it would probably not be seen for a static dike that inflates. The effect of previous opening events depends also on the choice of the discretization of the dike motion. Here I have chosen a value of 0.8 km, which corresponds to two steps of the spatial grid, as a compromise between a small step and an efficient computational cost for simulating a large number of sources. The effect is more evident in lateral cross section figures. Considering smaller forward steps could be an alternative which would give a more continuous movement of the dike.

The natural consequence of the dike changing its aspect ratio is that the intrusion takes temporal intervals Δt (see table 3.3) gradually longer to cover 0.8 km of forward translation. Instead in yz figures it can be seen that the high seismicity region shrinks in the x-direction and stretches vertically on the z-direction. Furthermore, because the simulation is done for dip-slip normal receiver faults, in frontal view the highest values of the rates are found along oblique directions starting from the vertices of the dike, above and under the dike.

An important improvement to the model would be to reduce the spatial and temporal shifts. This would make the simulation probably more accurate and would lead to more compact spatial concentrations of the high seismicity rates. In particular, when the dike decelerates it happens that the change in the radius is larger than the spatial shift. In such cases, it could be good to shorten the step in order to represent a smoother spatio-temporal path of the source.

In figures 3.51 and 3.52 are represented the simulation for a spatial shift of 3 km, which is larger than the previous shift. This is probably a suboptimal choice, because of the tail effects that generate from the large forward steps of the source of stress change, which would correspond to a quasi-instantaneous fracture tip-line propagation of a few kilometers.
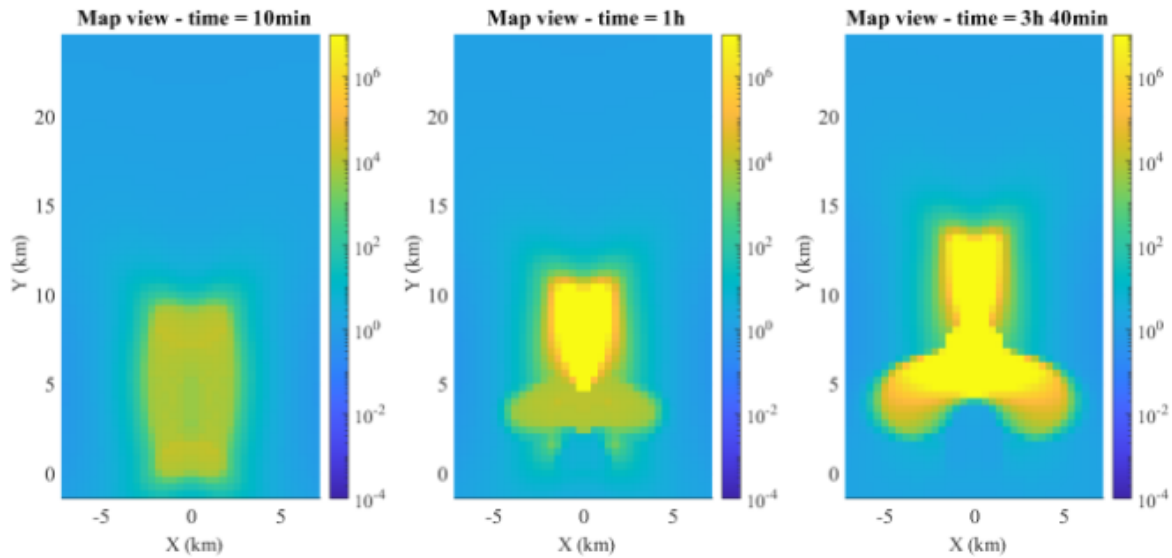
Figure 3.41: Map view of the spatial distribution of seismic rates, for dip-slip faults and a dike changing in size and velocity, at 10 min, 1 h and 3 h 40 min. In figures are reported the 1st, 3rd and 6th instants of dike opening at different locations.
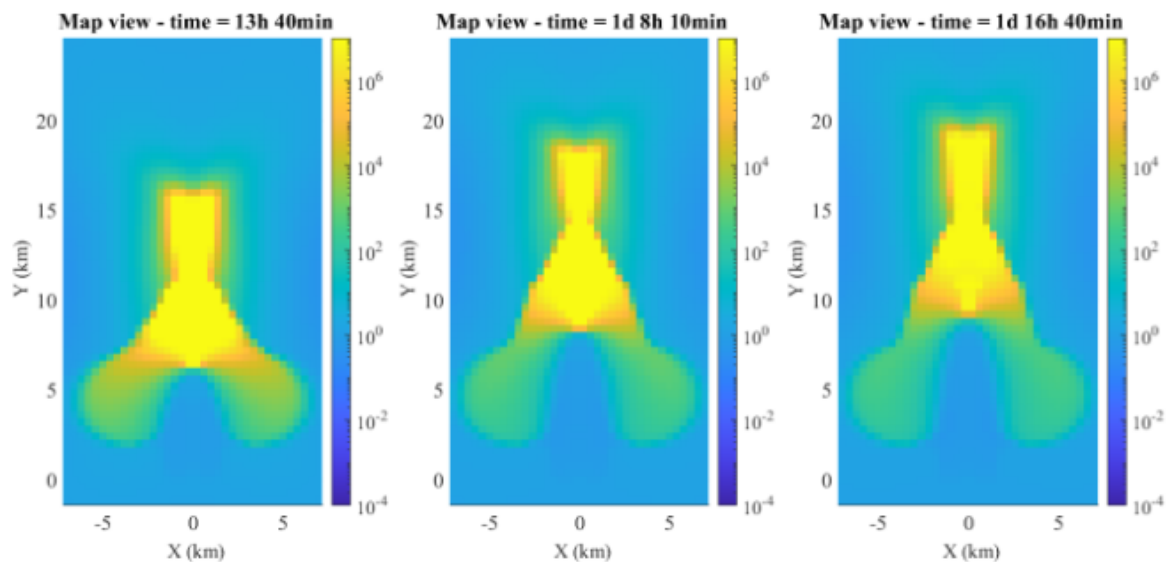
Figure 3.42: Map view of the spatial distribution of seismic rates, for dip-slip faults and a dike changing in size and velocity, at 13 h 40 min, 1 d 8 h 10 min and 1 d 16 h 40 min. In figures are reported the 9th, 12th and 13th instants of dike opening at different locations.

Figure 3.43: Map view of the spatial distribution of seismic rates, for dip-slip faults and a dike changing in size and velocity, at 2 d 4 h 20 min, 2 d 17 h 20 min and 5 d 10 h 30 min. In figures are reported the 14th and 15th instants of dike opening at different locations and an instant about three days after the last opening.

Figure 3.44: Frontal view of the spatial distribution of seismic rates, for dip-slip faults and a dike changing in size and velocity, at 10 min, 1 h and 3 h 40 min. In figures are reported the 1st, 3rd and 6th instants of dike opening at different locations.

Figure 3.45: Frontal view of the spatial distribution of seismic rates, for dip-slip faults and a dike changing in size and velocity, at 13 h 40 min, 1 d 8 h 10 min and 1 d 16 h 40 min. In figures are reported the 9th, 12th and 13th instants of dike opening at different locations.
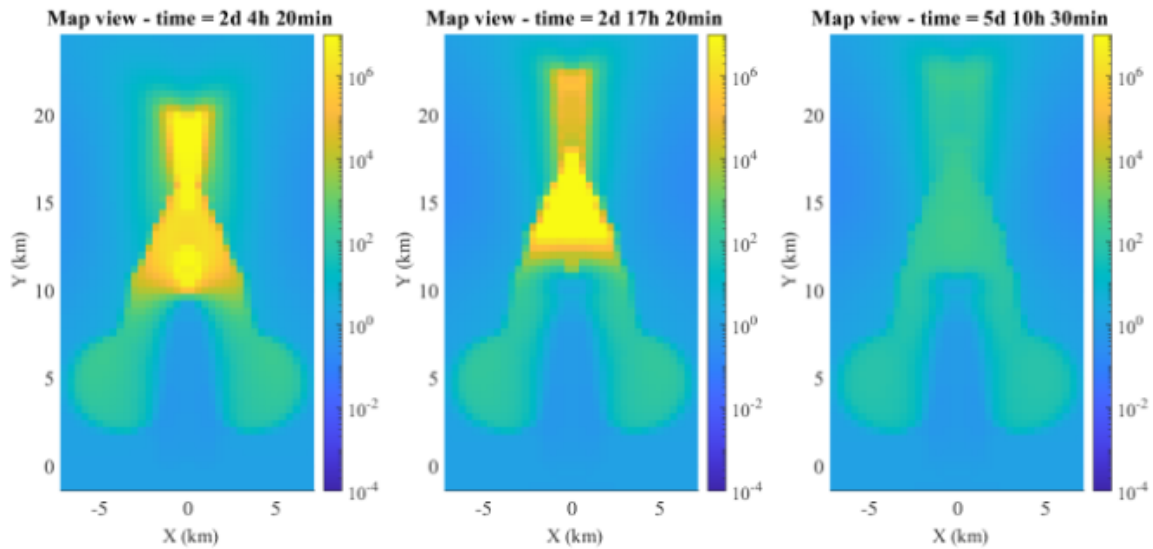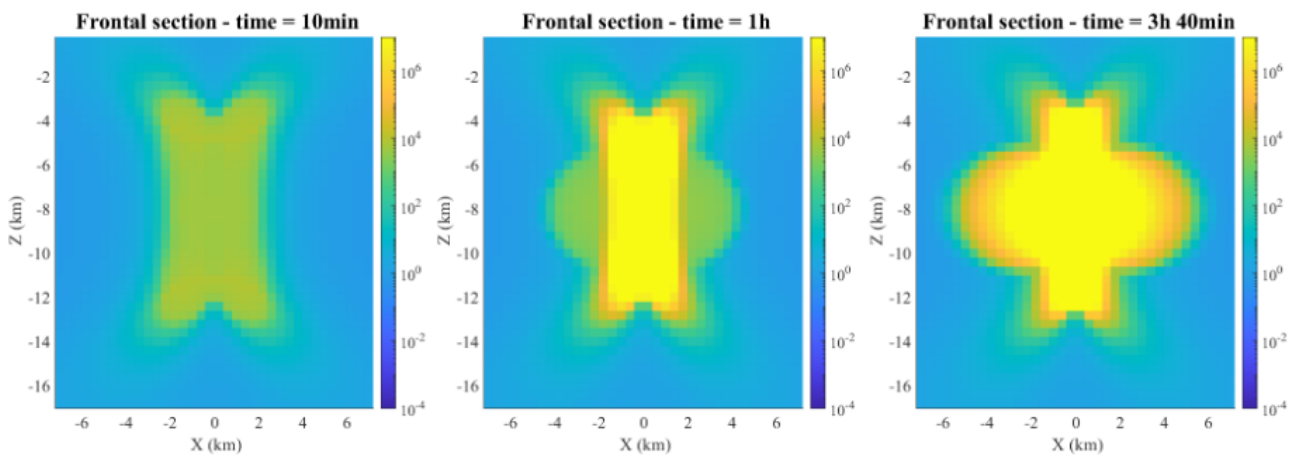

Figure 3.46: Frontal view of the spatial distribution of seismic rates, for dip-slip faults and a dike changing in size and velocity, at 2 d 4 h 20 min, 2 d 17 h 20 min and 5 d 10 h 30 min. In figures are reported the 14th and 15th instants of dike opening at different locations and an instant about three days after the last opening.

Figure 3.47: Lateral view of the spatial distribution of seismic rates, for dip-slip faults and a dike changing in size and velocity, at 10 min and 1 h. In figures are reported the 1st and 3rd instants of dike opening at different locations.
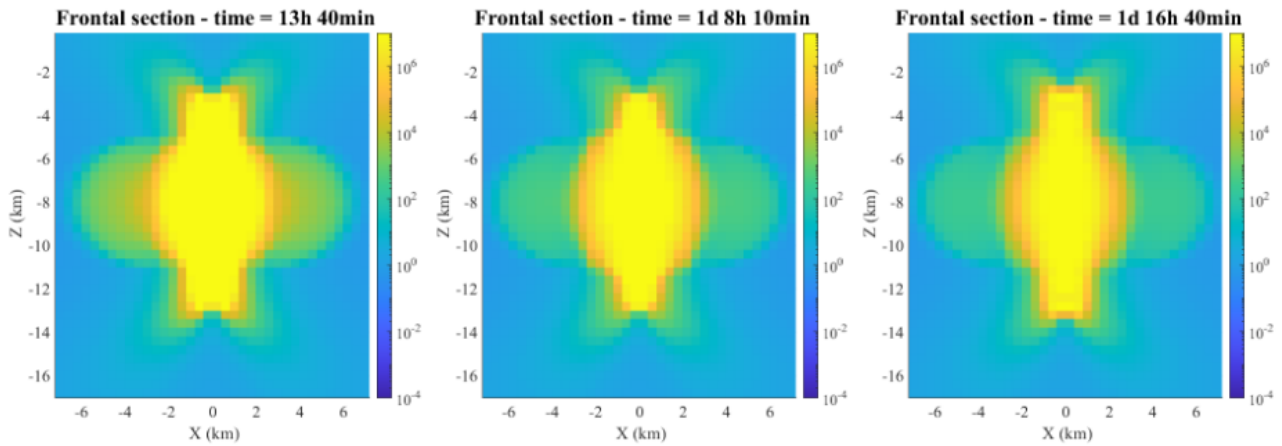

Figure 3.48: Lateral view of the spatial distribution of seismic rates, for dip-slip faults and a dike changing in size and velocity, at 3 h 40 min and 13 h 40 min. In figures are reported the 6th and 9th instants of dike opening at different locations.

Figure 3.49: Lateral view of the spatial distribution of seismic rates, for dip-slip faults and a dike changing in size and velocity, at 1 d 8 h 10 min and 1 d 16 h 40 min. In figures are reported the 12th and 13th instants of dike opening at different locations.
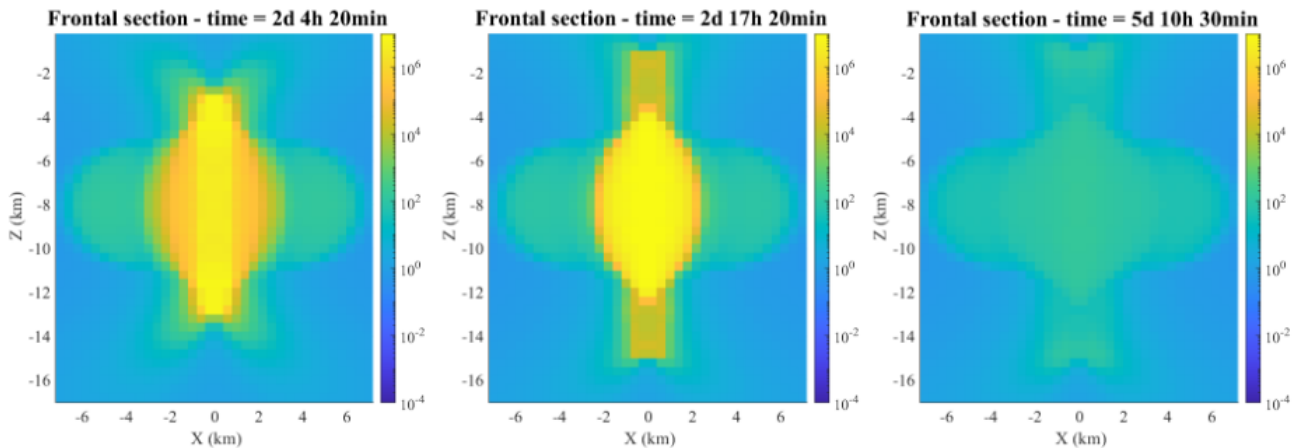

Figure 3.50: Lateral view of the spatial distribution of seismic rates, for dip-slip faults and a dike changing in size and velocity, at 2 d 4 h 20 min and 2 d 17 h 20 min. In figures are reported the 14th and 15th instants of dike opening at different locations.
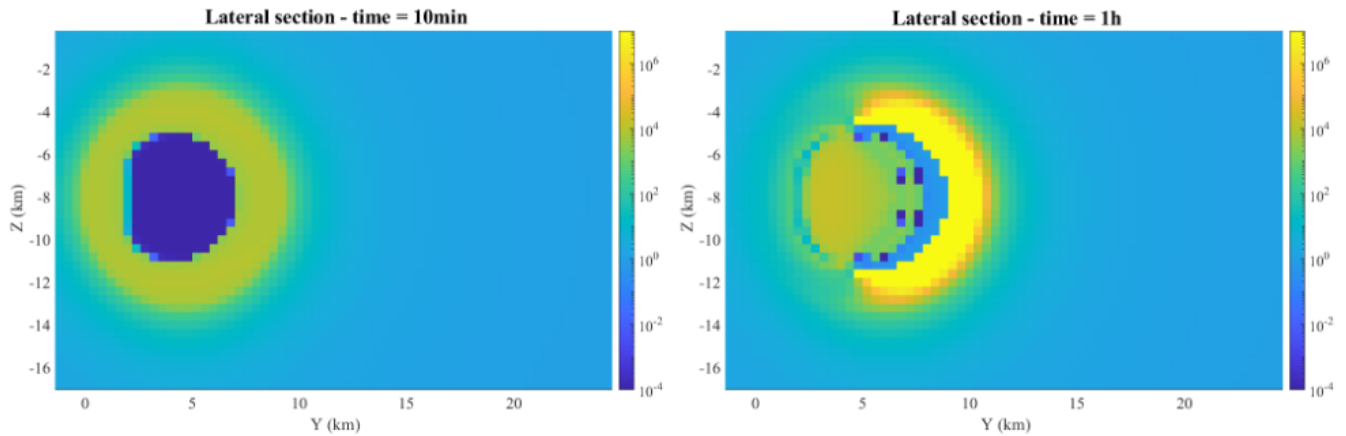
Figure 3.51: Map view of the spatial distribution of seismic rates, for dip-slip faults and a dike changing in size and velocity, at 2 h, 4 h and 8 h. In figures are reported the first three events of dike opening at different locations.
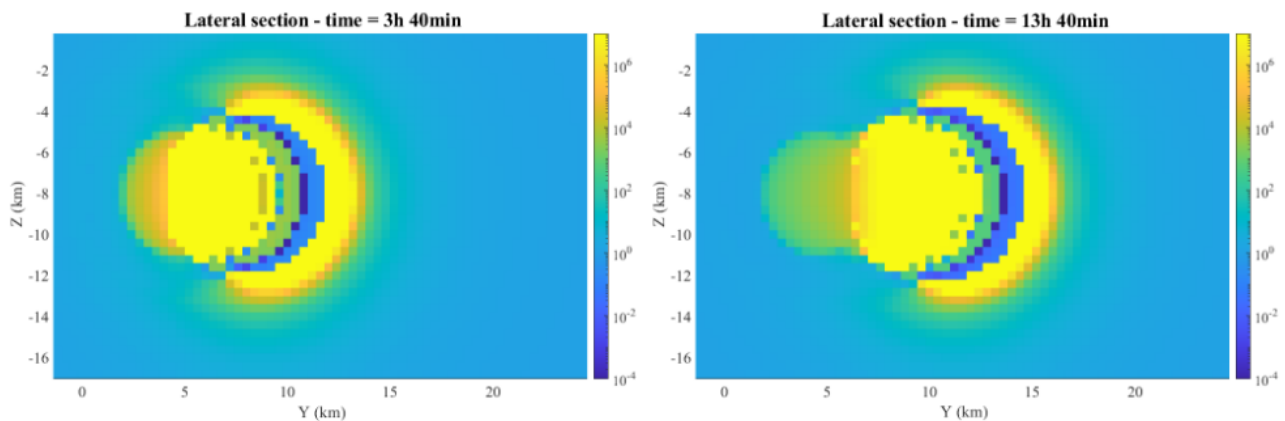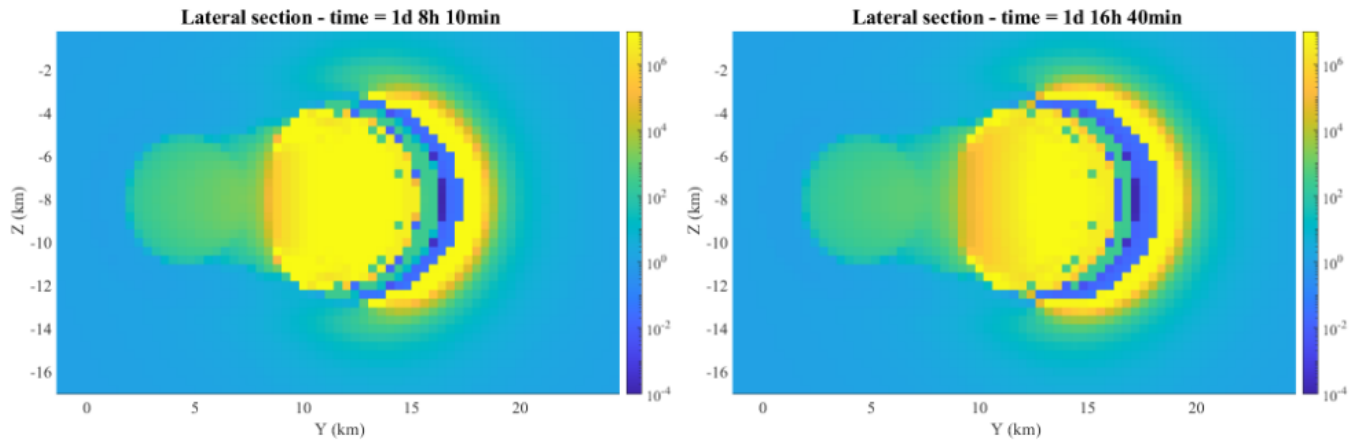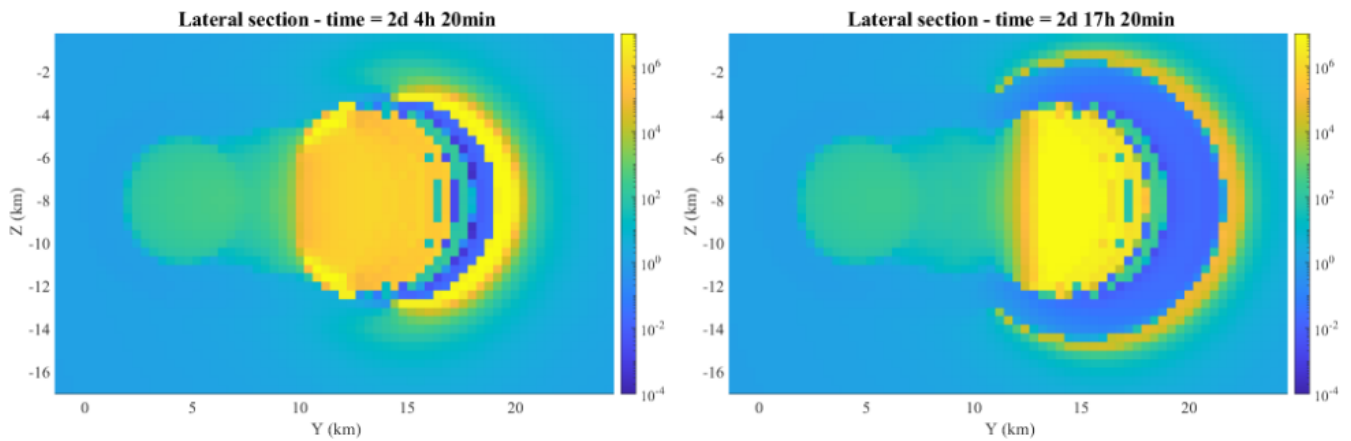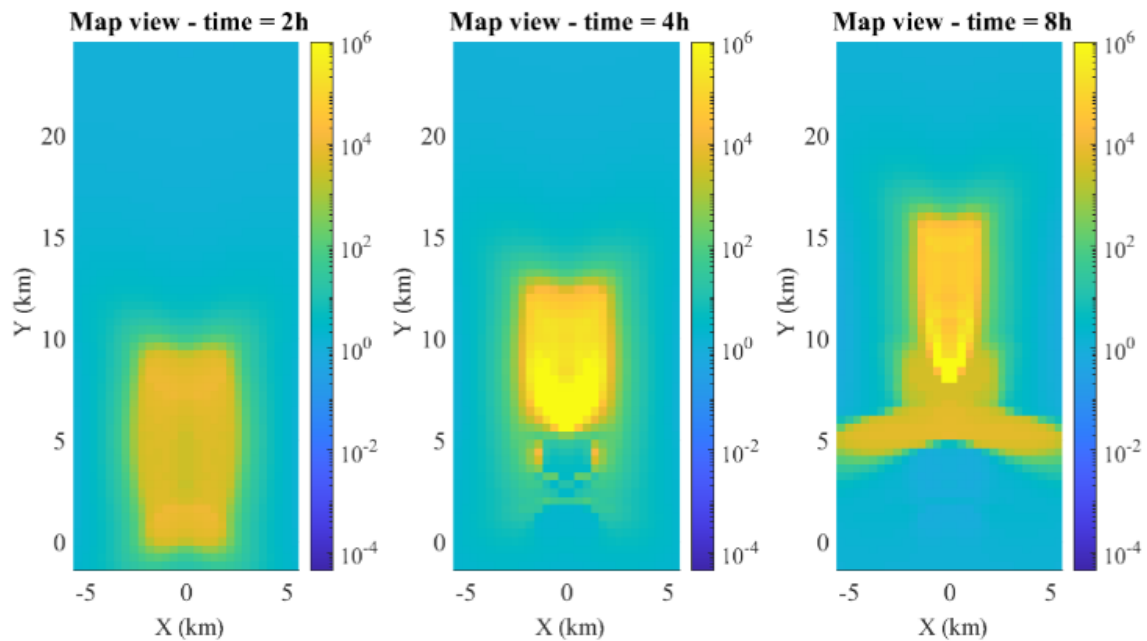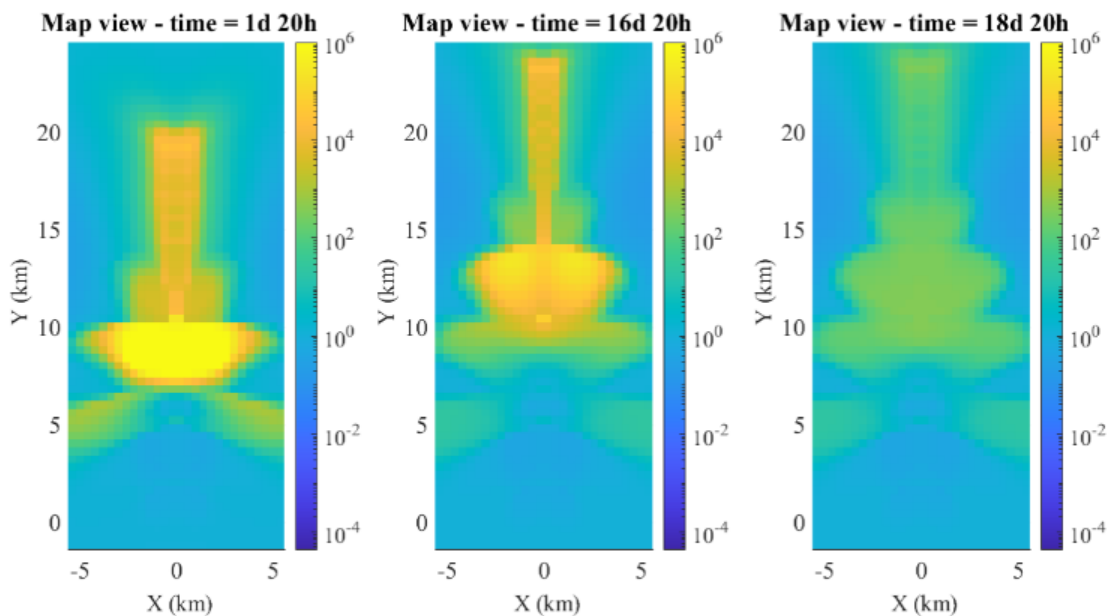

Figure 3.52: Map view of the spatial distribution of seismic rates, for dip-slip faults and a dike changing in size and velocity, at 1 d 20 h, 16 d 20 h and 18 d 20 h. In figures are reported the last two events of dike opening at different locations and the frame at two days after the last opening.

Chapter 4

Discussion and perspectives

4.1 Overview on the project

The focus of my thesis has been to develop a novel physical model for the seismicity induced by a propagating dike. As many observations have shown, an intense seismic activity accompanies propagating magma, including in areas that prior to the event showed very low seismicity rates(Belachew et al. (2011), Passarelli et al. (2015), Sigmundsson, Hooper, et al. (2015), Ágústsdóttir et al. (2019)). To do this, in chapter 3 I have developed two simple scenarios (with the second a little more complex) of propagating dikes in an elastic medium, reproducing some of the features of the propagation phase of the 2000 dike event at Miyakejima, Japan, and simulated the relative seismic rates. For the modeling of the dike (sec. 3.1.2) I have created a boundary element crack discretized in patches, taking inspiration for the shape from the analytical model by Davis, Eleonora Rivalta, and Dahm (2020), and applying a horizontal overpressure gradient in the direction of propagation of the intrusion.

For the modeling of the induced seismicity rates, I have implemented the physics-based rate-state model (J. Dieterich (1994)), based on Coulomb stress changes generated by a source of deformation, for the case of a series of step-like stress changes, such as those generated during the time intervals between different snapshots of the propagation. In particular, I have implemented equations by Hainzl, Steacy, and Marsan (2010), adapting them to my scenarios.

In the first scenario (sec. 3.2) the dike has a circular cross section, constant shape and volume and propagates at constant velocity. I use the velocity that has characterized the propagation phase of the intrusion of Miyakejima. The second scenario (sec. 3.2) introduces the effect of a decreasing topographic loading on the propagating dike, as a dike proceeds away from the volcanic edifice. This is a model for the decreasing topographic load affecting the dike during the first five days of the event at Miyakejima (Maccaferri, Eleonora Rivalta, Passarelli, and Aoki (2016)). In this simulation the volume of the dike is maintained constant

and so the circular section shape, while its size and velocity change. In reality, the dike was continuously fed by the magma chamber, so these models are still simplifying the natural case I selected.

4.2   Discussion of the results

As presented in chapter 1, the patterns of seismicity induced by dikes can be various and complex also because there are other factors that can play a role in seismicity such as heterogeneity in the weakness of the crust and other sources of stress redistribution that can have an impact on the earthquake distribution. What is common in many plots of temporal distribution of seismicity along the dike path is that the propagating phase is linked to a compact cloud of epicenters that moves together with the advancing fronts of the dike. This is visible in the plots in map view of my simulations: a yellow concentration of high seismicity moves with the dike and is followed behind by blue pixels of low rates. The seismic rate falls in the regions surpassed by the dike. Nevertheless the real phenomena have more complexities that my models does not consider. The other part of the plots (figures 1.5, 1.7 (c), 1.10 (a)), after a dike arrest, show a more complex pattern in which the seismicity partially migrate backwards along the dike path. Other factors probably intervene such as an interaction with pre-loaded faults (Maccaferri, Eleonora Rivalta, Passarelli, and Aoki (2016)) which for example, as shown in fig. 1.9, can inhibit earthquakes to the south of the strike-slip fault near Kozushima island and promote them to north of it, or aseismic slips (fig. 1.10, Cattania et al. (2017)) which can delay seismic activity producing slow slip events. Another factor could be the inflation of an arrested dike caused by new supply of magma from a reservoir, as happened at Miyakejima (Japan) in 2000 (Passarelli et al. (2015)) and Bardarbunga (Iceland) in 2014 (Ágústsdóttir et al. (2019)).

The two scenarios I have built in chapter 3, simulate the seismic distribution only for the propagation phase of a dike and in the case of a constant volume intrusion without newly supplied magma from a magma chamber, or loss of, e.g. through freezing. Another important point to stress is that the rate simulated are not absolute (R) but relative ($\frac{R}{r_0}$), meaning normalized with respect to the background seismic rate r_0, which is relative to a particular focal mechanism and magnitudes above a certain threshold. What the two simulations are able to catch of the seismic pattern of the event at Miyakejima reported in figure 1.9 (a) is certainly the compactness of the cloud of epicenters as it migrates together with the dike. This is visible in the comparison of figures in map view, and of those in lateral view. An important difference is visible from the lateral view plots of simulations and that of figure 1.9 (a). Indeed while in the simulations the hypocenters appear to be distributed over the entire vertical extension of the dike, in the real case they concentrates at the lower edge of the dike while shallower earthquakes are less and more sparse. This is something not yet entirely understood and that will need more examinations. The dike models used to reproduce the deformation and seismicity observed are various in size and depth, but they all have a greater concentration of earthquakes
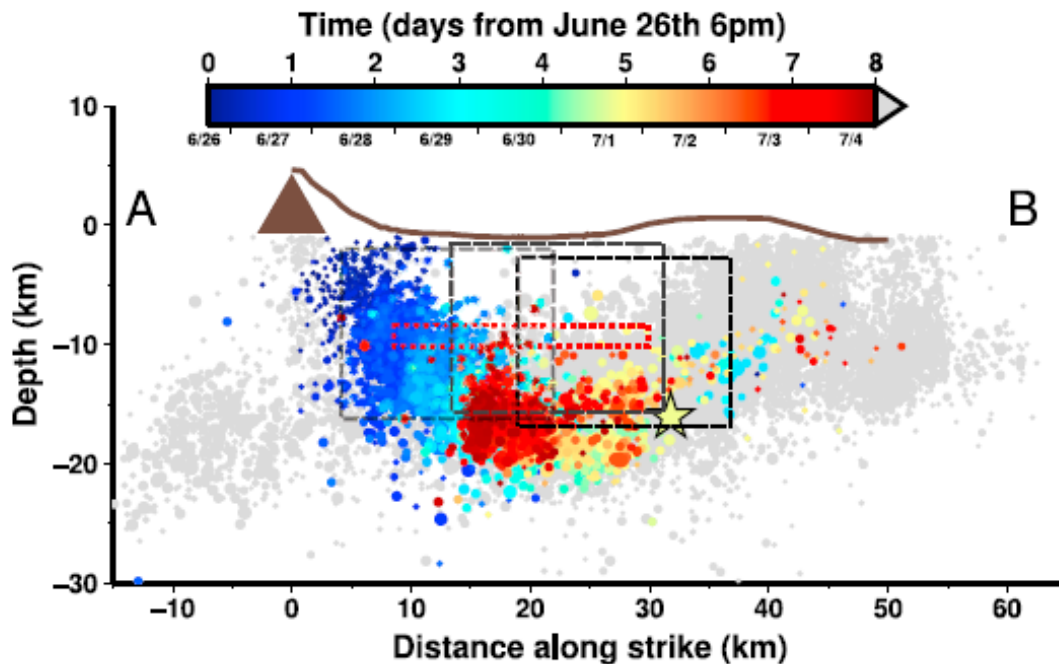
Figure 4.1: Cross section of the distribution of seismicity of the 2000 dike event at the Miyakejima volcano (brown triangle) for the first eight days. Figure 2 from Passarelli et al. (2015).

at deeper depths (see fig. 4.1 by Passarelli et al. (2015)). This pattern is similar to that observed at the Bardarbunga volcano in 2014 (see fig. 1.7). As suggested by Woods et al. (2019) it may be due to an initial aseismic slip at shallower depths due to a more weak and fractured rock medium. They suggest that the fracturing to happen needs that the ambient differential stress combined with that generated by a dike, to be sufficiently high and probably the former is not sufficient at shallower depths. It is more likely enough to induce earthquakes at more deep depths near the brittle-ductile transition of the Earth's crust (see Ágústsdóttir et al. (2019) as reference).

The two types of receiver faults employed in the simulations, strike-slip and normal faults, have been chosen consistently with the focal mechanisms observed during the 2000 dike event (Passarelli et al. (2015)) and the tectonic setting of the region. This makes consistent and reasonable a visual comparison of the plots of the simulations with those of the observed seismicity. Though is important to remember that for a quantitative confrontation it would be necessary to evaluate r_0 and then R from the relative seismic rate calculated in the simulations. As shown in figure 1.11 by Passarelli et al. (2015), which refers to the entire dike event, the strike-slip earthquakes cover depths between 5 and 20 km while the normal faulting is detected only between 5 and 10 km of depth, which means above the dike intrusion. This results means that maybe for the dip-slip events the simulations needs to take into account different conditions on the elastic properties of the medium at different depths. Moreover in figure 1.12 by

Passarelli et al. (2015), the distribution of normal and strike-slip mechanisms reflects the pattern expected by a tensile source of deformation acting on those types of receiving faults, with the former type striking parallel to the dike and the latter striking some acute angle between 45 and 60 degrees (see for comparison figure 3.26 and 3.24 relative to simulations respectively for strike-slip and dip-slip receiver faults).

Another aspect that appears to be reproduced in the simulation is the pattern of epicenters in figure 1.13 by Maccaferri, Eleonora Rivalta, Passarelli, and Aoki (2016). Although the mechanism of arrest and deceleration of the dike was a combination of a decreasing topography loading at the surface above the dike and its interaction with a strike-slip fault to the east of Kuzushima, the second scenario I have simulated, has produced similar results. Comparing the map view plot of seismicity of figures 3.41, 3.42 and 3.43 with figure 1.13, it can be recognized in the simulated plots that the lateral extension of the cloud of epicenters shrinks while the front of the dike advances.

4.3   Limits of the simulations and perspectives

Rheology of the crust and dike-fault interactions

The scenarios I have designed in chapter 3 are preliminary and do not take into account some factors that influence the event at the Miyakejima. Some further elements that could be introduced to improve the representation of the event and the agreement with the data, are: an interaction of the propagating dike with a strike-slip fault as analysed by Maccaferri, Eleonora Rivalta, Passarelli, and Aoki (2016); a spatial diversification of the brittle-elastic properties of the rock medium to take into account possible aseismic slips, maybe modifying the value of the parameter $t_a = \frac{A\sigma}{\dot{\tau}}$ of the rate-state model, which, as shown in section 3.2, influence the seismic response in terms of rates and temporal scale of rate decay; and the influence of the larger earthquakes on the induced seismicity.

Dike representation and extension to time-variable mass and volume of magma

Another important element of the simulations that is feasible to improve in future developments of this project, is the representation of the dike. A better modeling of the source of stress change can produce more detailed spatial pattern of seismicity rates. Using rectangular dislocations for the discretization of the dike plane does not give a perfect closure of the dike at the edges. This influences the rate calculations in the nearest grid points to the source. Besides increasing the number of patches to discretize more finely the dike, which would however add computational cost, a possible improvement could be achieved by using triangular dislocations, e.g. using the code byDavis, Eleonora Rivalta, and Dahm (2020). As it can be seen in figure 4.2, a discretization of the dike plane with triangular dislocations would help to better represent more complex shapes of the dike and in particular its edges. Moreover it could be

an improvement to my simulations to use a numerical method for the evolution of the dike shape and directions of propagation such that of Davis, Eleonora Rivalta, and Dahm (2020), in which to evaluate the propagating edges of the dike is use the ratio $\frac{K_I}{K_C}$ between the mode-I stress intensity factor and the critical one, for each patch of the tip-line. The ratio is a criterion for propagation because it represent the propensity to fracturing of the surrounding rock near the tip-line. These upgrades of my models would make the dike evolution more detailed and probably realistic.

A factor that I do not have considered but it could be important not only in the simulation of the propagating phase of the dike at the Miyakejima but also for its successive inflation phase, is to integrate in the model a time-variable mass and volume of the dike. It could take into account the interaction of the dike with the magma chamber, which continued to supply magma to the propagating intrusion, and with the caldera that formed during the 2000 dike event of Miyakejima, in consequence of the deflation of the magma chamber. The mass transport between the magma chamber and the dike could be constrained by the ground deformation data at the surface and imposing conservation of the mass in the overall system.
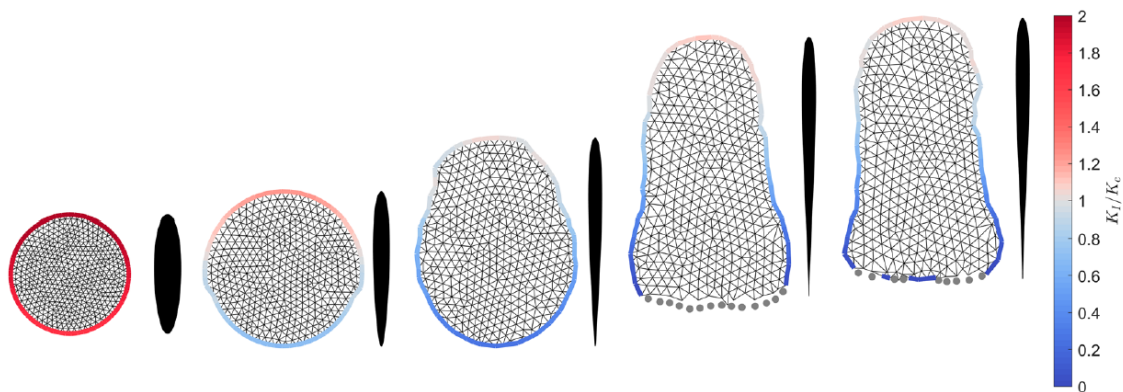
Figure 4.2: Cross sections and crack planes of a numerical simulation of a propagating dike using a discretization of the crack plane in triangular patches. The gray dots indicate closed patches and the color scale indicates the propensity of the dike edge to propagate through fracturig of the rock. Figure 2 from Davis, Eleonora Rivalta, and Dahm (2020).

Calibration and forecasting capability of the models

Lastly, the next steps following this thesis, could be to calibrate the parameters of the models I have built, and test their possible capability to forecast seismic rates given a certain evolution of a propagating source of stress change such as a dike. The idea is to train my models of the two scenarios using a portion of the data from the JMA catalog of hypocenters, relative to the first period of the propagation. Through a trial and error method it is possible to find the better choices for the parameters of the rate-state model (in particular $\dot{\tau}$, t_a and r_0) that

optimize the agreement between simulated rates and observed data. After the calibration it would be possible to test the potential capability of forecasting of the models by giving in input the model of the propagating dike and confronting the results of simulations with the observed pattern of seismicity. This part would help to investigate the potential of physics-based seismicity models as the rate-state and maybe the mechanisms behind events such that at the Miyakejima. Moreover there exist other alternative models for induced seismicity, such that by Dahm and Hainzl (2022), based on Coulomb stress changes, that could be implemented in similar scenarios to those presented here, and tested against data.

Appendix A

Matlab code for the implementation of the seismicity rate model

Here I report the MATLAB code I have developed for the simulations of the propagating dike, as source of stress and deformation, and of the seismicity rates through the formulas presented at the end of chapter 2. In the following pages you will find:

1. The main code for the simulation of the stresses of scenario 1 (for dip-slip receiver faults);

2. The function for the modeling of the dike (used at points 1 and 4);

3. The functions for the calculations of the receiver faults' optimum orientations and the Coulomb stresses (used at points 1 and 4);

4. The main code for the simulation of the stresses of scenario 2;

5. The main code for the implementation of the rate-state formulas of section 2.7.1;

6. The function for the calculation of the temporal evolution of the state variable γ;

A.1   Stress for scenario 1 - Main

```
tic
%% 3D Grid of calculus
%spatial step in the x: east, y: north, z: up directions in km
passox=0.4; passoy=0.4; passoz=0.4;
%spatial grid (larger) for calculations of stresses through translations of
%the grid: this because while the dike propagates forward it maintain its
%shape and size and so does the stress it generates
```

```
[Xg,Yg,Zg] = meshgrid(-6.2:passox:6.2,-21.2:passoy:29.2,-9:passoz:0);
lxg=length(Xg(1,:,1)); lyg=length(Yg(:,1,1)); lzg=length(Zg(1,1,:));
Ng_grid=lyg*lxg*lzg;
%spatial grid (smaller) for seismic rates calculations and plots
[X,Y,Z] = meshgrid(-6.2:passox:6.2,-1.2:passoy:29.2,-9:passoz:0);
lx=length(X(1,:,1)); ly=length(Y(:,1,1)); lz=length(Z(1,1,:));
N_grid=ly*lx*lz; %n punti griglia
%time array
lt=66; t=zeros(1,lt); dt=9*10^3; %2,5 hours in seconds
for i=1:length(t)
    t(i)=(i-1)*dt;
end


%% SOURCES of stress:
dike modeled with rectangular tensile boundary elements
% positions and instants of the center of the translating dike
Nsor=40; %number of positions of the dike
Xd=zeros(Nsor,3); %array of the positions of the dike
%Cartesian coordinates of the first position of the source
xo=0; yo=4; zo=-4.4;

t_ind=(2:41); %array of the indices of tsor
%array of the instants of appearance of the dike in a new position
tsor=(t_ind-1)*dt;

%number of patches, horizontal and vertical, of the discretization of
%the dike plane and extensions of one patch in the y and z directions
n_o=31; n_v=31; passoy_p=0.2; passoz_p=0.2;
Dgamma= 1550e3; % Pa/km, horizontal overpressure gradient

Stress_dtot=zeros(Ng_grid,6); %stress on the larger grid, generated
%by the dike, the six components of the stress tensor are in order:
%sxx, syy, szz, sxy, sxz, syz
%function to calculate the stresses of the dike on the larger grid
[Stress_dtot,time1,time2]=stress_dike_BEM(Xg,Yg,Zg,xo,yo,zo, ...
    n_o,n_v,passoy_p,passoz_p,Dgamma);

%% Coulomb stress computation on DIP-SLIP faults
%tensorial form of the stress just computed
Stress_dtot_tens1=reshape(Stress_dtot(:,1), size(Xg));
Stress_dtot_tens2=reshape(Stress_dtot(:,2), size(Xg));
```

```matlab
Stress_dtot_tens3=reshape(Stress_dtot(:,3), size(Xg));
Stress_dtot_tens4=reshape(Stress_dtot(:,4), size(Xg));
Stress_dtot_tens5=reshape(Stress_dtot(:,5), size(Xg));
Stress_dtot_tens6=reshape(Stress_dtot(:,6), size(Xg));

%array of the stress on the smaller grid for the successive calculation of
%the seismic rates, for each of the different position of the source-dike
stressdtot=zeros(N_grid,6,Nsor);
%arrays of the six components of stress on the smaller grid (are temporary)
stressdtot1=zeros(ly,lx,lz); stressdtot2=zeros(ly,lx,lz);
stressdtot3=zeros(ly,lx,lz); stressdtot4=zeros(ly,lx,lz);
stressdtot5=zeros(ly,lx,lz); stressdtot6=zeros(ly,lx,lz);

%calculation of the stresses on the smaller grid for a forward translation
%of the dike in the y-direction, of a spatial step equal to a spatial step
%of the grid, which means 0.4 km
for i=1:Nsor %number of the postion of the propagation of the dike
 ya=51-1*(i-1); yb=127-1*(i-1);
 stressdtot1(:,:,:)=Stress_dtot_tens1(ya:yb,:,:); stressdtot1_v=stressdtot1(:);
 stressdtot2(:,:,:)=Stress_dtot_tens2(ya:yb,:,:); stressdtot2_v=stressdtot2(:);
 stressdtot3(:,:,:)=Stress_dtot_tens3(ya:yb,:,:); stressdtot3_v=stressdtot3(:);
 stressdtot4(:,:,:)=Stress_dtot_tens4(ya:yb,:,:); stressdtot4_v=stressdtot4(:);
 stressdtot5(:,:,:)=Stress_dtot_tens5(ya:yb,:,:); stressdtot5_v=stressdtot5(:);
 stressdtot6(:,:,:)=Stress_dtot_tens6(ya:yb,:,:); stressdtot6_v=stressdtot6(:);
 stressdtot(:,1,i)=stressdtot1_v(:); stressdtot(:,2,i)=stressdtot2_v(:);
 stressdtot(:,3,i)=stressdtot3_v(:); stressdtot(:,4,i)=stressdtot4_v(:);
 stressdtot(:,5,i)=stressdtot5_v(:); stressdtot(:,6,i)=stressdtot6_v(:);
end

%tectonic stressing rate
sigma_xx_dot=8*10^(-4); stressrate=[sigma_xx_dot 0 0; 0 0 0; 0 0 -1*10^(-7)];
mup=0.4; %effective friction coefficient
%optimally oriented fault planes with respect to the tectonic stressing rate
%shear stressing rate, normal direction and direction of slip of the faults
dottau=zeros(1,2); n=zeros(3,2); d=zeros(3,2);
[~,d(:,1),n(:,1),d(:,2),n(:,2),dip(1,1),dip(1,2)]=CFSmax([stressrate(1,1) ...
stressrate(2,2) stressrate(3,3) stressrate(1,2) stressrate(1,3) ...
stressrate(2,3)],mup);
dottau(1,1)=(stressrate*n(:,1))'*d(:,1); dottau(1,2)=(stressrate*n(:,2))'*d(:,2);
D_CFS=zeros(N_grid,Nsor,2); %2 is the number of dip-slip receiver faults
D_CFS_cutoff=0.5e6; %see Cattania (2015)
```

```matlab
for i=1:N_grid
    %compute the Coulomb stress in a point, for the first position of the dike
    [D_CFS(i,1,1),~,~]=D_C6(stressdtot(i,:,1),mup,n(:,1),d(:,1));
    [D_CFS(i,1,2),~,~]=D_C6(stressdtot(i,:,1),mup,n(:,2),d(:,2));
    if D_CFS(i,1,1) > D_CFS_cutoff
       D_CFS(i,1,1)=D_CFS_cutoff;
    end
    if D_CFS(i,1,2) > D_CFS_cutoff
       D_CFS(i,1,2)=D_CFS_cutoff;
    end
    if D_CFS(i,1,1) < -D_CFS_cutoff
       D_CFS(i,1,1)=-D_CFS_cutoff;
    end
    if D_CFS(i,1,2) < -D_CFS_cutoff
       D_CFS(i,1,2)=-D_CFS_cutoff;
    end
end
stresstot=zeros(N_grid,6);
for j=2:Nsor
    stresstot=stressdtot(:,:,j)-stressdtot(:,:,j-1);
    for i=1:N_grid
        %compute the Coulomb stress in a point, for the positions of the dike
        %following the first
        [D_CFS(i,j,1),~,~]=D_C6(stresstot(i,:),mup,n(:,1),d(:,1));
        [D_CFS(i,j,2),~,~]=D_C6(stresstot(i,:),mup,n(:,2),d(:,2));
        if D_CFS(i,j,1) > D_CFS_cutoff
            D_CFS(i,j,1)=D_CFS_cutoff;
        end
        if D_CFS(i,j,2) > D_CFS_cutoff
            D_CFS(i,j,2)=D_CFS_cutoff;
        end
        if D_CFS(i,j,1) < -D_CFS_cutoff
            D_CFS(i,j,1)=-D_CFS_cutoff;
        end
        if D_CFS(i,j,2) < -D_CFS_cutoff
            D_CFS(i,j,2)=-D_CFS_cutoff;
        end
    end
end
save('stress_scenario1.mat')
toc
```

A.2   Functions for the modelling of the dike

A.2.1   Function stress_dike_BEM.m

```
function [Stress_dtot,time1,time2]=stress_dike_BEM(X_in_grid,Y_in_grid, ...
Z_in_grid,xof,yof,zof,no,nv,passoy_in,passoz_in,Dgamma_in)

%spatial and temporal grid
X=X_in_grid; Y=Y_in_grid; Z=Z_in_grid;
lx=length(X(1,:,1)); ly=length(Y(:,1,1)); lz=length(Z(1,1,:));
N_grid=ly*lx*lz; %n punti griglia
%position of the center of the dike
xo=xof; yo=yof; zo=zof;

%horizontal, vertical and total number of patches for the dike discretization
n_o=no; n_v=nv; Npat=n_o*n_v;
passoy_p=passoy_in; passoz_p=passoz_in;
Lf=n_o*passoy_p; Wf=n_v*passoz_p; plunge = 0; dip = 90; strike = 0; rake = 0;
mu = 0.33e11; lambda = 0.33e11; %in Pa
RefPoint = 'Pc'; slip=0; Dgamma= Dgamma_in;

%function dikeBEM_HS_ellip compute the openings on the patches of the dike
%given a boundary condition of the pressure on each patch
[b,maxb,meanb,X0,Y0,Z0,L,W]=dikeBEM_HS_ellip(Dgamma,Lf,Wf,xo,yo,zo,n_o, ...
n_v,plunge,dip,strike,rake);
%order of the elements in 1D vector b: z=1, x=1, y=1,2,3,...;
%z=1, x=2, y=1,2,3,... etc.; X0, Y0, Z0 are column vectors of Nsor elements
depth=-Z0;  opening=b;
time1=toc;

%compute the stresses generated by all the patches and their sum, on
%the larger grid of calculus of the main code (Xg,Yg,Zg)
Stress_d=zeros(N_grid,6); Stress_dtot=zeros(N_grid,6);
for i=1:Npat
    [Stress_d(:,:),~] = RDstressHS(X,Y,Z,X0(i),Y0(i),depth(i),L,W,plunge, ...
    dip,strike,rake,slip,opening(i),mu,lambda,RefPoint);
    Stress_dtot=Stress_dtot+Stress_d;
end
%RDstressHS.m: function by Nikkhoo et al. (2016)
time2=toc;
```

A.2.2   Function dikeBEM_HS_ellip.m

```
function [b2,maxb,meanb,Xd00,Yd00,Zd00,L,W]=dikeBEM_HS_ellip(Dgamma,Lf, ...
Wf,xof,yof,zof,n_o,n_v,plunge,dip,strike,...
    rake)
%% Geometry of the dike, the initial dike plane is rectangular with dip=90
%then it will take an elliptical/circular shape
L1=Lf; W1=Wf; %extensions of the rectangular plane
A=L1/2; B=W1/2; c=L1/2; p_meno=-Dgamma*c/3; %see Davis,Rivalta, and Dahm (2020)
%for the model, spatial dimensions in km
xo=xof; yo=yof; zo=zof; %center of the dike
%horizontal extremities of the rectangular plane of the dike
XdA=xo; XdB=xo; YdA=yo-L1/2; YdB=yo+L1/2;
%vertical extremities, from the most shallow to the deepest:
%RDstressHS.m uses positive depths
ZdA=zo-W1/2; ZdB=zo+W1/2;
norizz=n_o; nz=n_v; dy=L1/norizz; dz=W1/nz;

Xd=((XdA+dx/2):dx:XdB); %array in a row of norizz elements, relative to
%the centers of the patches
Yd=((YdA+dy/2):dy:YdB); %array in a row of norizz elements
Zd=((ZdA+dz/2):dz:ZdB); %array in a row of nz elements

Xd0=zeros(norizz,nz); Yd0=Xd0; Zd0=Xd0;
%in alternative to classical meshgrid, for the plots
for i=1:norizz
    Zd0(i,:)=Zd;
end
for i=1:nz
    Xd0(:,i)=Xd;
    Yd0(:,i)=Yd;
end
Xd00=Xd0(:); Yd00=Yd0(:); Zd00=Zd0(:);
k=0;
for j=1:nz
    for i=1:norizz
        if Yd0(i,j)>=yo-sqrt(A^2-(Zd0(i,j)-zof)^2*A^2/B^2) ...
            && Yd0(i,j)<=yo+sqrt(A^2-(Zd0(i,j)-zof)^2*A^2/B^2)
             k=k+1;
             Yd1(k)=Yd0(i,j);
             Zd1(k)=Zd0(i,j);
```

```
                press(k,1)=p_meno+2*Dgamma*c*(i-1)/(norizz-1);
            end
        end
end
Y0=Yd1(:); Z0=Zd1(:); X0=zeros(length(Y0),1); %column vectors

%geometry of one patch
L = L1/norizz; W = W1/nz; %extensions of a single patch
plunge1 = plunge; dip1 = dip; strike1 = strike; rake1 = rake;
slip = 0; opening = 1; %opening=1 for computation of tensor G
mu = 0.33e11; lambda = 0.33e11; RefPoint = 'Pc';

% compute the influence coefficients G (see boundary elements in chapter 2)
G=zeros(length(X0),length(X0));
%the order of the patches: from left to right and from down to up
for i=1:length(X0)
  [Stress,~] = RDstressHS(X0,Y0,Z0,X0(i),Y0(i),-Z0(i),L,W,plunge1,dip1,...
      strike1,rake1,slip,opening,mu,lambda,RefPoint);
  G(:,i)=Stress(:,1); %stress(pressure) in one location at a time
  %generated by a unit opening by i-th patch
end
stress_normal=-press;
b=G\stress_normal; %b=G^(-1)tau %x = A\b MATLAB formalism for the
%inverse matrix for linear systems of equations
k=find(b<0); maxb=max(b)*1e5; meanb=mean(b)*1e5;
minb=min(b)*1e5;

b1=zeros(norizz,nz); h=0;
for j=1:nz %to make elliptical/circular the plane/cross sectino of the dike
    for i=1:norizz
        if Yd0(i,j)>=yo-sqrt(A^2-(Zd0(i,j)-zof)^2*A^2/B^2) ...
            && Yd0(i,j)<=yo+sqrt(A^2-(Zd0(i,j)-zof)^2*A^2/B^2)
            h=h+1;
            if b(h)<0 %to avoid negative openings
                b1(i,j)=0;
            else
                b1(i,j)=b(h);
            end
        end
    end
end b2=b1(:);
```

A.3   Function CFSmax.m and D_C6.m

This function computes the normal vector and the vector of slip for a couple of optimally ori-
ented fault planes relatively to a stress field. It is used in the main codes for stress calculations
in scenario 1 and 2.

CFSmax.m

```
function [CFSmax,d1p,n1p,d2p,n2p,dip1,dip2]=CFSmax(stressin,mup)
[sigma1Vec,sigma2Vec,sigma3Vec,sigma1,sigma2,sigma3]=...
    calcPrincipalStress(stressin);
sig1=-sigma1; sig2=-sigma2; sig3=-sigma3;
gamma=atan(1/mup)/2; %For real values of X, atan(X) returns values
%in the interval [-pi/2,pi/2]

d1=[-cos(gamma) 0 sin(gamma)]'; n1=[sin(gamma) 0 cos(gamma)]';
d2=[-cos(gamma) 0 -sin(gamma)]'; n2=[sin(gamma) 0 -cos(gamma)]';

M=[sigma1Vec',sigma2Vec',sigma3Vec'];
d1p=M*d1; n1p=M*n1; d2p=M*d2; n2p=M*n2;  % normal and slip versors
%with respect to the plane of the fault
dip1=acos(n1p(3)); dip2=acos(n2p(3)); % in radianti!!
if dip1*180/pi > 90
    dip1=pi-dip1;
end
if dip2*180/pi > 90
    dip2=pi-dip2;
end
CFSmax=(sig3-sig1)/2*sqrt(1+mup^2)+(sig3+sig1)/2*mup;
% see "Fundamentals fo Structural Geology" di Raymond C. Fletcher, David D.
% Pollard, 2005, capitolo 9.3
```

calcPrincipalStress.m

It is used to calculate the principal stresses and vectors of a stress field.

```
function [sigma1Vec,sigma2Vec,sigma3Vec,sigma1,sigma2,sigma3]=...
    calcPrincipalStress(Stress)
% Calculates the orientations of principal stresses
Np = size(Stress,1); sigma1 = zeros(Np,1); sigma2 = zeros(Np,1);
sigma3 = zeros(Np,1); sigma1Vec = zeros(Np,3); sigma2Vec = zeros(Np,3);
sigma3Vec = zeros(Np,3);
```

```matlab
for k=1:Np
    St = [Stress(k,1) Stress(k,4) Stress(k,5); Stress(k,4) Stress(k,2) ...
          Stress(k,6); Stress(k,5) Stress(k,6) Stress(k,3)];
    if isnan(trace(St))
        St = zeros(3);
    end
    [Vk,Dk] = eig(-St); % For positive compressive stresses
    [sigma,Ind] = sort(diag(Dk));
    sigma1(k) = sigma(3); % Maximum eigenvalue (maximum compressive)
    sigma2(k) = sigma(2); % Intermediate eigenvalue
    sigma3(k) = sigma(1); % Minimum eigenvalue (least compressive)
    % sigma3(k) = min(diag(squeeze(Dk)));
    sigma1Vec(k,:) = Vk(:,Ind(3))'; sigma2Vec(k,:) = Vk(:,Ind(2))';
    sigma3Vec(k,:) = Vk(:,Ind(1))';
    sigma1Vec(k,:) = sigma1Vec(k,:)/norm(sigma1Vec(k,:));
    sigma2Vec(k,:) = sigma2Vec(k,:)/norm(sigma2Vec(k,:));
    sigma3Vec(k,:) = sigma3Vec(k,:)/norm(sigma3Vec(k,:));
end
```

D_C6.m

It computes the Coulomb stress given a stress field and a fault plane characterized by a normal
and a slip vectors.

```matlab
function [D_C,N,S]=D_C6(stress,mup,n,d) %n e d column vectors
si=[stress(1) stress(4) stress(5);stress(4) stress(2) stress(6); ...
    stress(5) stress(6) stress(3)];
N=(si*n)'*n; %normal component of traction
S=(si*n)'*d; %shear component of traction, along the rake direction
D_C=S+mup*N; %0.4 is the effective friction coefficient
```

A.4   Stress for scenario 2 - Main

```matlab
%% 3D Grid of calculus
%spatial steps in the x: east, y: north, z: up directions in km
passox=0.4; passoy=0.4; passoz=0.4;
%spatial grid
[Xg2,Yg2,Zg2] = meshgrid(-7.4:passox:7.4,-1.2:passoy:25,-16.8:passoz:0);
lxg=length(Xg2(1,:,1)); lyg=length(Yg2(:,1,1)); lzg=length(Zg2(1,1,:));
Ng_grid=lyg*lxg*lzg;
%time array
```

```
lt=785; t=zeros(1,lt); dt=600; %10 min in seconds
for i=1:length(t)
    t(i)=(i-1)*dt;
end

%% SOURCES of stress:
dike modeled with rectangular tensile boundary elements
% positions and instants of the center of the moving dike
Nsor=15; %number of positions of the dike
Xd=zeros(Nsor,3); % array of the positions of the dike
xo=0; yo=4; zo=-4.4; %Cartesian coordinates of the first position
ds=0.8; %forward spatial step of 0.8km
% positions of all the different sources: dike moves and changes size
Xd(1,1)=xo; Xd(1,2)=yo; Xd(1,3)=zo; Xd(2,1)=xo; Xd(2,2)=yo+ds; Xd(2,3)=zo;
Xd(3,1)=xo; Xd(3,2)=yo+ds*2; Xd(3,3)=zo; Xd(4,1)=xo; Xd(4,2)=yo+ds*3;
Xd(4,3)=zo; Xd(5,1)=xo; Xd(5,2)=yo+ds*4; Xd(5,3)=zo; Xd(6,1)=xo;
Xd(6,2)=yo+ds*5; Xd(6,3)=zo; Xd(7,1)=xo; Xd(7,2)=yo+ds*6; Xd(7,3)=zo;
Xd(8,1)=xo; Xd(8,2)=yo+ds*7; Xd(8,3)=zo; Xd(9,1)=xo; Xd(9,2)=yo+ds*8;
Xd(9,3)=zo; Xd(10,1)=xo; Xd(10,2)=yo+ds*9; Xd(10,3)=zo; Xd(11,1)=xo;
Xd(11,2)=yo+ds*10; Xd(11,3)=zo; Xd(12,1)=xo; Xd(12,2)=yo+ds*11; Xd(12,3)=zo;
Xd(13,1)=xo; Xd(13,2)=yo+ds*12; Xd(13,3)=zo; Xd(14,1)=xo; Xd(14,2)=yo+ds*13;
Xd(14,3)=zo; Xd(15,1)=xo; Xd(15,2)=yo+ds*14; Xd(15,3)=zo;
%array of the indices of the following array tsor
t_ind=[2,5,7,11,16,23,38,57,83,115,154,194,245,315,393];
%array of the instants of appearance of the dike in a new position
tsor=(t_ind-1)*dt;

%number of patches, horizontal and vertical, of the discretization
%of the dike plane
passoy_p=0.2; passoz_p=0.2; %extensions of a patch in the y and z directions
n_o1=31; n_v1=31; Dgamma1= 3500e3; % Pa/km, horizontal overpressure gradient
n_o2=31; n_v2=31; Dgamma2= 3550e3; n_o3=33; n_v3=33; Dgamma3= 2733e3;
n_o4=33; n_v4=33; Dgamma4= 2550e3; n_o5=37; n_v5=37; Dgamma5= 1675e3;
n_o6=39; n_v6=39; Dgamma6= 1425e3; n_o7=39; n_v7=39; Dgamma7= 1300e3;
n_o8=41; n_v8=41; Dgamma8= 1100e3; n_o9=43; n_v9=43; Dgamma9= 963e3;
n_o10=43; n_v10=43; Dgamma10= 900e3; n_o11=45; n_v11=45; Dgamma11= 840e3;
n_o12=45; n_v12=45; Dgamma12= 775e3; n_o13=47; n_v13=47; Dgamma13= 660e3;
n_o14=47; n_v14=47; Dgamma14= 635e3; n_o15=65; n_v15=65; Dgamma15= 180e3;

%(initialization) stress generated by the dike in each position
%the six components of the stress tensor (see main code scenario 1)
```

```
Stress_dtot1=zeros(Ng_grid,6);
Stress_dtot2=zeros(Ng_grid,6); Stress_dtot3=zeros(Ng_grid,6);
Stress_dtot4=zeros(Ng_grid,6); Stress_dtot5=zeros(Ng_grid,6);
Stress_dtot6=zeros(Ng_grid,6); Stress_dtot7=zeros(Ng_grid,6);
Stress_dtot8=zeros(Ng_grid,6); Stress_dtot9=zeros(Ng_grid,6);
Stress_dtot10=zeros(Ng_grid,6); Stress_dtot11=zeros(Ng_grid,6);
Stress_dtot12=zeros(Ng_grid,6); Stress_dtot13=zeros(Ng_grid,6);
Stress_dtot14=zeros(Ng_grid,6); Stress_dtot15=zeros(Ng_grid,6);

%the stress is calculated one source at a time changing the numbers from 1
%to 15 in the following lines
%the difference between stress_dike_BEM2.m and stress_dike_BEM.m is that
%the first considers a fullspace medium while the second an halfspace:
%the first uses RDstressFS.m instead of RDstressHS.m (by Nikkhoo et al.(2016))
[Stress_dtot15,time1,time2]=stress_dike_BEM2(Xg2,Yg2,Zg2,Xd(15,1), ...
    Xd(15,2),Xd(15,3),n_o15,n_v15,passoy_p,passoz_p,Dgamma15);
Stress_dtot15b=Stress_dtot15;

%% Coulomb stress computation on DIP-SLIP faults
stressdtot=zeros(Ng_grid,6,Nsor);
stressdtot(:,:,1)=Stress_dtot1(:,:); stressdtot(:,:,2)=Stress_dtot2(:,:);
stressdtot(:,:,3)=Stress_dtot3(:,:); stressdtot(:,:,4)=Stress_dtot4(:,:);
stressdtot(:,:,5)=Stress_dtot5(:,:); stressdtot(:,:,6)=Stress_dtot6(:,:);
stressdtot(:,:,7)=Stress_dtot7(:,:); stressdtot(:,:,8)=Stress_dtot8(:,:);
stressdtot(:,:,9)=Stress_dtot9(:,:); stressdtot(:,:,10)=Stress_dtot10(:,:);
stressdtot(:,:,11)=Stress_dtot11(:,:); stressdtot(:,:,12)=Stress_dtot12(:,:);
stressdtot(:,:,13)=Stress_dtot13(:,:); stressdtot(:,:,14)=Stress_dtot14(:,:);
stressdtot(:,:,15)=Stress_dtot15(:,:);

%the following part is the same of the main code for scenario 1:
%tectonic stressing rate
sigma_xx_dot=8*10^(-4); stressrate=[sigma_xx_dot 0 0; 0 0 0; 0 0 -1*10^(-7)];
[...]
[...]
        if D_CFS(i,j,2) < -D_CFS_cutoff
            D_CFS(i,j,2)=-D_CFS_cutoff;
        end
    end
end
save('stress_scenario2.mat')
toc
```

A.5   Seismic rates for scenarios 1 and 2 - Main

```matlab
load('stress_scenario.mat')
%SEISMIC RATES, rate-state model
w=[1/2 1/2]; %equal weights for the two dip-slip faults

As=0.048*10^6; %t_a of about 4 yr
R1=zeros(N_grid,lt,2);

%dottau in Pa/s, is the shear stressing rate, the same in every location
%array N_grid x lt x 2
[gamma]=gamma(N_grid,t,t_ind,dt,As,dottau(1,:),D_CFS(:,:,:));
numeratore=ones(N_grid,lt,2);
numeratore(:,:,1)=numeratore(:,:,1)/dottau(1,1)*w(1);
numeratore(:,:,2)=numeratore(:,:,2)/dottau(1,2)*w(2);
%R1 e R are 'relative rates', which means R/r0
R1=numeratore./gamma;
R=sum(R1,3); %weighted mean

Rtens=zeros(ly,lx,lz,lt);
for i=1:length(t)
    %R in tensor form for different time instants
    Rtens(:,:,:,i)=reshape(R(:,i),size(X));
end

%R summed over the z direction
Rtotz=squeeze(sum(Rtens,3)); %dimensions (y,x,1,t)
Rtotz(:,:,[lt])=[]; %delete the last instant
Rtotz=Rtotz*passox*passoy*passoz; %this is the value for a column
%volume of the spatial grid of calculus

%R summed over the y direction
Rtoty=squeeze(sum(Rtens,1)); %dimensions (1,x,z,t)
%this is the value for a row in the y direction
Rtoty(:,:,[lt])=[]; Rtoty=Rtoty*passox*passoy*passoz;

%R summed over the x direction
Rtotx=squeeze(sum(Rtens,2)); %dimensions (y,1,z,t)
%this is the value for a row in the x direction
Rtotx(:,:,[lt])=[]; Rtotx=Rtotx*passox*passoy*passoz;
save('seismic_rates.mat')
```

A.6   Function for the evolution of the variable γ: gamma.m

```matlab
function [gamma]=gamma(N_grid,t,t_ind,dt,As,dottau1,D_CFS)
dottau=zeros(1,1,length(dottau1)); dottau(1,1,:)=dottau1;
lt=length(t); lind=length(t_ind); gamma=zeros(N_grid,lt,2);
for i=1:(20-lind) %the code is built for a maximum of 20 sources
 t_ind=[t_ind,lt]; %it is needed to make the code work
end
tsor=(t_ind-1)*dt; %real instants of the sources
for i=1:N_grid  %gamma varies from location to location
 for j=1:lt  %gamma at each time step
  if t(j) < t(t_ind(1))
   gamma(i,j,:)=1./dottau; %gamma(1) is gamma0
  end
  if t(j) >= t(t_ind(1)) && t(j) < t(t_ind(2))
   gamma(i,j,:)=1./dottau+(1./dottau.*exp(-D_CFS(i,1,:)/As)-1./dottau) ...
   .*exp(-(t(j)-tsor(1)).*dottau/As);
  end
  if t(j) >= t(t_ind(2)) && t(j) < t(t_ind(3))
   gamma2=1./dottau+(1./dottau.*exp(-D_CFS(i,1,:)/As)-1./dottau) ...
   .*exp(-(tsor(2)-tsor(1)).*dottau/As);
   gamma(i,j,:)=1./dottau+(gamma2.*exp(-D_CFS(i,2,:)/As)-1./dottau) ...
   .*exp(-(t(j)-tsor(2)).*dottau/As);
  end
  if t(j) >= t(t_ind(3)) && t(j) < t(t_ind(4))
  gamma3=1./dottau+(gamma2.*exp(-D_CFS(i,2,:)/As)-1./dottau) ...
   .*exp(-(tsor(3)-tsor(2)).*dottau/As);
   gamma(i,j,:)=1./dottau+(gamma3.*exp(-D_CFS(i,3,:)/As)-1./dottau) ...
   .*exp(-(t(j)-tsor(3)).*dottau/As);
  end
[...]
  if t_ind(20) ~= lt
   if t(j) >= t(t_ind(20))
    gamma20=1./dottau+(gamma19.*exp(-D_CFS(i,19,:)/As)-1./dottau) ...
    .*exp(-(tsor(20)-tsor(19)).*dottau/As);
    gamma(i,j,:)=1./dottau+(gamma20.*exp(-D_CFS(i,20,:)/As)-1./dottau) ...
    .*exp(-(t(j)-tsor(20)).*dottau/As);
   end
  end
 end
end
```
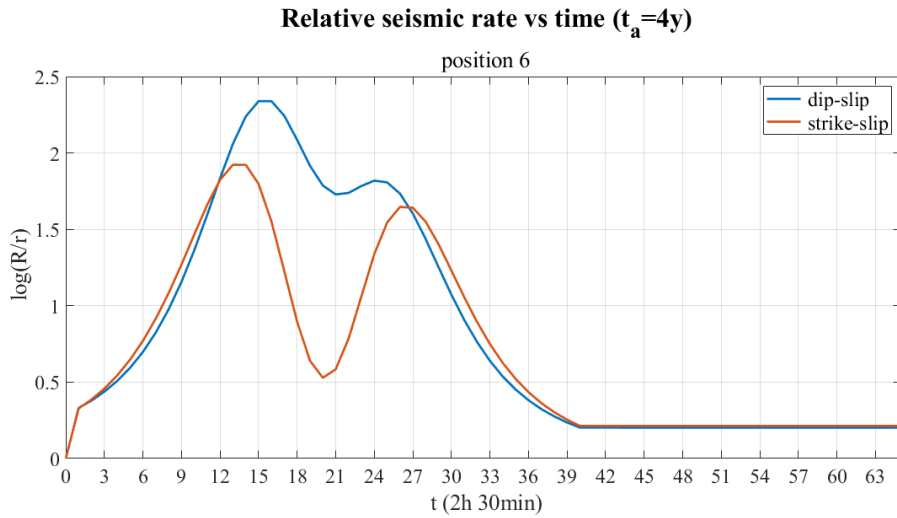
Appendix B

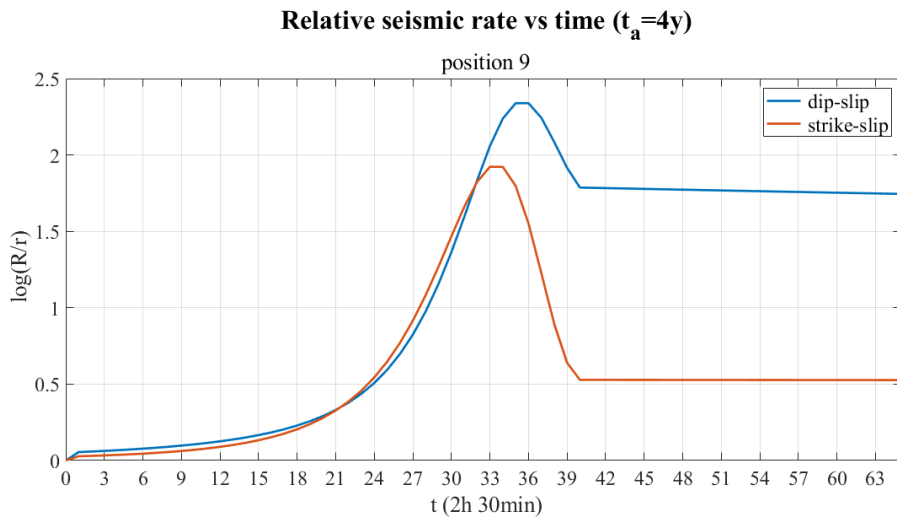# Relative seismic rates vs time and space

Rates at single locations and in frontal section view, for scenario 1
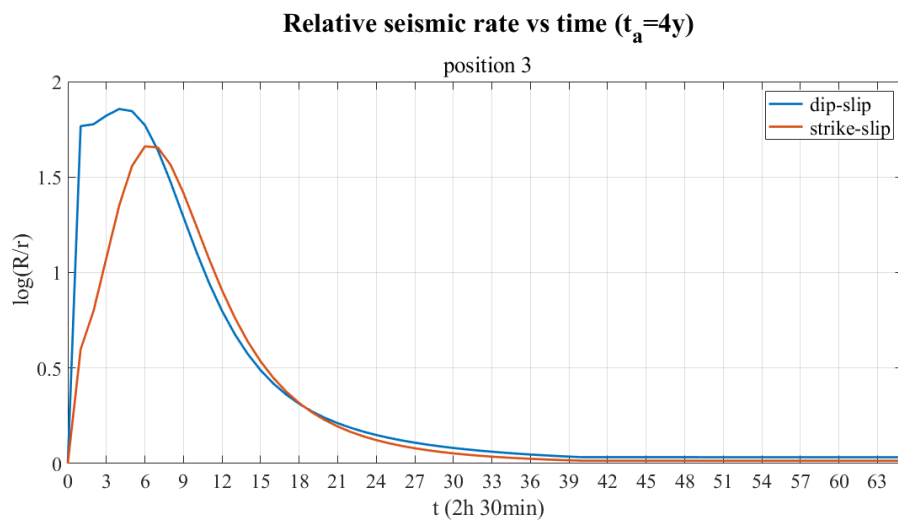
Figure B.1: Decimal logarithm of relative seismic rates versus time, at position P3, for both dip-slip and strike-slip faults.

Figure B.2: Decimal logarithm of relative seismic rates versus time, at position P6, for both dip-slip and strike-slip faults.
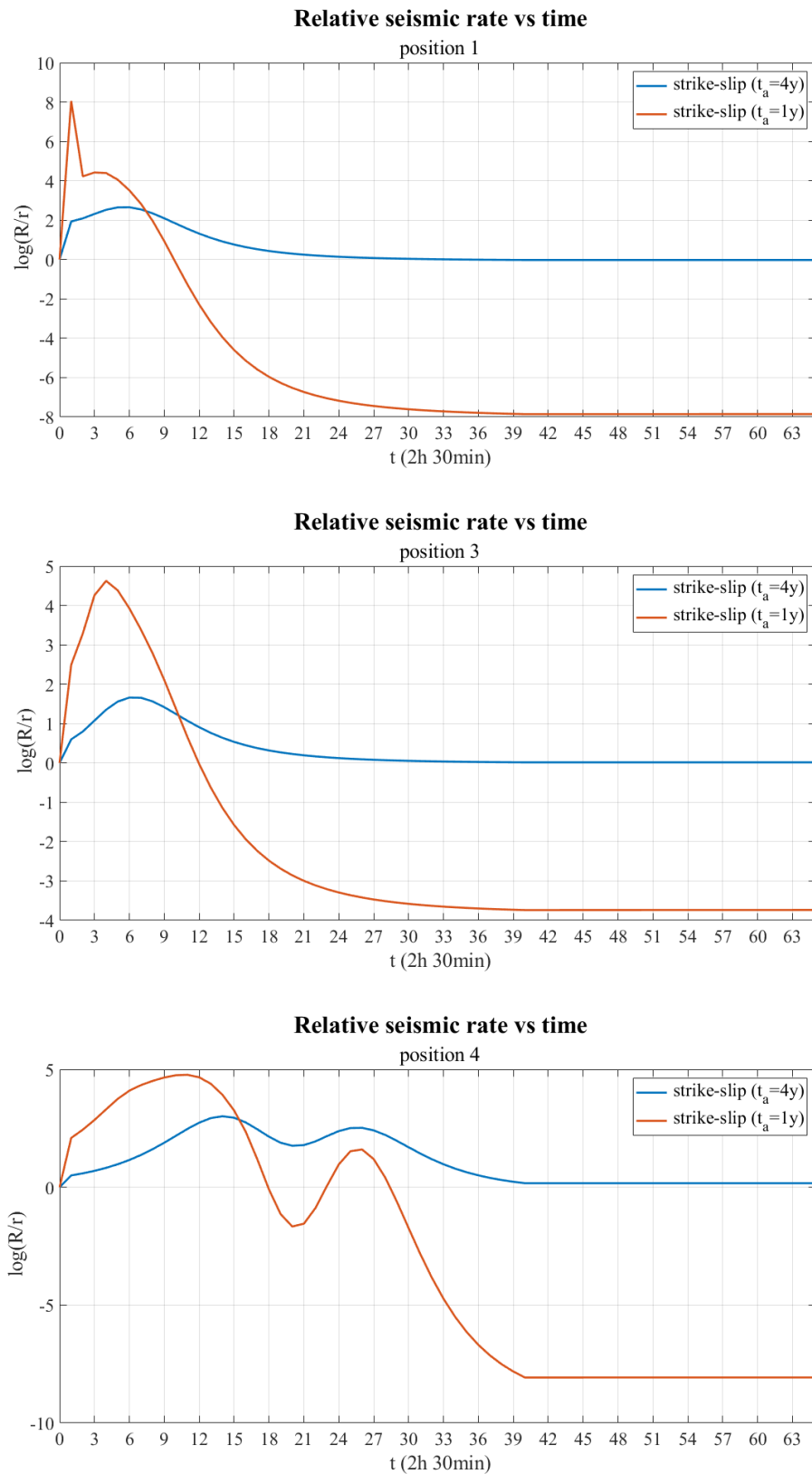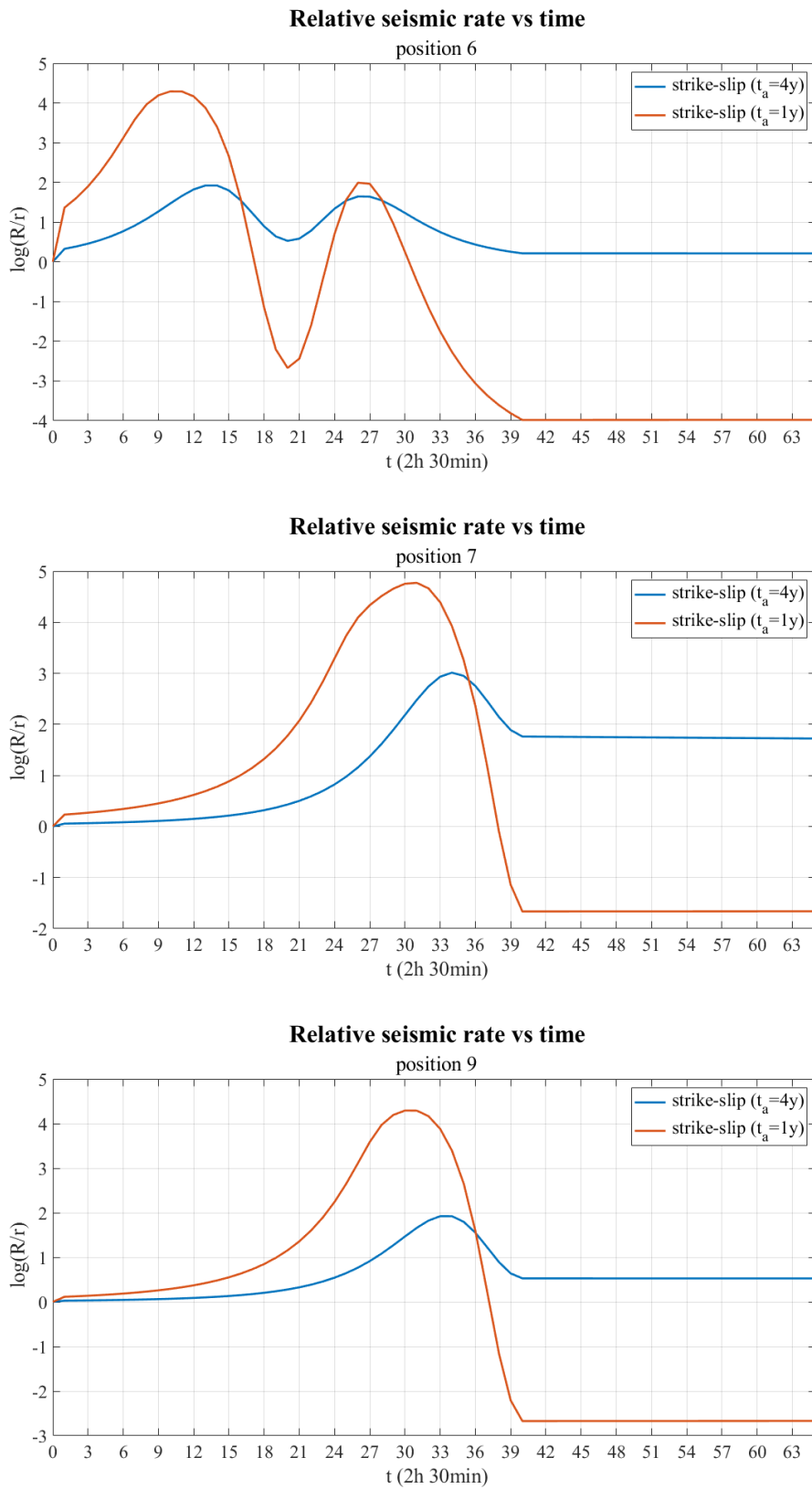

Figure B.3: Decimal logarithm of relative seismic rates versus time, at position P9, for both dip-slip and strike-slip faults.

Figure B.4: Decimal logarithm of relative seismic rates versus time, at positions P1, P3 and P4, for strike-slip faults and two different t_a of 4 and 1 years respectively.

Figure B.5: Decimal logarithm of relative seismic rates versus time, at positions P6, P7 and P9, for strike-slip faults and two different t_a of 4 and 1 years respectively.
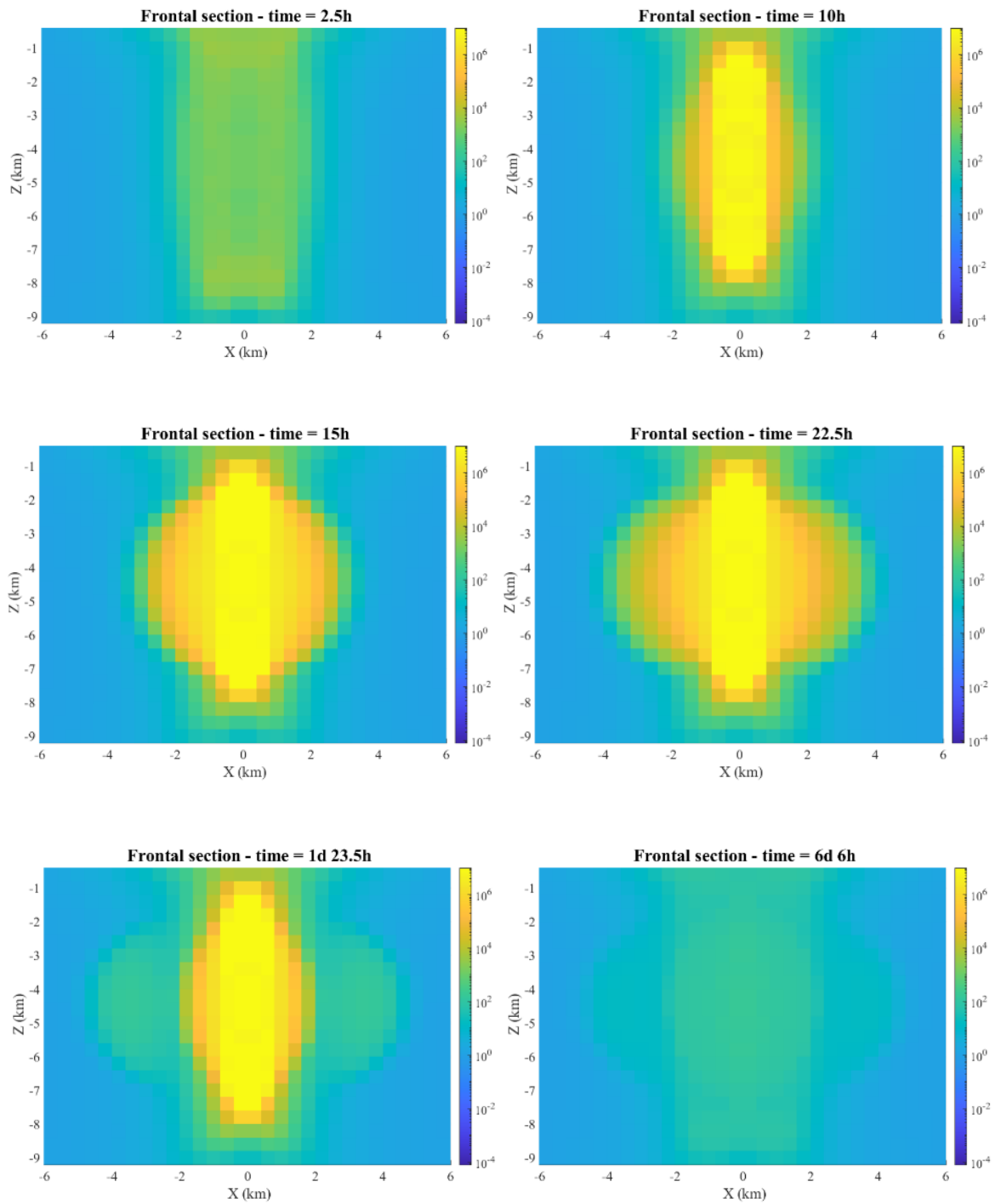
Figure B.6: Frontal section view of the spatial distribution of seismic rates, for strike-slip faults, at 2.5 h, 10 h, 15 h, 22.5 h, 1 d 23.5 h and 6 d 6 h.

Acknowledgments

In this place I would like to thank a series of persons that have helped me before and during the realization of my thesis. First of all I want to thank my professor and supervisor Eleonora Rivalta, who not only introduced me to the world of volcanic dikes and scientific research but also helped me continuously with everything, showing me great and inspiring empathy and helpfulness, which I will not forget. Then I want to thank my family Fabiola, Andrea, Filippo and Camilla, for their perpetual support and presence in my life. Lastly my friends and flat mates, for confronting me with patience and compassion, and for fulfilling my days.

Bibliography

Ágústsdóttir, Thorbjörg et al. (2019). "Intense seismicity during the 2014–2015 Bárarbunga-Holuhraun rifting event, Iceland, reveals the nature of dike-induced earthquakes and caldera collapse mechanisms". In: *Journal of Geophysical Research: Solid Earth* 124(8), pp. 8331–8357.

Aloisi, Marco, Alessandro Bonaccorso, and Salvatore Gambino (2006). "Imaging composite dike propagation (Etna, 2002 case)". In: *Journal of Geophysical Research: Solid Earth* 111(B6).

Amante, Christopher and Barry W Eakins (2009). "ETOPO1 arc-minute global relief model: procedures, data sources and analysis".

Belachew, Manahloh et al. (2011). "Comparison of dike intrusions in an incipient seafloor-spreading segment in Afar, Ethiopia: Seismicity perspectives". In: *Journal of Geophysical Research: Solid Earth* 116(B6).

Cattania, Camilla (2015). "Improvement of aftershock models based on Coulomb stress changes and rate-and-state dependent friction". PhD thesis. Universität Potsdam.

Cattania, Camilla et al. (2017). "A nonplanar slow rupture episode during the 2000 Miyakejima dike intrusion". In: *Journal of Geophysical Research: Solid Earth* 122(3), pp. 2054–2068.

Cocco, Massimo and James R. Rice (2002). "Pore pressure and poroelasticity effects in Coulomb stress analysis of earthquake interactions". In: *Journal of Geophysical Research: Solid Earth* 107(B2), ESE 2-1-ESE 2–17. DOI: https://doi.org/10.1029/2000JB000138.

Crouch, SL and AM Starfield (1984). *Boundary Element Methods in Solid Mechanics by SL Crouch and AM Starfield*.

Dahm, Torsten and Sebastian Hainzl (2022). "A Coulomb Stress Response Model for Time-Dependent Earthquake Forecasts". In: *Journal of Geophysical Research: Solid Earth* 127(9), e2022JB024443.

Davis, Timothy, Eleonora Rivalta, and Torsten Dahm (2020). "Critical fluid injection volumes for uncontrolled fracture ascent". In: *Geophysical Research Letters* 47(14), e2020GL087774.

Davis, Timothy, Eleonora Rivalta, Delphine Smittarello, et al. (2023). "Ascent rates of 3-D fractures driven by a finite batch of buoyant fluid". In: *Journal of Fluid Mechanics* 954, A12.

Deichmann, Nicholas and Domenico Giardini (2009). "Earthquakes induced by the stimulation of an enhanced geothermal system below Basel (Switzerland)". In: *Seismological Research Letters* 80(5), pp. 784–798.

Dieterich, James (1994). "A constitutive law for rate of earthquake production and its application to earthquake clustering". In: *Journal of Geophysical Research: Solid Earth* 99(B2), pp. 2601–2618.

Dieterich, James, Valérie Cayol, and Paul Okubo (2000). "The use of earthquake rate changes as a stress meter at Kilauea volcano". In: *Nature* 408(6811), pp. 457–460.

Dieterich, James H (1979). "Modeling of rock friction: 1. Experimental results and constitutive equations". In: *Journal of Geophysical Research: Solid Earth* 84(B5), pp. 2161–2168.

Dieterich, James H (1981). "Constitutive properties of faults with simulated gouge". In: *Mechanical behavior of crustal rocks: the Handin volume* 24, pp. 103–120.

Felzer, Karen R and Emily E Brodsky (2006). "Decay of aftershock density with distance indicates triggering by dynamic stress". In: *Nature* 441(7094), pp. 735–738.

Fujita, Eisuke et al. (2002). "Cyclic jerky opening of magma sheet and caldera formation during the 2000 Miyakejima volcano eruption". In: *Geophysical research letters* 29(9), pp. 40–1.

Gonnermann, Helge and Benoit Taisne (2015). "Magma transport in dikes". *The encyclopedia of volcanoes*. Elsevier, pp. 215–224.

Griffith, Alan Arnold (1921). "VI. The phenomena of rupture and flow in solids". In: *Philosophical transactions of the royal society of london. Series A, containing papers of a mathematical or physical character* 221(582-593), pp. 163–198.

Gutenberg, Beno and Charles F Richter (1950). "Seismicity of the earth and associated phenomena". In: *MAUSAM* 1(2), pp. 174–176.

Hainzl, Sebastian, Javad Moradpour, and Jörn Davidsen (2014). "Static stress triggering explains the empirical aftershock distance decay". In: *Geophysical Research Letters* 41(24), pp. 8818–8824.

Hainzl, Sebastian, D Steacy, and S Marsan (2010). "Seismicity models based on Coulomb stress calculations". In: *Community Online Resource for Statistical Seismicity Analysis*.

Heimisson, Elías R and Paul Segall (2020). "Physically consistent modeling of dike-induced deformation and seismicity: Application to the 2014 Bárarbunga dike, Iceland". In: *Journal of Geophysical Research: Solid Earth* 125(2), e2019JB018141.

Hughes, Gwyneth Retta (2010). "Investigations of magmatic end-members: Silicic magma chambers and mafic dikes". PhD thesis. Stanford University.

King, Geoffrey CP, Ross S Stein, and Jian Lin (1994). "Static stress changes and the triggering of earthquakes". In: *Bulletin of the Seismological Society of America* 84(3), pp. 935–953.

Maccaferri, Francesco, Maurizio Bonafede, and Eleonora Rivalta (2011). "A quantitative study of the mechanisms governing dike propagation, dike arrest and sill formation". In: *Journal of Volcanology and Geothermal Research* 208(1-2), pp. 39–50.

Maccaferri, Francesco, Eleonora Rivalta, Luigi Passarelli, and Yosuke Aoki (2016). "On the mechanisms governing dike arrest: Insight from the 2000 Miyakejima dike injection". In: *Earth and Planetary Science Letters* 434, pp. 64–74.

Maccaferri, Francesco, Eleonora Rivalta, Luigi Passarelli, and Sigurjón Jónsson (2013). "The stress shadow induced by the 1975–1984 Krafla rifting episode". In: *Journal of Geophysical Research: Solid Earth* 118(3), pp. 1109–1121.

Mallman, Ellen P and Mark D Zoback (2007). "Assessing elastic Coulomb stress transfer models using seismicity rates in southern California and southwestern Japan". In: *Journal of Geophysical Research: Solid Earth* 112(B3).

Montgomery-Brown, Emily K et al. (2011). "Spatiotemporal evolution of dike opening and décollement slip at Kīlauea Volcano, Hawai'i". In: *Journal of Geophysical Research: Solid Earth* 116(B3).

Nikkhoo, Mehdi et al. (Nov. 2016). "Compound dislocation models (CDMs) for volcano deformation analyses". In: *Geophysical Journal International* 208(2), pp. 877–894. DOI: 10.1093/gji/ggw427. URL: https://doi.org/10.1093/gji/ggw427.

Nobile, Adriano et al. (2012). "Dike-fault interaction during the 2004 Dallol intrusion at the northern edge of the Erta Ale Ridge (Afar, Ethiopia)". In: *Geophysical Research Letters* 39(19).

Okada, Yoshimitsu (1985). "Surface deformation due to shear and tensile faults in a half-space". In: *Bulletin of the seismological society of America* 75(4), pp. 1135–1154.

Okada, Yoshimitsu (1992). "Internal deformation due to shear and tensile faults in a half-space". In: *Bulletin of the seismological society of America* 82(2), pp. 1018–1040.

Ozawa, S et al. (2004). "Creep, dike intrusion, and magma chamber deflation model for the 2000 Miyake eruption and the Izu islands earthquakes". In: *Journal of Geophysical Research: Solid Earth* 109(B2).

Passarelli, Luigi et al. (2015). "Stress changes, focal mechanisms, and earthquake scaling laws for the 2000 dike at Miyakejima (Japan)". In: *Journal of Geophysical Research: Solid Earth* 120(6), pp. 4130–4145.

Pollard, David and Raymond Fletcher (Jan. 2005). "Fundamentals of structural geology / David D. Pollard and Raymond C.Fletcher." In: *SERBIULA (sistema Librum 2.0)*. DOI: 10.2277/0521839270.

Reid, Harry Fielding (1910). "The california earthquake of April 18, 1906". In: *Report of the state earthquake investigation commission* 2, pp. 16–18.

Rice, JR (1978). "Thermodynamics of the quasi-static growth of Griffith cracks". In: *Journal of the Mechanics and Physics of Solids* 26(2), pp. 61–78.

Rivalta, E et al. (2015). "A review of mechanical models of dike propagation: Schools of thought, results and future directions". In: *Tectonophysics* 638, pp. 1–42.

Rivalta, Eleonora and Torsten Dahm (2006). "Acceleration of buoyancy-driven fractures and magmatic dikes beneath the free surface". In: *Geophysical Journal International* 166(3), pp. 1424–1439.

Ruch, Joël et al. (2016). "Oblique rift opening revealed by reoccurring magma injection in central Iceland". In: *Nature communications* 7(1), p. 12352.

Ruina, Andy (1983). "Slip instability and state variable friction laws". In: *Journal of Geophysical Research: Solid Earth* 88(B12), pp. 10359–10370.

Saito, Genji et al. (2005). "Petrological characteristics and volatile content of magma from the 2000 eruption of Miyakejima Volcano, Japan". In: *Bulletin of Volcanology* 67, pp. 268–280.

Segall, Paul (2010). *Earthquake and volcano deformation*. Princeton University Press.

Sigmundsson, Freysteinn, Andrew Hooper, et al. (2015). "Segmented lateral dyke growth in a rifting event at Bárarbunga volcanic system, Iceland". In: *Nature* 517(7533), pp. 191–195.

Sigmundsson, Freysteinn, Sigrún Hreinsdóttir, et al. (2010). "Intrusion triggering of the 2010 Eyjafjallajökull explosive eruption". In: *Nature* 468(7322), pp. 426–430.

Simpson, Robert W (1994). *Chapter F. The Loma Prieta, California, Earthquake of October 17, 1989-Tectonic processes and models*. Tech. rep. US Geological Survey.

Spaans, Karsten and Andrew Hooper (2018). "Insights Into the Stress Field Around Bár arbunga Volcano From the 2014/2015 Holuhraun Rifting Event". In: *Journal of Geophysical Research: Solid Earth* 123(4), pp. 3238–3249.

Toda, Shinji, Ross S Stein, Keith Richards-Dinger, et al. (2005). "Forecasting the evolution of seismicity in southern California: Animations built on earthquake stress transfer". In: *Journal of Geophysical Research: Solid Earth* 110(B5).

Toda, Shinji, Ross S Stein, and Takeshi Sagiya (2002). "Evidence from the AD 2000 Izu islands earthquake swarm that stressing rate governs seismicity". In: *Nature* 419(6902), pp. 58–61.

Ueda, Hideki et al. (2005). "Magma intrusion and discharge process at the initial stage of the 2000 activity of Miyakejima, Central Japan, inferred from tilt and GPS data". In: *Geophysical Journal International* 161(3), pp. 891–906.

Utsu, Tokuji, Yosihiko Ogata, et al. (1995). "The centenary of the Omori formula for a decay law of aftershock activity". In: *Journal of Physics of the Earth* 43(1), pp. 1–33.

Watanabe, Tohru et al. (2002). "Analog experiments on magma-filled cracks Competition between external stresses and internal pressure". In: *Earth, planets and space* 54(12), pp. 1247–1261.

Woods, Jennifer et al. (2019). "Evolution of a lateral dike intrusion revealed by relatively-relocated dike-induced earthquakes: The 2014–15 Bárarbunga–Holuhraun rifting event, Iceland". In: *Earth and Planetary Science Letters* 506, pp. 53–63.

Xu, Caijun et al. (2010). "Applying the Coulomb failure function with an optimally oriented plane to the 2008 Mw 7.9 Wenchuan earthquake triggering". In: *Tectonophysics* 491(1-4), pp. 119–126.

Yeats, Robert S (1998). "Living with earthquakes in the Pacific Northwest".